# SEARCH FOR SQUARKS AND GLUINOS WITH THE DØ DETECTOR

**Name: Mark A. Goforth**

**Department: Department of Physics**

**Major Professor: Horst Wahl**

**Degree: Doctor of Philosophy**

**Term Degree Awarded: Summer, 1995**

A search for the pair production of supersymetric particles using data from the DØ detector at the Fermilab $\overline{p}p$ Tevatron collider, with center of mass energy $\sqrt{s} =$ 1.8 TeV, has yielded a null result. The search was performed looking for gluino and squark decays with a signature of multiple particle jets and high missing transverse energy. With a total luminosity of 7.5 $\text{pb}^{-1}$ of data, and with no signal events observed above expected Standard Model backgrounds, the existence of gluinos and squarks has been excluded with masses below 213 $\text{GeV}/\text{c}^2$ at the 95% confidence level for equal squark and gluino mass.

# SEARCH FOR SQUARKS AND GLUINOS WITH THE DØ DETECTOR

**Mark A. Goforth, Ph.D.**
**Florida State University, 1995**
**Major Professor: Horst Wahl, Ph.D.**

A search for the pair production of supersymetric particles using data from the DØ detector at the Fermilab $\overline{p}p$ Tevatron collider, with center of mass energy $\sqrt{s} =$ 1.8 TeV, has yielded a null result. The search was performed looking for gluino and squark decays with a signature of multiple particle jets and high missing transverse energy. With a total luminosity of 7.5 $pb^{-1}$ of data, and with no signal events observed above expected Standard Model backgrounds, the existence of gluinos and squarks has been excluded with masses below 213 $GeV/c^2$ at the 95% confidence level for equal squark and gluino mass.

THE FLORIDA STATE UNIVERSITY
COLLEGE OF ARTS AND SCIENCES

# SEARCH FOR SQUARKS AND GLUINOS WITH THE DØ DETECTOR

By
MARK A. GOFORTH

A Dissertation submitted to the
Department of Physics
in partial fulfillment of the
requirements for the degree of
Doctor of Philosophy

Degree Awarded:
Summer Semester, 1995

## ACKNOWLEDGEMENTS

Thanks to my mother, who has always believed in me. Thanks to my wife, Julie, for her devotion and support.

Thanks to all the DØ collaborators for their dedication and hard work on the experiment. I owe a debt of graditude to the members of the New Phenomena Group: Wyatt Merrit, Marc Paterno, Doug Norman, Amber Boehnlein, Nick Hadley, and others.

A special thanks to the faculty members of the High Energy Physics group at Florida State University: Howie Baer, Sue Blessing, Harvey Goldman, Sharon Hagopian, Vasken Hagopian, Jeff Owens, Harrison Prosper, and Horst Wahl. Their patience, experience and knowledge has helped me complete this degree.

## CONTENTS

List of Figures . . . . . vi

List of Tables . . . . . vii

ABSTRACT . . . . . ix

**1 Supersymmetry** **1**

1.1 Introduction . . . . . 1

1.2 The Standard Model . . . . . 2

1.3 The Supersymmetry Model . . . . . 5

1.3.1 The Supersymmetric Particle Spectrum . . . . . 9

1.3.2 MSSM Parameters . . . . . 10

1.3.3 Current Limits on Supersymmetry Masses . . . . . 11

1.4 Search for Supersymmetry Using the DØ Detector . . . . . 13

1.4.1 Squark and Gluino Signatures at DØ . . . . . 13

1.4.2 Squark and Gluino Cross Sections at the Tevatron . . . . . 15

1.5 Terminology and Definitions . . . . . 18

**2 Experimental Apparatus** **20**

2.1 Fermilab Tevatron Collider . . . . . 20

2.2 Calorimeters . . . . . 24

2.2.1 Electromagetic Showers . . . . . 25

2.2.2 Hadronic Showers . . . . . 26

2.3 DØ Calorimeter . . . . . 27

2.3.1 Electromagnetic Calorimeter . . . . . 31

2.3.2 Hadronic Calorimeter . . . . . 31

2.3.3 Intercryostat Detector . . . . . 33
2.4 DØ Tracking System . . . . . 34
2.4.1 Vertex Chamber . . . . . 34
2.4.2 Transition Radiation Detector . . . . . 34
2.4.3 Central and Forward Drift Chambers . . . . . 36
2.5 DØ Muon System . . . . . 39

**3 Trigger and Data Acquisition 41**
3.1 Level 0 Trigger . . . . . 42
3.2 Level 1 Trigger . . . . . 44
3.3 Level 2 . . . . . 44
3.4 Missing Transverse Energy ($\not\!\!E_T$) Trigger . . . . . 46
3.5 Luminosity . . . . . 47

**4 Event Selection 50**
4.1 Data Collection . . . . . 50
4.2 Jets . . . . . 51
4.2.1 DØ Cone Algorithm . . . . . 52
4.3 Energy Corrections . . . . . 53
4.3.1 Electromagnetic Energy Scale . . . . . 55
4.3.2 Hadronic Energy Scale . . . . . 55
4.3.3 Out-of-Cone Showering . . . . . 56
4.3.4 Zero-Suppression . . . . . 56
4.3.5 Underlying Event . . . . . 57
4.4 Missing Transverse Energy ($\not\!\!E_T$) Resolution . . . . . 57
4.5 Data Streaming . . . . . 58

**5 Data Analysis 61**

5.1 Multiple Interactions . . . . . 61
5.2 Jets . . . . . 65
5.2.1 Leading Cell Fraction . . . . . 65
5.2.2 Main Ring Interactions . . . . . 66
5.2.3 Electromagnetic Fraction . . . . . 67
5.2.4 ICD Faction . . . . . 67
5.2.5 Number of Cells in the Jet . . . . . 68
5.3 Signal Selection: Missing Transverse Energy ($\not\!\!E_T$) and Number of Jets 68
5.4 Background Calculations . . . . . 72
5.4.1 DØ Detector Simulation . . . . . 73
5.5 Vector Boson Backgrounds . . . . . 75
5.6 QCD Background . . . . . 75
5.6.1 Estimate from Collider Data . . . . . 77
5.6.2 Estimate from Monte Carlo with Jet $E_T$ Smearing . . . . . 77
5.7 Squark-Gluino Efficiencies . . . . . 82
5.8 Systematic Uncertainties . . . . . 83

**6 Results** **87**
6.1 Event Limit . . . . . 87
6.2 Mass Limit . . . . . 89
6.3 Effect of Varying the $\not\!\!E_T$ Cut on the Mass Limit . . . . . 93
6.3.1 Effects of Varying Supersymmetry Model Parameters . . . . . 96
6.4 Future Searches . . . . . 100

**BIBLIOGRAPHY** **101**

**Biographical Sketch** **108**

## LIST OF TABLES


1.1 Standard Model Particles . . . . . 3

1.2 Known Interactions . . . . . 4

1.3 Supersymmetric Particles . . . . . 6

1.4 Supersymmetry Model Parameters . . . . . 11

1.5 High Energy Physics Units . . . . . 19

2.1 Calorimeter Electromagnetic Section Characteristics . . . . . 32

2.2 Calorimeter Hadronic Section Characteristics . . . . . 33

2.3 Vertex Chamber . . . . . 35

2.4 Transition Radiation Detector . . . . . 37

2.5 Central and Forward Chamber . . . . . 38

2.6 Muon Detector . . . . . 40

3.1 $\not{E}_T$ Trigger History . . . . . 49

3.2 Jet-Miss Trigger History . . . . . 49

5.1 Multiple Interaction Flag . . . . . 64

5.2 Data Selection . . . . . 72

5.3 Monte Carlo Estimates for W and Z Boson Backgrounds . . . . . 76

5.4 Parameters Used in the DØ Jet Energy Resolution Function . . . . . 80

5.5 Supersymmetry Model Parameters . . . . . 82

5.6 Supersymmetry Signal Monte Carlo, Efficiencies and Cross Sections . 84

5.7 Systematic Uncertainties . . . . . 86

## LIST OF FIGURES


1.1 $\not{E}_T$ Distribution from Supersymmetry Monte Carlo . . . . . 9

1.2 Number of jets produced with varying gluino mass . . . . . 14

1.3 Squark and gluino cross sections at the Fermilab Tevatron . . . . . 16

2.1 DØ Detector . . . . . 21

2.2 DØ Calorimeter . . . . . 28

2.3 Calorimeter detector shown in interaction lengths . . . . . 29

3.1 Data Acquisition System . . . . . 43

3.2 Calorimeter with $\eta$ divisions . . . . . 45

4.1 Energy Corrections to jet $E_T$ and $\not{E}_T$ . . . . . 54

5.1 $\not{E}_T$ Resolution and Vertex Mismeasurement . . . . . 63

5.2 Multiple Interaction Flag Distribution . . . . . 65

5.3 Angular cut between $\not{E}_T$ and Jets . . . . . 70

5.4 Jet Multiplicity of Collider Data . . . . . 71

5.5 $\not{E}_T$ Distribution of Collider Data . . . . . 71

5.6 $\not{E}_T$ Distribution Compared for Data and Background Monte Carlo . . 76

5.7 $\not{E}_T$ distribution from QCD trigger . . . . . 78

5.8 Variation of Collider Data and Backgrounds with $\not{E}_T$ . . . . . 79

5.9 $\not{E}_T$ distribution from ISAJET Monte Carlo . . . . . 81

5.10 Signal Efficiency for Heavy Squarks . . . . . 85

5.11 Signal Efficiency for Equal Mass Squarks and Gluinos . . . . . 85

6.1 Gluino Mass Limit for Heavy Squarks . . . . . 91

6.2 Squark-Gluino Mass Limit for Equal Masses . . . . . 91
6.3 Squark-Gluino Mass Limit Contour . . . . . 92
6.4 Combined Squark-Gluino Mass Limits from Various Experiments . . 94
6.5 Gluino Mass Limit with Varying $\not{E}_T$ Cut . . . . . 96
6.6 Effects of varying the $\tan\beta$ parameter . . . . . 98
6.7 Effect of varying the $\mu$ parameter . . . . . 99

## ABSTRACT

A search for the pair production of supersymetric particles using data from the DØ detector at the Fermilab $\overline{p}p$ Tevatron collider, with center of mass energy $\sqrt{s} =$ 1.8 TeV, has yielded a null result. The search was performed looking for gluino and squark decays with a signature of multiple particle jets and high missing transverse energy. With a total luminosity of 7.5 $pb^{-1}$ of data, and with no signal events observed above expected Standard Model backgrounds, the existence of gluinos and squarks has been excluded with masses below 213 $GeV/c^2$ at the 95% confidence level for equal squark and gluino mass.

# CHAPTER 1
# SUPERSYMMETRY

## 1.1 Introduction

A fundamental belief held in the sciences is that the structure of the universe is ordered. Discovering order is the first step toward an understanding of our physical world. A symmetry is a type of order seen in nature. The German physicist Hermann Weyl often said, "Nature loves symmetry." Throughout history symmetries have played a key role in forming explanations for the physical world. The ancient Greeks, upon discovery of the Polyhedra (three-dimensional figures with more than four sides and angles), concluded that the whole world was built from these symmetrical shapes [1]. In fact, our word *symmetry* comes from the Greek word *summetros* meaning well-ordered or of like measure.

Since the sixteenth century, symmetries have been assumed to be a fundamental law of nature. Kepler, the influential astronomer of the sixteenth century, concluded his book *Mysterium Cosmographicum* with the sentence "Credo spatioso numen in orbe" — "I believe in the geometric order of the universe" [2]. Today, our advanced technology has allowed us to observe symmetry at all levels of nature.

A physical system exhibits symmetry if it remains unchanged under a particular operation. Symmetries observed in nature can be from translations, rotations, and reflections. Geometric symmetries are encountered in molecules and crystals. Dynamic symmetries were discovered in the development of quantum mechanics, the order of states of a physical system. Wolfgang Pauli first observed a dynamic symmetry in the regularity of the discrete spectrum of the hydrogen atom [3].

Symmetry arguments are often used to predict undiscovered effects and promote the formulation of new theories. The mass spectrum of hadrons has been described

by the special transformation group $SU(3)$ [4]. Maxwell's inclusion of the electromagnetic "displacement current" in his equation for the curl of the magnetic field was based on grounds of symmetry rather than experimental results.

## 1.2 The Standard Model

All matter is comprised of elementary spin-1/2 particles (fermions) called quarks (which make up the proton and neutron) and leptons such as the electron (see Table 1.1). These particles interact via four fundamental interactions: gravity and the electromagnetic, weak and strong nuclear forces. The latter three interactions are described by gauge field theories as the exchange of bosons, particles of integer spin. The Standard Model predicts the strong [5], weak and electromagnetic [6] interactions among the quarks and leptons. The top quark was the last of the six quarks to be discovered [7] and completes the three matter families of the Standard Model. Although the force of gravity is the most familiar of all the interactions, there is not yet a testable quantum theory of gravity.

The gauge bosons of the Standard Model, shown in Table 1.2, include spin-1 particles which mediate the strong and electroweak interactions. The electromagnetic force is described through the exchange of massless photons. Since photons are massless, the range of the electromagnetic interaction is infinite. The weak interactions are mediated by massive particles called $W$ and $Z$ gauge bosons with only a short range. The $W$ and $Z$ bosons were first observed at the CERN collider, confirming the predictions of the electroweak theory [9].

In the Standard Model, the generation of the fermion masses is accomplished by the presence of the Higgs particle, a spin-0 boson that spontaneously breaks the electroweak symmetry [10]. The Higgs boson interacts by a Yukawa coupling.

Table 1.1: Matter particles in the Standard Model with their masses [8]. The electric charge is shown in units of the electron charge.

| Name | Electric Charge | Mass (MeV/c$^2$) |
|---|---|---|
| leptons | | |
| electron e | -1 | 0.511 |
| neutrino $\nu_e$ | 0 | $< 7.3 \times 10^{-6}$ |
| muon $\mu$ | -1 | 105.7 |
| neutrino $\nu_\mu$ | 0 | $< 0.27$ |
| tau $\tau$ | -1 | 1784 |
| neutrino $\nu_\tau$ | 0 | $< 35$ |
| quarks | | |
| up u | $-1/3$ | $\approx 5.6$ |
| down d | $2/3$ | $\approx 9.9$ |
| strange s | $-1/3$ | $\approx 199$ |
| charm c | $2/3$ | $\approx 1,350$ |
| bottom b | $-1/3$ | $\approx 5,000$ |
| top t | $2/3$ | $\approx 180,000$ |

Table 1.2: The four fundamental forces and their characteristics. The mediating particles are bosons that are exchanged in the theory. Although the graviton has not been observed, it may be the quantum exchanged in a quantum field theory of gravity. The strength of the gauge couplings depend on the characteristic momentum or distance of the interaction.

| Interaction | Relative Strength | Range | Mediating Particle |
|---|---|---|---|
| gravitational | $5.3 \times 10^{-39}$ | $\infty$ | graviton? |
| electromagnetic | $\alpha_{em} = 1/137$ | $\infty$ | photon ($\gamma$) |
| weak | $10^{-6}$ | $10^{-18}$ m | Vector Bosons ($W^{\pm}, Z^0$) |
| strong | $0.1 - 1.0$ | $10^{-15} - 10^{-16}$ m | gluon ($g$) |

Since the quarks have different masses, each quark must couple to the Higgs with a different strength. The Higgs boson associated with the electroweak scale is expected to have a mass of less than 1000 GeV/c$^2$ to maintain unitarity in the Standard Model.

Although the Standard Model has been sufficient to explain the observed phenomena at high energy colliders to date, there are indications that the Standard Model is not a complete theory. There are many parameters in the Standard Model that cannot be determined except via experiment (nine fermion masses, charged Higgs mass, electromagnetic coupling constant, Fermi coupling constant, and the weak mixing angle, $\sin\theta_W$).

Loop diagrams are higher order radiative corrections for particles spending a short time in a virtual state. For any quantum field theory with elementary scalar fields (the Higgs boson is an elementary scalar field), the radiative correction to the scalar boson mass diverges quadratically as the internal momentum in the loop becomes very large [11, 12]. A cutoff, $\Lambda$, can be imposed at some high energy scale (usually the Grand Unification scale, where the electromagnetic, weak and strong forces are expected to arise from one massive gauge boson) where degrees of freedom

not included in the Standard Model become relevant. In lowest order perturbation theory, $m_H^2 = m_0^2 + \delta m_H^2 \sim m_0^2 - g^2\Lambda^2$, where $m_H$ is the Higgs mass, $m_0$ is the bare Higgs boson mass in the Lagrangian, and $g$ is a dimensionless coupling constant. The Higgs mass must be comparable to the electroweak scale, $m_H \sim 250$ GeV/c$^2$. If $\Lambda \sim M_{\rm gut}$ or $M_{\rm Planck}$, where gravitation becomes relevant, and $g^2 \sim 1$, then $m_0^2$ and $\delta m_H^2$ are each $\sim 10^{30}$ GeV$^2$/c$^4$ and the difference must leave $m_H \sim 250$ GeV/c$^2$. Therefore, if loop corrections to the lightest Higgs particles are applied to observables, Grand Unified Theories require fine tuning the mass order by order in perturbation theory to an accuracy of $10^{-26}$. This delicate tuning of the Higgs mass in GUT Models is known as the hierarchy problem, the large difference between symmetry-breaking scales in GUT and electroweak theories.

Although there is no experimental evidence for new particles or interactions, the above deficiencies with the Standard Model may indicate that the Standard Model is only valid in the current energy regime and new degrees of freedom, and new particles or interactions, are at the energy scale of $\sim 1000$ GeV/c$^2$. Ideas for the new physics include compositeness (quarks and leptons are made of constituents), supersymmetry (a symmetry relating particles of different spin), leptoquarks (a particle with both lepton and quark quantum numbers), or something else unknown.

## 1.3 The Supersymmetry Model

Supersymmetry is a symmetry relating particles of different spin [13, 14]. The spin of a supersymmetric particle differs by 1/2 from that of its ordinary Standard Model counterpart, relating fermions to bosons, but other quantum numbers and interactions remain the same. The known elementary particles and their superpartners are listed in Table 1.3. Although no supersymmetric particles have yet been

Table 1.3: Standard Model particles and their supersymmetric counterparts. The fermions have a fractional spin, and the bosons have integral spin. The theory of supersymmetry relates fermions to bosons [12].

| Particle | Spin | Electric Charge | $R$-parity |
|---|---|---|---|
| $g$ gluon | 1 | 0 | 1 |
| $\tilde{g}$ gluino | $\frac{1}{2}$ | 0 | -1 |
| $q$ quark | $\frac{1}{2}$ | $\frac{2}{3}, -\frac{1}{3}$ | 1 |
| $\tilde{q}$ squark | 0 | $\frac{2}{3}, -\frac{1}{3}$ | -1 |
| $e$ electron | $\frac{1}{2}$ | -1 | 1 |
| $\tilde{e}$ selectron | 0 | -1 | -1 |
| $\nu$ neutrino | $\frac{1}{2}$ | 0 | 1 |
| $\tilde{\nu}$ sneutrino | 0 | 0 | -1 |
| $\gamma$ photon | 1 | 0 | 1 |
| $W^{\pm}, Z^0$ intermediate bosons | 1 | $\pm 1, 0$ | 1 |
| $H$ Higgs bosons | 0 | $\pm 1, 0$ | 1 |
| $\tilde{\chi}^0_{1,2,3,4}$ neutralinos | $\frac{1}{2}$ | 0 | -1 |
| $\tilde{\chi}^{\pm}_{1,2}$ charginos | $\frac{1}{2}$ | $\pm 1$ | -1 |

discovered, supersymmetry offers several interesting solutions to problems found in the Standard Model.

A unified theory is defined as one set of equations that unifies the gravitational, electromagnetic, strong and weak nuclear forces. As science probes subatomic particles using higher energies, and thus at smaller distances, the strengths of the strong, weak, and electromagnetic forces appear to converge. This indicates that the fundamental forces of nature, the strong, weak, and electromagnetic forces, are aspects of a single interaction, mediated by exotic particles with a mass of $\sim 10^{16}$ GeV/c$^2$

This led to the formulation of Grand Unification Theories (GUTs) [15]. The previously mentioned fine tuning problem can be solved by introducing a boson-fermion symmetry to the GUT theory.

Gravity can be included in particle physics by requiring local supersymmetry. Local supersymmetry, known as supergravity, reduces to general relativity, and relates matter fields to gauge fields to unify all forces. Furthermore, the supersymmetric extension of the Standard Model requires many new parameters that must be specified, including some 26 coupled differential equations [16]. Within the supergravity framework, the number of parameters required to specify all the masses and interactions of the super particles reduces to a small set (see Section 1.3.2).

In a supersymmetric theory, a new fermion field with properties related to the original spin zero Higgs field is included. The spin zero fields are then protected from acquiring enormous masses via radiative corrections, referred to as loop graphs [17]. The diagrams from fermion particles and their boson partners have opposite signs that cancel the quadratic divergences when combined. In order for the graphs to cancel, the supersymmetric particle masses must be less than $\sim 1000$ GeV/c$^2$ if supersymmetry is to resolve the hierarchy problem.

In an elementary supersymmetric theory, the spin 1/2 operator $Q$ changes the total angular momentum by 1/2 unit relating bosons to fermions, spinors (fermions and their antiparticles) to vectors, and scalars to spinors: $Q_\alpha|\text{boson}\rangle = |\text{fermion}\rangle$ where $\alpha$ is a spinor index. The (anti)commutation rules for the supersymmetry generators are:

$$[Q_\alpha, P^\mu] = 0$$

$$[Q_\alpha, M^{\mu\nu}] = i(\sigma^{\mu\nu}Q)_\alpha$$

$$[Q_\alpha, \overline{Q_\beta}]_+ = -2(\gamma_\mu)_{\alpha\beta}P^\mu$$

$$[Q_\alpha, Q_\beta]_+ = [\overline{Q_\alpha}, \overline{Q_\beta}]_+$$

where $P^\mu$ are the Poincaré generators and $\alpha$, $\beta$, are spinors indexes and $\mu$, $\nu$ are 4-vector indices, and $\sigma^{\mu\nu} = \frac{1}{4}[\gamma^\mu, \gamma^\nu]$. Although more generators can be used, only one supersymmetric generator is required to allow the fermions to be in chiral [1] representations, as experimentally observed. These transformation rules indicate that the supersymmetric generator transforms as a spinor. Two successive supersymmetric transformations involve a space-time translation; therefore supersymmetry is not an internal symmetry and the supersymmetric generator commutes with internal symmetries such as electric charge. Therefore, the predicted supersymmetric particles will have the same Standard Model quantum numbers as their ordinary matter counterparts, except for spin.

The Minimal Supersymmetric Standard Model (MSSM) is the inclusion of the minimum number of supersymmetric particles (sparticles) and their interactions to the Standard Model [12]. Particles are assigned a multiplicative quantum number $R$-parity defined as $R = (-1)^{3(B-L)+2S}$ where $B$ is the baryon number, $L$ is the lepton number, and $S$ is the particle spin. Ordinary Standard Model particles are assigned even $R$-parity ($R = +1$) and superparticles have odd $R$-parity ($R = -1$). By conservation of $R$-parity, superparticles would be pair produced and eventually decay to the lightest supersymmetric particle (LSP).

If $R$-parity is conserved, then the LSP should be both electrically and color neutral, and absolutely stable. An electrically charged or strongly interacting LSP would have been detected by its ability to bind with nuclei or atoms to make heavy isotopes. The LSP is assumed to be the lightest neutralino, $\tilde{\chi}_1^0$, a mixture of the Higgsinos and gauginos, combinations of supersymmetric fermions with the same quantum numbers. A weakly interacting particle escapes detection in a calorimeter.

[1] The Weyl field is used to describe the massless neutrinos in weak interactions, where the neutrinos have only negative helicity states and the antineutrinos have only positive helicity states.

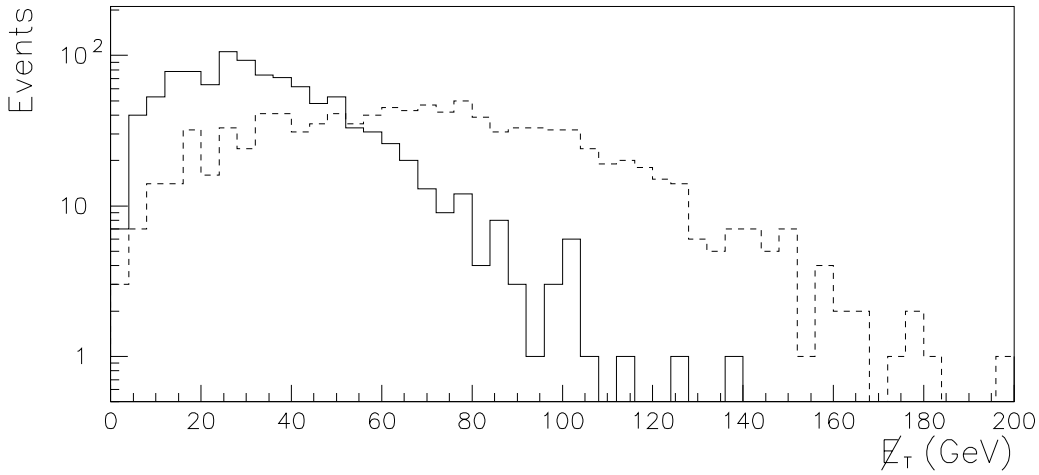


Figure 1.1: $\not{E}_T$ distribution from supersymmetry Monte Carlo for $m_{\tilde{q}}$= 150 GeV/c$^2$ and $m_{\tilde{g}}$= 100 (solid) and 200 (dotted) GeV/c$^2$.

This energy carried by the weakly interacting LSP will be indicated by "missing transverse energy" ($\not{E}_T$), an energy imbalance in the direction transverse to the beam direction. To illustrate the large $\not{E}_T$ for supersymmetric events, Figure 1.1 shows the $\not{E}_T$ distribution from supersymmetry Monte Carlo (see Section 5.7) for $m_{\tilde{g}}$= 100 and 200 GeV/c$^2$ for $m_{\tilde{q}}$= 150 GeV/c$^2$. The $\not{E}_T$ signature becomes more pronounced for higher mass particles that provide more energy for the LSP to carry. The canonical signature for supersymmetric particle production is $\not{E}_T$ due to the escape of the weakly interacting LSP.

Supersymmetry offers a solution to the fine-tuning problem, provides a mechanism for including gravity, and the LSP is a good candidate for cold dark matter [18].

### 1.3.1 The Supersymmetric Particle Spectrum

In a supersymmetric theory, each known particle and field is a member of a supersymmetric pair. Superparticles have yet to be discovered; no known particle can be the superpartner of another known particle. Therefore, supersymmetry must

be a broken symmetry so that the mass degeneracy is removed but the other relations and couplings remain the same.

The supersymmetric partners of the gauge particles are given their Standard Model related names with the addition of the "ino" suffix. The spin-1/2 gluino is the supersymmetric partner of the gluon, the mediator of the strong force.

The supersymmetric partner of the quark is called the squark. The squark has the same interactions as the quark, only the squark is a boson with spin 0. There are two degrees of freedom for the spin-1/2 quark (spin up and spin down). The number of degrees of freedom for the squark must be the same as its ordinary matter partner, the quark. Therefore there would be left and right-handed squarks since both have spin 0. Due to the absence of the observation of strong flavor-changing neutral currents in the $K$-meson sector, the squark masses of the first two generations would be nearly identical in the simplest supergravity model [19].

The supersymmetric partners of the $W$, $Z$ and Higgs gauge bosons are called gauginos and Higgsinos. The mass eigenstates, charginos and neutralinos, are complex mixtures of the Higgsinos and gauginos, combinations of supersymmetric fermions with the same quantum numbers. Charginos and neutralinos may decay into leptons, quarks, or supersymmetric particles and always finally decay into the LSP since $R$-parity is assumed conserved.

In a supersymmetric theory, two Higgs doublets are required to give masses to the left and right quarks and charged leptons where only one is necessary in the Standard Model. The quantum numbers of supersymmetric particles and their counterparts are given in Table 1.3.

### 1.3.2 MSSM Parameters

Although supersymmetry roughly doubles the number of particles in the Standard Model, only six new parameters must be introduced into the theory within the supergravity inspired model [16]. All superparticle masses and mixings are de-

Table 1.4: Supersymmetry model parameters used for the ISAJET Monte Carlo in signal cross section caculations.

| Parameter | Value Used |
|---|---|
| $\tan\beta$ | 2 |
| $\mu$ | $-250$ GeV |
| $m_{\rm top}$ | 140 GeV/c$^2$ |
| $m_{\rm H^+}$ | 500 GeV/c$^2$ |

termined by six parameters of the supergravity-inspired MSSM and can only be determined by experiment: the gluino mass ($m_{\tilde{g}}$), squark mass ($m_{\tilde{q}}$), supersymmetric higgsino mass parameter ($\mu$), the ratio of the vacuum expectation values of the Higgs fields ($v_1/v_2$), the top quark mass ($m_{\rm top}$), and the mass of the charged Higgs ($m_{\rm H+}$). The ratio of the vacuum expectation values of the Higgs fields is usually expressed as $\tan\beta = v_1/v_2$. The model parameters chosen for this analysis are listed in Table 1.4.

The supersymmetry Monte Carlo data was generated before the discovery of the top quark (with measured mass of 180-200 GeV/c$^2$ [7]). At the time, the top mass was thought to be close to 140 GeV/c$^2$, the top mass chosen for this analysis. Chosing the top mass of 140 GeV/c$^2$, rather then the correct top mass, does not have a strong influence on the production cross section of the first two generations of squarks and therefore the results of this analysis.

### 1.3.3 Current Limits on Supersymmetry Masses

For supersymmetry to be a solution to the hierarchy problem, the supersymmetric particles must have masses less than 1000 GeV/c$^2$ (see Section 1.2). In addition,

various experiments have placed lower limits and constraints on sparticle masses and MSSM parameters.

The UA1/UA2 collaborations were the first to place limits on the squark and gluino masses by searching for high $\not{E}_T$ events and, observing no events above Standard Model backgrounds [20]. The limits on the gluino and squark masses were determined assuming that the squark and gluino only decays directly into the lightest supersymmetric particle and the results were $m_{\tilde{q}} > 74$ GeV/c$^2$ and $m_{\tilde{g}} > 79$ GeV/c$^2$ with a 95% confidence level

From the absence of anomalous decays of the $Z$ boson and precise measurement of its line shape (or the decay width), the ALEPH experiment at the electron-positron collider of CERN has been able to place lower limits on the chargino, slepton, sneutrino, and squark masses of 45 GeV/c$^2$ [21]. For small values of $\tan\beta$, supersymmetry theory predicts a light Higgs scalar which would have been detected at LEP, thus the LEP measurements have indirectly excluded the entire range of gluino masses [22] for $\tan\beta < 1.6$. Also, for values of positive $\mu$, LEP has excluded the gluino mass range currently accessible at Fermilab ($\sim 250$ GeV/c$^2$).

The CDF experiment at Fermilab presented a bound on the gluino mass from a study of multijet and high $\not{E}_T$ events in proton–antiproton collisions [23]. For direct decays into the LSP, the CDF experiment has set a limit for equal mass gluinos and squarks of $m_{\tilde{q}}=m_{\tilde{g}} > 225$ GeV/c$^2$ at a 90% confidence level, where they have chosen model parameters the same as this analysis. Depending on those model parameters, the gluino bound from CDF measurements is diminished by 10 to 15 GeV/c$^2$ when the effect of cascade decays is included [24]. The squark mass bound diminishes with increasing gluino mass since the LSP mass increases with increasing gluino mass, absorbing more of the energy of the squark-pair events. By combining the CDF bounds on the gluino mass and the LEP contraints on the MSSM model parameters, a lower bound on the LSP mass of 18 GeV/c$^2$ results [25].

The current squark and gluino mass limits are shown in Figure 6.4.

## 1.4 Search for Supersymmetry Using the DØ Detector

### 1.4.1 Squark and Gluino Signatures at DØ

Although heavy particles require large amounts of energy to be created, gluinos and squarks could be produced at a high energy hadron collider and the failure to observe them would allow limits to be placed on their masses. A potential signal for supersymmetric particles at the Fermilab Tevatron Collider is the strong production of gluinos and squarks. The Fermilab Tevatron collides protons and antiprotons at a center-of-mass energy of 1.8 TeV. The strong interaction between the proton and antiproton dominates particle production. Since the gluino and squark interact via known gauge couplings, the cross sections for their production are calculable in terms of their masses.

For heavy gluinos and squarks, decay into charginos and neutralinos before subsequent decay into the LSP will dominate rather than direct decays into the LSP [26]. For gluino masses above 135 GeV/c$^2$, an intermediate decay into charginos will account for more than half of the gluino decays [27].

The final event signature will depend on the decay of the charginos, but by $R$-parity conservation, the event will always end with the stable (weakly interacting) LSP. The final $\not{E}_T$ spectrum from cascade decays is considerably softer than that of direct decays, because the energy is shared among more particles, leaving less energy to be carried by the LSP. The heavy gluinos and squarks will have intermediate decays to charginos and neutralinos. This will introduce more jets into each event, and possibly signatures with leptons as well as jets in the final state. The heavier the produced particles are, the more the average number of jets per event increases.

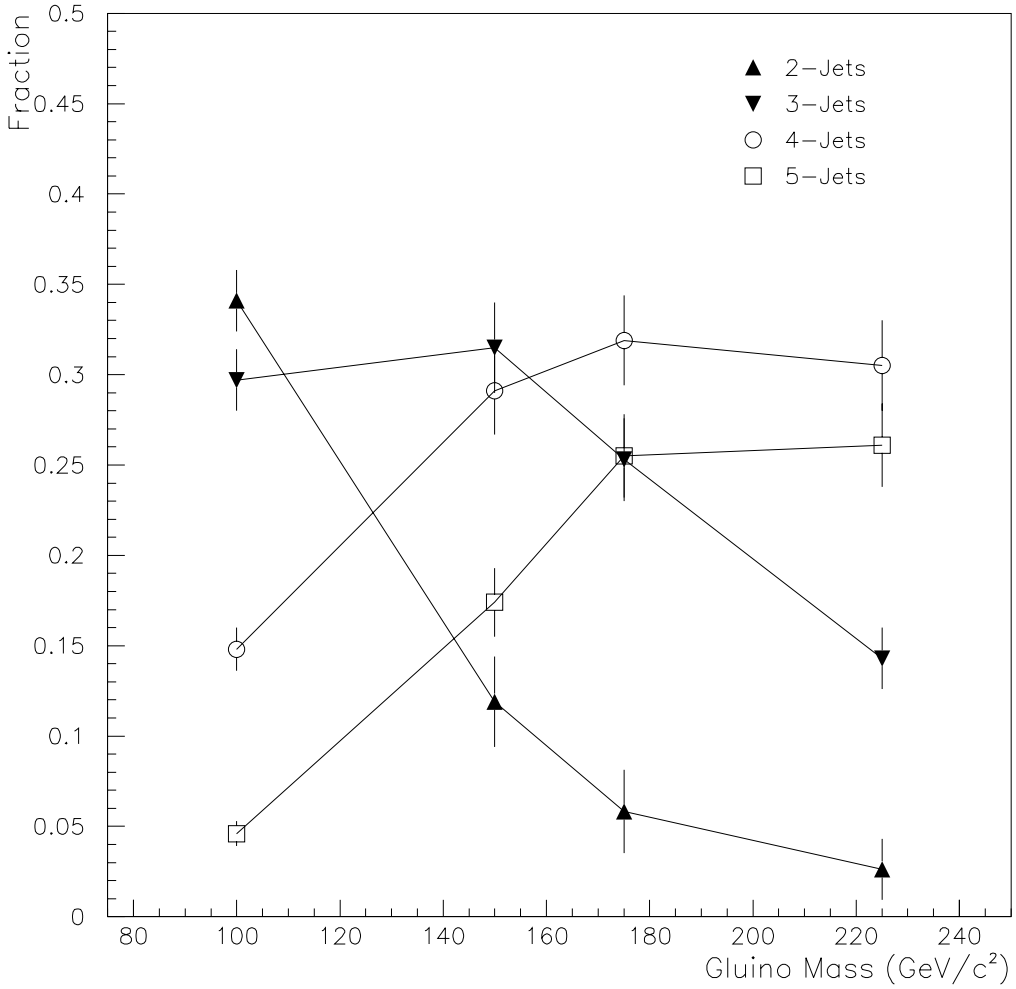


Figure 1.2: Fraction of signal events with multiple jets predicted by supersymmetry Monte Carlo. For high gluino masses cascade decays into charginos and neutralinos before decay into the LSP dominate the cross section. The squark mass is fixed at 500 GeV/$c^2$.

This can be seen in Figure 1.2, which shows the fraction of events with three, four and five jets as a function of gluino mass.

Thus, production and cascade decay of supersymmetric particles would manifest itself as events with multi-jets, leptons, and $\not\!\!E_T$ from the LSP and neutrinos. The cross sections for these decay channels have been calculated [28]. A signature of high $\not\!\!E_T$ is relatively free from backgrounds and is the most prominent signature for supersymmetry. This dissertation reports a search for the evidence of supersymmetric particles at the Fermilab Tevatron collider in the channel four or five jets and large $\not\!\!E_T$.

### 1.4.2 Squark and Gluino Cross Sections at the Tevatron

The cross sections for gluino-gluino, squark-gluino, and squark-squark production at the Tevatron were calculated with the Monte Carlo event generator ISAJET 7.13 [29]. The ISAJET Monte Carlo program is a leading-order calculation and includes only tree-level diagrams.

The cross sections were determined by a Supergravity inspired model [16]. The model included the minimum supersymmetric extensions to the Standard Model and assumed $R$-parity conservation. If $R$-parity is not conserved, there may be a significant effect on the $\not\!\!E_T$ signature and the squark-gluino cross sections [30]. The supersymmetry cross sections depend most strongly on the squark and gluino masses. The supersymmetric parameters used in the calculation are listed in Table 1.4. The top squark mass was set to 500 GeV/c$^2$ since top squark production and decays are diverse and complicated and warrant a separate study [31].

Divergences incurred while calculating the Feynman diagrams for these processes are regulated by introducing a renormalization scheme and a mass scale. Cross sections calculated to all orders of pertubation theory do not depend on the renormalization scheme. However, ISAJET calculates cross sections only to leading order, and the truncated series exhibits renormalization scale dependence. The arbitrariness of

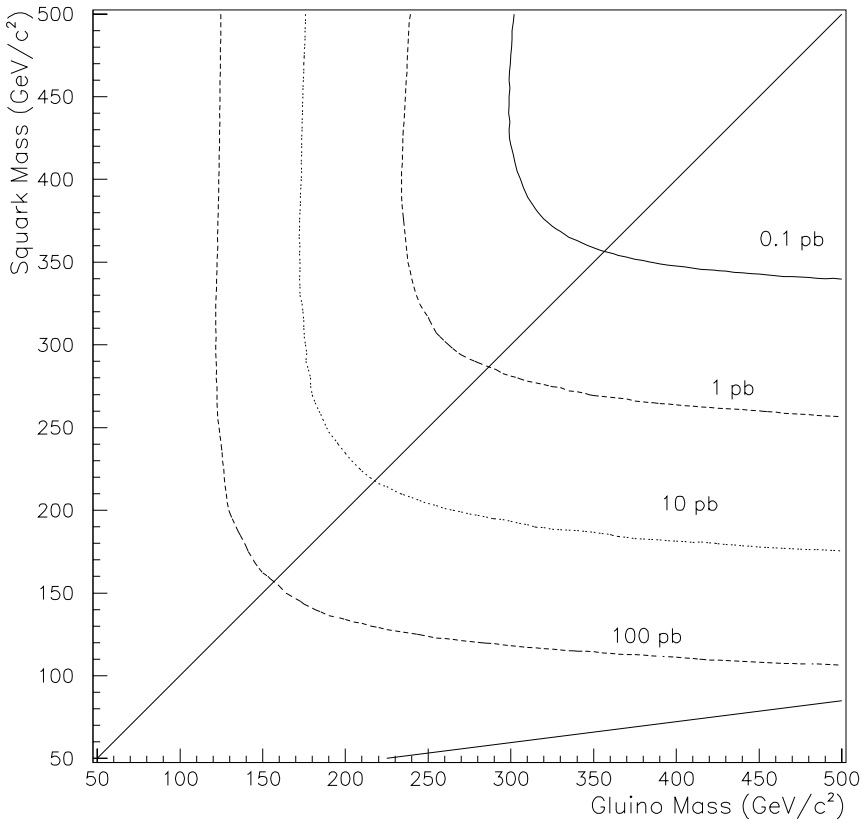


Figure 1.3: Cross section for squark and gluino production at the Fermilab Tevatron. The contours represent production cross sections of 0.1, 1, 10, and 100 pb. Below the contour at the bottom right corner, no cross section was computed because the squark mass is not allowed to be much smaller than the gluino mass before it becomes the LSP [16].

the scale choice corresponds to an uncertainty in the cross section. The renormalization mass scale is usually chosen to be equal to the typical energy scale in the process, where the theoretical predictions are less sensitive to its variation. Cross sections in ISAJET were evaluated with the renormalization scale set to $\hat{s}$ (the center of mass energy of the colliding proton and antiproton). By varying the scale choice from $\hat{s}/4$ to $4\hat{s}$, the uncertainty in the cross section was determined to be about a factor of two [32]. The mass renormalization scale choice introduces the largest uncertainty in the calculation, and this would change a derived mass limit by less than $\pm 20$ GeV/c$^2$.

A next to leading order calculation would be less sensitive to the scale choice. There has recently been a next to leading order calculation of the cross section for squark-squark production at the Fermilab Tevatron [34]. This relatively new calculation indicates that the cross sections determined from ISAJET may be about 25% too low. This would increase a mass limit by about 8 GeV/c$^2$.

The proton (antiproton) distribution function, and its structure function, are the probability that a parton (gluon or quark) carries a certain momentum fraction of the nucleon's total momentum. A contribution to the cross section uncertainty comes from the choice of structure function. The CTEQ2L structure functions [33] were used in the cross section calculations. Since a large fraction of the proton's (antiproton's) energy is necessary for the production of heavy objects, the choice between structure functions (which differ mainly at lower momentum fractions) makes little difference. Figure 1.3 shows the production cross section contours in the squark–gluino mass plane.

## 1.5 Terminology and Definitions

In describing the detector and event configuration, cartesian and cylindrical coordinates are used. A right-handed coordinate system is used where the $z-$axis is along the proton direction and the $y-$axis is upward. The $r-$coordinate is the distance perpendicular to the beam axis. The angle $\varphi$ is the azimuthal angle measured from the $x-$axis in the plane perpendicular to the proton beam. The angle $\theta$ is the polar angle measured from the incoming proton direction where $\theta = 0$ is along the proton beam direction.

Momentum transverse to the colliding beams is defined as $p_T = p \sin\theta$. For particles of equal mass and with equal but opposite momentum, the total momentum before and after collisions is $\sum_i^{\text{particles}} \vec{p}_i = 0$. The "energy vector" in the calorimeter is defined as

$$E_x = \sum_i^{\text{cells}} E_i \sin\theta_i \cos\varphi_i$$

$$E_y = \sum_i^{\text{cells}} E_i \sin\theta_i \sin\varphi_i$$

$$E_z = \sum_i^{\text{cells}} E_i \cos\theta_i$$

where $E_i$ is the energy deposited in calorimeter cell $i$, and $\theta_i$, $\varphi_i$ are the polar and azimuthal angles of a vector from the interaction point to the center of calorimeter cell $i$, and the sum is taken over calorimeter cells. This energy vector is approximately equal to the total momentum vector of all particles that deposited their energy in the calorimeter.

Pseudorapidity is defined as $\eta = -\ln(\tan\frac{\theta}{2})$. For highly energetic particles where $E \gg mc^2$, $E^2 = m^2c^4 + p^2c^2$ then $E \sim pc$. Pseudorapidity approximates the true rapidity $y = \frac{1}{2}\ln(\frac{E+p_xc}{E-p_xc})$ for finite angles in the limit that $\frac{mc^2}{E} \to 0$.

For colliding beams with equal momenta, total momentum before a collision is zero. Particles from spectator partons are produced at small $\theta$ angles and escape

Table 1.5: Units used in high energy physics compared with their equivalence in the SI system.

| Units | High Energy Physics | SI System |
|---|---|---|
| Energy | GeV | $10^9$ electron Volts $= 1.6 \times 10^{-10}$ joules |
| Mass | GeV/c$^2$ | $1.78 \times 10^{-27}$ kg |
| Cross Section | pb | $10^{-12}$ barns $= 10^{-40}$ m$^2$ |

undetected in the beam pipe. However, these particles have very small transverse energies, so that the total transverse energy can be measured accurately for the event.

Transverse energy is the energy directed in the direction transverse to the beam. For colliding beams of opposite directions (such as at the Fermilab Tevatron), the total transverse energy before and after any collision is identically zero. The total scalar transverse energy is measured after the collision and is defined as

$$S_T = \sum_i^{\text{cells}} E_i \sin\theta_i$$

with units of energy, GeV. Similarly, missing transverse energy $\not{E}_T$ is defined as

$$\not{E}_T = (\not{E}_x{}^2 + \not{E}_y{}^2)^{\frac{1}{2}}$$

where

$$\not{E}_x = -\sum_i^{\text{cells}} E_i \sin\theta_i \cos\varphi_i$$

$$\not{E}_y = -\sum_i^{\text{cells}} E_i \sin\theta_i \sin\varphi_i$$

and is measured in units of energy.

Various units used in high energy physics are shown in Table 1.5.

# CHAPTER 2
# EXPERIMENTAL APPARATUS

The DØ detector, located at the Fermi National Accelerator Laboratory in Batavia, IL, is a general purpose particle detector designed to detect the particles produced in the $p\overline{p}$ collisions. It is optimized to observe evidence of new phenomena by efficiently detecting leptons and accurately measuring energies transverse to the colliding beams. The construction of the experiment, originally proposed in 1983 [35], was completed in 1992 when the finished apparatus was rolled into the collision hall.

The DØ detector consists of three separate detector subsystems (see Figure 2.1): the central tracking system, the calorimeter, and the muon system. The central tracking system is closest to the beamline to provide vertex as well as charged track information. The calorimeter is a hermetic uranium/liquid argon sampling calorimeter that provides excellent energy resolution and particle containment. The muon system resides outside the calorimeter for full solid angle detection of muons with a momentum measurement determined by the particle deflection in the magnetic field provided by a toroidal magnet. The total number of detector channels is approximately 70,000 with some 5.5 million meters of cable and 1000 high voltage power supplies. The DØ detector has been documented in detail in reference [36].

## 2.1 Fermilab Tevatron Collider

The Fermilab Tevatron is a large proton synchrotron 1 km in radius, constructed from superconducting magnets with a peak energy of 900 GeV. It has been modified

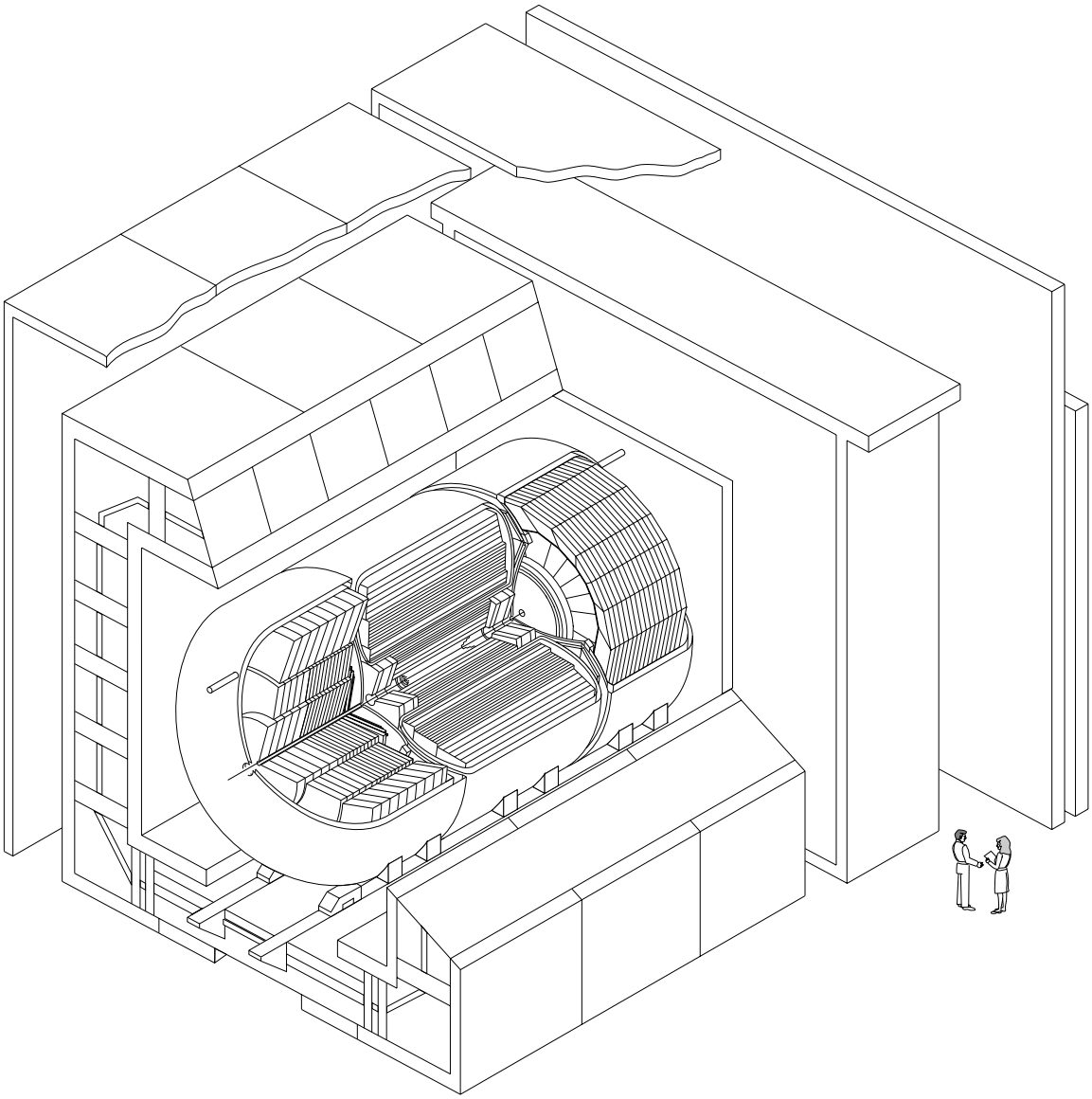

**DØ Detector**

Figure 2.1: A cutaway view of the full DØ detector. The central detector system is shown closest to the detector center, and surrounding it is the uranium/liquid argon sampling calorimeter, with its accompaning steel cryostat. The magnet toroids for the muon spectrometer surround the calorimeter. The Main Ring beam line resides above the center of the detector.

to allow operation as a proton-antiproton collider. When the Tevatron is run in the collider mode, bunches of protons and antiprotons are stored in the ring, circulating opposite to each other. The bunches encounter each other at a number of points along the ring. They are allowed to collide at the regions where experimental detectors are located. At the other crossing points they are prevented from colliding by separators which move the bunches out of each other's way. In 1985, the first colliding beams were produced in the Tevatron. Fermilab Collider Run Ia is the third collider run.

Protons and antiprotons first go through a linear accelerator and then a series of alternating gradient synchrotons: the Booster, Main Ring, and Tevatron. In a synchroton, particles are accelerated by radio-frequency cavities in a circular path. The maximum magnetic field available and size of the ring determines the final beam energy. The Booster and Main Ring synchrotrons are made of conventional copper-iron magnets, whereas the Tevatron was built with superconducting magnets allowing for a high final beam energy. The superconducting magnets are cooled with liquid helium kept at 4.6 Kelvin.

The protons originate from a negatively charged hydrogen ion ($H^-$) source that serves as input to a 750 keV Cockcroft-Walton electrostatic accelerator and provides approximately $1.4 \times 10^{14}$ $H^-$ ions/sec. A linear accelerator then accelerates the ions to 200 MeV. The $H^-$ is stripped of electrons in a charge exchange before injection into the Booster which raises the proton energy to 8 GeV. The protons are next injected into the Main Ring and accelerated to an energy of 150 GeV before transport to the Tevatron Ring.

Antiprotons were chosen for the collisions since the protons and antiprotons can circulate in the same path in opposite directions. The antiproton source is comprised of a target station, the Debuncher Ring, and the Accumulator Ring [37]. Protons are extracted from the Main Ring with 120 GeV energy and directed onto a target disk

of nickel. The secondaries from the target are focused with a lithium lens. Lithium is chosen for its low density as a solid and small occurrence of antiproton absorption and multiple scattering. An azimuthal magnetic field is established in the lithium with a current of 0.5 amps. A pulsed dipole magnet selects exiting particles with 8 GeV/c momentum. The 8 GeV antiprotons are stored in the Accumulator and later injected into the Main Ring for acceleration to 120 GeV.

The Main Ring is designed to accept 8 GeV protons (antiprotons) and accelerate them to 120 GeV. Before leaving the Main Ring, the protons are coalesced into a bunch and then injected into the Tevatron. The proton bunches are stored at 120 GeV until 6 bunches are accumulated. The Main Ring and Tevatron ring are located in the same tunnel and both operate at 53 MHz, allowing for the high efficiency in transfering particles from Main Ring to Tevatron. Once six proton and six antiproton bunches are in the Tevatron, the proton-antiproton energy is raised to 900 GeV for a final collision center of mass energy of 1800 GeV.

The six proton bunches, as well as the six antiproton bunches are separated from each other in time by 3.5 $\mu$sec. The proton bunches circulate in opposite direction on the same orbit as the antiproton bunches, so that there are 12 bunch crossing points along the Tevatron ring. Each proton (antiproton) bunch typically contains about $150 \times 10^9$ ($50 \times 10^9$) particles per bunch. Each store lasts for typically 12 hours before the instantaneous luminosity is sufficiently degraded.

In collider Run Ia, the bunch orbits were separated with electro-static separators to produce helical orbits. This resulted in collisions only at two interaction points, the DØ and BØ experimental regions, called the luminous regions. The peak instantaneous luminosity for Run Ia was $1.0 \times 10^{31}\mathrm{sec}^{-1}\mathrm{cm}^{-2}$. Quadrapole magnets were on either side of the luminous regions to reduce the beam spot size to $\sigma_{x,y} \approx 40$ $\mu$m. The quadropoles were not of equal strength surrounding the DØ luminous region, resulting in the interaction vertex being shifted by 10 cm in $z$ from the center of

the detector. The vertex position along the beam axis varied from event to event due to the finite bunch size. The distribution of event vertices measured by the DØ tracking chambers was $\sigma_z \approx 30$ cm.

One bunch revolution takes about 21 $\mu$sec and is split into 1113 states corresponding to RF buckets, a frequency of about 53 MHz. The bunches are not equally spaced since there is an odd number of RF buckets, and the bunch spacing alternates between 186 and 187 buckets. A timing signal is sent from the Tevatron to the DØ detector master clock system coherent with the bunches in the accelerator.

## 2.2 Calorimeters

A calorimeter intercepts particles and measures the energy deposited via a cascade or shower of decreasingly lower energy particles. The incoming particle loses energy by interacting with the absorbing medium to create new particles with smaller energies. A sampling calorimeter is made of a number of active layers interspersed with passive absorber. The signal is extracted from the active layers. Calorimeters are sensitive to both charged and electrically neutral particles. Calorimeters may be constructed to distinguish between particles (such as hadrons, electrons, muons) based on characteristic shower paterns. A calorimeter can be made to contain high energy particle showers, because the size of the calorimeter scales as $\log(E)$ [38] with the particle energy it can absorb. Calorimeters are ideal for measuring global event characteristics such as total scalar $E_T$, $\not{E}_T$, and jet production (see Section 4.2). Calorimeters can be segmented to allow for measurements of the direction of particles and to aid in triggering (by ganging the segmented cells into towers).

In a sampling calorimeter, highly energetic particles produce particle showers that develop in the absorber. The energy resolution for a calorimeter is statistically

dependent on the number of particles in the shower. A calorimeter produces a signal that is proportional to the energy of the incoming particles and with energy resolution that is proportional to $1/\sqrt{E}$. The statistical variation in the energy deposited into the active layers is called sampling fluctuation.

Since a high energy jet may contain an unknown fraction of electromagnetic and hadronic energy, a uniform response to both types of showers is important for consistent energy measurement among jets. The size of the gaps between the absorber and the active medium type of absorber and active medium are optimized for good electron/hadron response, as close as possible to compensation, where response to a purely electromagnetic shower is the same as the response to a purely hadronic shower of equal energy, i.e. $e/h = 1$. Noncompensation contributes a small constant term to the energy resolution.

### 2.2.1 Electromagetic Showers

High energy electrons and photons with $E > 1$ GeV primarily lose energy by Bremsstrahlung and pair-production. Electrons and positrons interact with the nuclear electric field that radiates photons and alters the incident particle's directon. The amount of deviation is usually small and depends on the atomic number of the absorber (strength of the electric field). As the electron energy diminishes, shower multiplication eventually stops at the critical energy, where ionization dominates.

A unit frequently used to describe the shower characteristics is called a radiation length. The radiation length ($X_0$) is material-dependent and is the distance over which a high energy electron ($> 1$ GeV) loses on average $1 - 1/e$ of its energy by Bremsstrahlung. The laws of quantum electrodynamics dictate the electromagnetic shower development and energy loss mechanisms for interactions with the Coulomb field. They are simulated in detail with Monte Carlo techniques, where random processes too complex to derive analytically are simulated on a computer with pseudorandom numbers.

### 2.2.2 Hadronic Showers

When hadrons (strongly interacting particles) of high energy traverse dense materials, their interactions with the protons and/or neutrons of the nuclei will lead to the production of new hadrons, which in turn will produce secondaries by strong interaction with the absorber nucleons, thus causing a "nuclear or hadronic cascade or shower" to develop. The more complicated nature of the strong interaction and the wide variety of shower particles that can be produced make the hadronic showers much more difficult to calculate than the relatively simple electromagnetic showers. Also, some of the energy lost by a hadron in a dense absorber may be used for excitation of nuclei, or to produce shower particles whose presence in the absorber does not give measurable signals (e.g. muons, neutrons,...). Thus, in general, the energy measured in the calorimeter due to a hadron depositing its energy is smaller than that due to a particle of the same energy losing its energy by an electromagnetic shower. The situation is further complicated by the fact that a pi0 can be produced in a hadronic reaction which via its decay into two photons initiates an electromagnetic shower, thus making part of the shower initiated by a hadron electromagnetic in nature. The large variety of possible processes mentioned leads to much wider fluctuations in the value of the seen energy for hadronic showers than for electromagnetic showers. As a consequence, the "energy response" (energy seen per energy lost in the calorimeter) is in general smaller for a hadronic shower than for an electromagnetic shower, a fact which in general is referred to as "$e/h > 1$". Furthermore, since a variable fraction of a hadronic cascade can become electromagnetic, and due to the other possibilities whereby the energy seen in a hadronic shower can fluctuate, the hadronic energy resolution is in general worse than the elecromagnetic one.

A hadronic calorimeter measures the energy deposited by particles by their nuclear interactions. The hadronic calorimeter is coarsely divided longitudinally and

primarily measures energy by particle showers that knock out protons and neutrons from the nuclei of detector atoms. The hadronic energy resolution is dominated by sampling fluctuations which cause an unevenness in the energy deposit. The energy resolution for hadrons is broader because of secondary particles like $\mu$, $\nu$, neutrons and $K_L^0$ that partly escape. The probability for a hadron to not interact via nuclear interaction after traversing a depth $x$ is $P(x) = e^{-x/\Lambda}$, where $\Lambda$ is called the interaction length. The nuclear interaction length is the mean free path of a hadron and depends on the substance.

## 2.3 DØ Calorimeter

The DØ calorimeter is a uranium liquid argon sampling detector with $4\pi$ full angular coverage for detection of electrons, photons, and hadrons, see Figure 2.2. The DØ calorimeter was constructed to contain nearly all of the particles produced in $p\overline{p}$ collisions, as represented in Figure 2.3. DØ measures $\not{E}_T$ well because of the good overall energy resolution of the calorimeter and the hermeticity of the calorimeter — cracks and dead material were kept at a minimum. Endcap cryostats were chosen to provide a pseudorapidity range down to $|\eta| = 4$ and to allow access to the central detectors. Some of the advantages of liquid argon are: nearly compensating, low cost, high density, good electron mobility, non-flammable, and radiation damage resistant. A disadvantage is that it must be operated cold in an accompanying cryostat, expensive in both cost and inactive material.

The calorimeter was made to measure two types of particle showers, electromagnetic and hadronic particle showers. A tower structure is used to allow for simple trigger design. The towers were segmented in units of pseudorapidity, $\Delta\eta = 0.1$, and phi, $\Delta\varphi = 2\pi/64$, except for the third electromagnetic layer where the electron

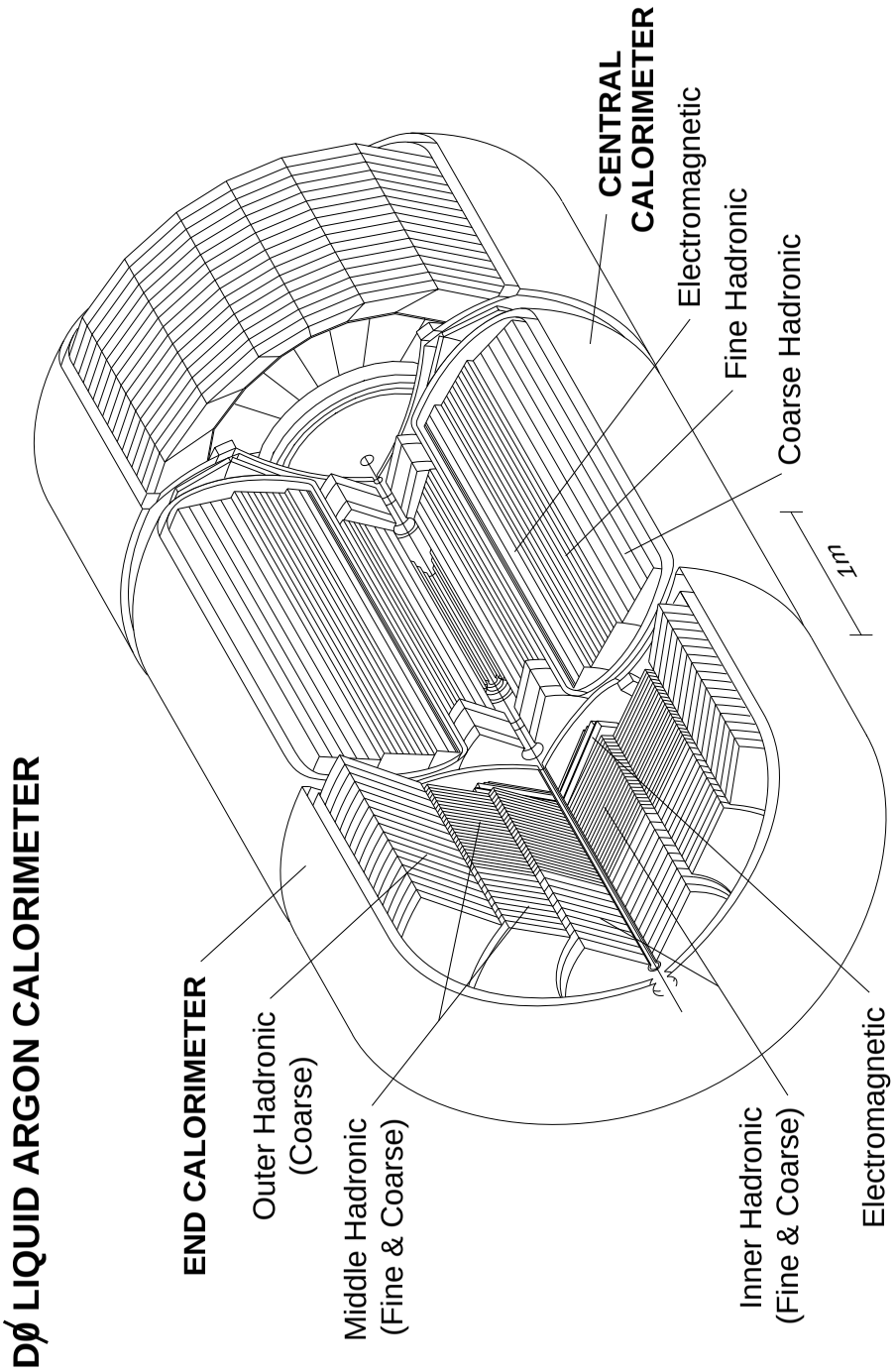


Figure 2.2: DØ calorimeter.

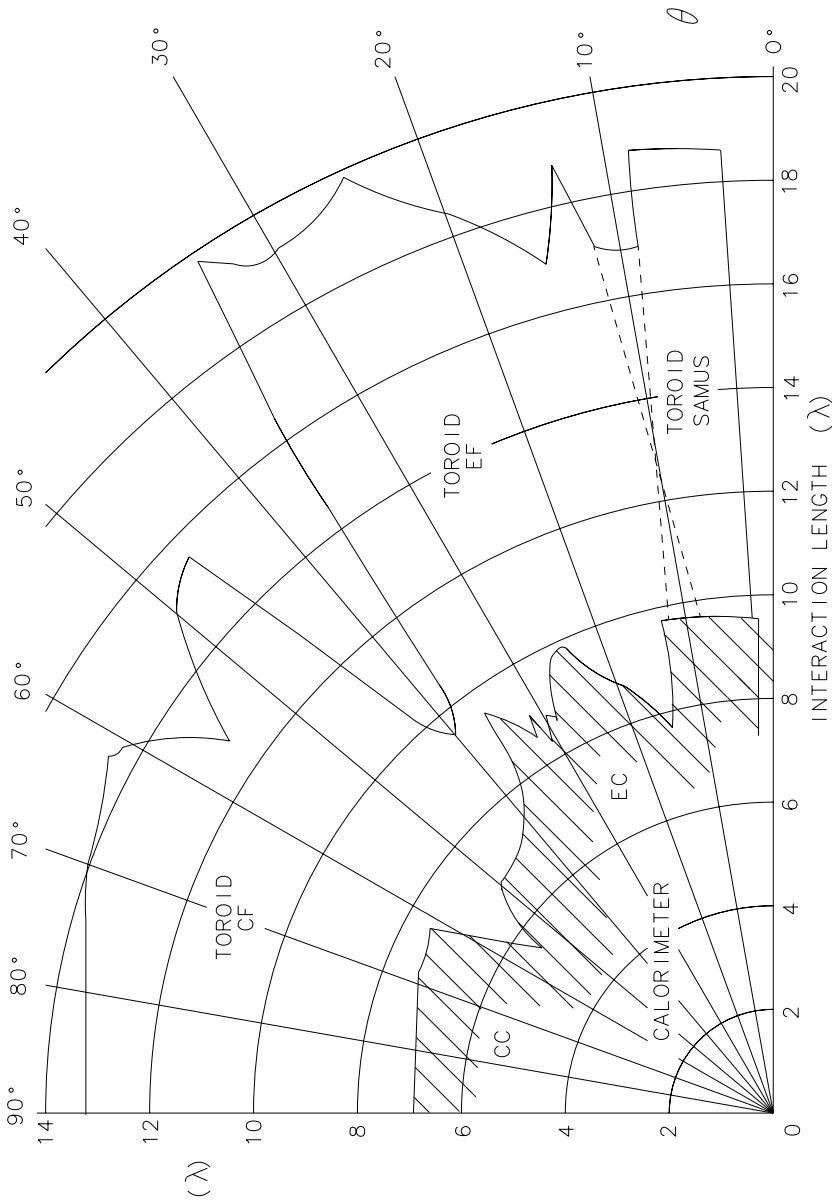


Figure 2.3: This is a pictorial representation of the DØ calorimeter displayed in interaction lengths by $\eta$. The calorimeter is constructed to contain 95% of the highest energy hadronic showers produced from the $p\overline{p}$ collisions. The center of the calorimeter is 7.2 interaction lengths deep and at high $\eta$ the end calorimeter is 10.3 interaction lengths.

shower has its maximum spread, $\Delta\eta = 0.05$, and $\Delta\varphi = 2\pi/128$. The minimum cell size was determined by matching the typical partonic jet transverse size of $R = (\Delta\varphi^2 + \Delta\eta^2)^{\frac{1}{2}} = 0.5$. A smaller size was built to allow for shower studies. Each tower is sampled in four electromagnetic and four hadronic layers. The Main Ring passes through the three cryostats above the centerline where the Tevatron beam line is positioned. Effects on data analysis due to the Main Ring are discussed in Section 5.2.2.

The liquid argon is cooled to a final operating temperature of 78 K. Double walled stainless steel cryostats contain forty layers of superinsulation filling the inner vacuum space. Oxygen has a high affinity for electrons and reduces the calorimetric energy response. The $O_2$ contamination is less than 0.6 ppm, and is monitored with a radioactive $\beta$ source.

A sampling calorimeter cell consists of a depleted uranium absorber plate, a liquid argon gap, G-10 signal board, and a second liquid argon gap. The variation in thickness of the uranium plates is less than 2.3%. The Uranium plates act as absorber material, while the liquid argon plays the role of the "active medium": the charged particles produced in the shower ionize the liquid argon when traversing it. The G-10 signal board is coated with high resistivity epoxy to provide an electrode which is maintained at 2.5 kV with respect to the Uranium plates which are at ground potential. The electric field between the Uranium plates and the resistive coating causes the charge from the ionization of the liquid Argon to be collected on the electrode. An interior surface of the read-out board has copper pads in the shape of the desired read-out segmentation. By capacitive coupling, a charge collected on the resistive coating causes a signal on the nearest copper pad which is then transported to the preamplifier.

Tefzel 30 $\Omega$ coaxial cables bring signals out of the liquid argon cryostats and into a charge-sensitive preamplifier with shaping circuits (BaseLine Subtractors)

to counteract the reactance in the long cables that alters the signal shape. The signal is integrated just before beam crossing and 2.2 $\mu$sec after the beam crossing. The output is sent to 12-bit analog to digital converters (with an extension of the dynamic range by amplification of either 1 or 8 times) to measure the DC output of the BLS circuits that is proportional to the measured charge. One least count corresponded to 3.75 MeV of energy, where a minimum ionizing particle deposits between 8 and 90 MeV, depending on the layer. A pulser is used to inject charge into the electronics at various stages for calibration.

### 2.3.1 Electromagnetic Calorimeter

The electromagnetic (EM) calorimeter was designed for electron identification and energy measurement. The EM calorimeter was built to contain high energy electrons and extends out to approximately 20 radiation lengths, see Figure 2.3. The EM section is comprised of relatively thin uranium plates sandwiched with liquid argon and G-10 signal board. The electron energy resolution and electron to hadron response in the calorimeter was determined from testbeam studies [39], see Table 2.1.

### 2.3.2 Hadronic Calorimeter

The hadronic calorimeter was designed to detect and measure jets containing hadronic particles which pass through the electromagnetic section. The hadronic calorimeter has a deep interaction length for containment of hadronic particles, see Figure 2.3. The hadronic calorimeter section is separated into 4 independent layers for readout. The pion energy resolution was measured from test beam measurements [40], and is shown in Table 2.2.

Table 2.1: Characteristics of the calorimeter electromagnetic section.

| | Electromagnetic |
|---|---|
| $\eta$ range | $\lvert\eta\rvert < 1.1$, $1.4 < \lvert\eta\rvert < 4.0$ |
| Liquid Argon Gap | 2.3 mm |
| Absorber plates | 3 mm uranium |
| Number of Readout Layers | 4 |
| Total $X_0$ (at $\eta = 0$) | 20.5 |
| Total $\Lambda$ (at $\eta = 0$) | 0.76 |
| Uranium | $X_0 = 0.32$ cm |
| Electron Energy Resolution | $15.5\%/\sqrt{E}$ |
| Electron to Hadron response | 1.04 |

Table 2.2: Characteristics of the calorimeter hadronic section.

| | Hadronic |
|---|---|
| $\eta$ range | $\|\eta\| < 4.0$ |
| Liquid Argon Gap | 2.3 mm |
| Absorber plates | 6 mm uranium (fine) |
| | 47 mm copper (coarse) |
| Number of Readout Layers | 4 |
| Total $X_0$ (at $\eta = 0$) | 128.9 |
| Total $\Lambda$ (at $\eta = 0$) | 6.4 |
| Hadronic Energy Resolution | $41\%/\sqrt{E}$ |

### 2.3.3 Intercryostat Detector

The area between the central and end cryostats, called the intercryostat region, contains support structures. Scintillator tiles were placed in this region to detect any particles otherwise unmeasured by the calorimeter. The intercryostat detectors (ICD) were mounted on the outer surface of the end cap calorimeters [41].

The 384 scintillator tiles were segmented to match the calorimeter as $\Delta\eta = 0.1$, $\Delta\varphi = 32\pi/64$. These tiles were made from Bicron BC-414 scintillator with 3 mm grooves to allow 0.2 mm polystyrene wavelength-shifting scintillating fibers to collect the light produced in the tiles and transport it to a phototube to measure the light yield. The typical minimum ionizing particle produced approximately 20 photoelectrons detected by the phototube.

## 2.4 DØ Tracking System

The DØ tracking system is comprised of drift chambers including a vertex detector, central and forward drift chambers, and a transition radiation detector. The tracking system is located closest to the collision point and detected trajectories of charged particles in gas. The vertex position of each $p\overline{p}$ collision is determined by analyzing the tracks of particles from the central tracking system.

Drift chambers measure the spatial position of charged particles. A charge is collected on the sense wires produced by ionization from the traversing charged particle. A high voltage on the wires attracts the ionized particles for collection.

Response of the central detectors is expected to vary with gas content and changes in atmospheric conditions. Small test chambers measure the response to a radioactive source to detect changes in the gas composition.

### 2.4.1 Vertex Chamber

The vertex chamber, a drift chamber, is used to detect charged particle trajectories arising from proton-antiproton interactions [42]. The chamber is the closest detector to the Tevatron ring and interactions and constructed of three layers of cells supported by G-10 material and mounted on carbon fiber support tubes. Each cell contains 8 wires staggered in $\varphi$ to remove left-right ambiguity and provide position information. Sense wires are read out from each end and the integrated charge and timing information from the wire is used to measure the $z$ position. Table 2.3 lists the construction details for the vertex chamber.

### 2.4.2 Transition Radiation Detector

A transition radiation detector (TRD) surrounds the vertex chamber, see Table 2.4. It is used to distinguish between electrons and hadrons with energies up to 200 GeV. Discrimination between electrons and pions is accomplished by comparing the amplitude and timing of the X-ray spectrum produced when highly relativistic

Table 2.3: Characteristics of the vertex chamber.

| | |
|---|---|
| Layers | 3 |
| Radius | 3.7 cm (inner), 16.2 cm (outer) |
| Phi Sectors by Layer | 16/32/32 |
| Sense Wires/Cell | 8 |
| Sense Wires | NiCoTin |
| Sense Wire Stagger | 100 $\mu$m |
| Maximum Drift Distance | 13.7 |
| Field and Grid Wires | 152 $\mu$m Gold Plated Aluminum |
| Gas | $CO_2/C_2H_4$ |
| Track Resolution | 63 $\mu$m |
| Pair Resolution | 7 mm |

particles (where the Lorentz factor $\gamma = 1/\sqrt{1-(v/c)^2} > 10^3$) traverse the boundary between media with different dielectric constants producing transition radiation X-rays. The total energy radiated by a single interface between two media is proportional to the Lorentz factor $\gamma$; the total energy emitted by an assembly of foils of finite width reaches a limiting value as $\gamma \to \infty$ which depends on the number of foils and other properties of the detector [43]. The X-rays were detected by a proportional wire chamber surrounding the conversion stage.

The TRD consists of three separate chambers each with a conversion stage and an X-ray detection chamber or amplification stage. The two stages are separated by a cathode grid. The conversion stage is made of radiator foils. The X-ray energy spectrum peaks at 8 keV and is detected by a proportional wire chamber. Conversions into charged particles takes place in the first few millimeters and the charged clusters are detected by sense wires.

### 2.4.3 Central and Forward Drift Chambers

Drift chambers surrounding the TRD chamber are used to detect the trajectories of charged particles [44], see Table 2.5. The central drift chamber (CDC) surrounds the TRD chamber, is parallel to the colliding beam direction, and is used for measuring the trajectories of charged particles for vertex position determination. The forward drift chamber (FDC) extends the coverage for charged particle tracking (down to $\theta \approx 5^o$) and is perpendicular to the colliding beam direction at either end of the vertex detector.

Charged particles traversing the chambers interact with the gas in the chamber leaving an ionization trail that is collected on sense wires. High voltage wires were used to produce an electric field causing the ionization trail to drift toward the sense wires. Field shaping is accomplished by resistive strips on the cathode surfaces.

Table 2.4: Characteristics of the transition radiation detector.

| | |
|---|---|
| Layers | 3 |
| Wires/Layer | 258 |
| Conversion Stage | 393 radiator foils |
| Foils | 18 $\mu$m polypropylene, 150 $\mu$m gaps filled with N gas |
| Inner Cathode | 70 $\mu$m gold-plated tungsten wires |
| Potential Wires | 100 $\mu$m copper-beryllium wires |
| Anode | 30 $\mu$m gold-plated tungsten wires |
| Outer Cathode | helical copper strips deposited on Kapton foil |
| Gas | Xe(91%)/$CH_4$(7%)/$C_2H_6$(2%) |
| Drift Time | 0.6 $\mu$sec |
| Electron to Pion Rejection | 1/10 |

Table 2.5: Characteristics of the central and forward drift chambers.

| | |
|---|---|
| Gas | $Ar(92.5\%)/CH_4(4\%)/CO_2(3\%)/H_2O(0.5\%)$ |
| Sense Wires | 30 $\mu$m gold-plated tungsten wires |
| Voltage | 1.45 kV |
| Drift Distance | 5.3 cm |
| Sense Wire Stagger | 200 $\mu$m |
| Central Drift Chamber | |
| Layers | 4 |
| Cells/Layer | 32 |
| Wires/Cell | 7 |
| Sense Wire Resolution | 200 $\mu$m |
| Pair Resolution | 10 mm |
| Forward Drift Chamber | |
| Chambers | 3 (on each end) |
| Theta Sectors/Quadrant | 6 |
| Theta Quadrants | 4 |
| Wires/Theta Sector | 8 |
| Phi Sectors | 36 |
| Wires/Phi Sector | 16 |
| Range | $\theta > 5$ degrees |
| Position Resolution | 200 $\mu$m |

Within a cell, two delay lines (one delay line in the FDC) embedded in the inner and outer shelves are read out at both ends. The difference of arrival times at the delay line ends is used to measure the track $z$-position. Sense wires are staggered in $\varphi$ ($z$ in the FDC) by $\pm 200$ $\mu$m to remove left-right ambiguity.

The vertex position and event multiplicity in this analysis is primarily found using the central drift chamber ($> 90\%$ of the time) and forward drift chambers.

## 2.5 DØ Muon System

The muon system was designed to determine the momentum and position of muons produced in the high energy collisions. The muon detector is made of solid-iron toroidal magnets and proportional drift tube chambers. Muons interact with matter via electromagnetic interactions. For high energy muons, energy loss by radiative processes (e.g. Bremsstrahlung) become significant compared to that by ionization and becomes dominant at muon energies above a few hundred GeV.

The large interaction length of the calorimeter and the presence of iron in the muon detector allow nearly all of a jet to be contained in the calorimeter, leaving only muons and weakly interacting particles to traverse the muon chambers. The characteristics of the muon system are shown in Table 2.6.

The iron toroids are separated into a wide angle muon system (WAMUS) [45] and a small-angle muon system (SAMUS) that covered large pseudorapidity. The proportional drift tubes are oriented in the same direction as the magnetic field and with one layer before the and two layers after the toroids. The chamber planes are offset to allow breaking of the left-right drift-time ambiguity. The WAMUS copper-clad cells are made of Glasteel cathode pads, polyester and epoxy copolymer sheets with chopped glass fibers.

Table 2.6: Characteristics of the muon chambers. The momentum resolution is the multiple scattering limit assuming 100% chamber efficiency.

| | |
|---|---|
| Magnetic Field Strength | 2 Tesla |
| Cells | 5308 (WAMUS) |
| Muon Sign | $p_T < 200$ GeV/c at $\eta = 0$ |
| | $p_T < 30$ GeV/c at $\eta = 3.3$ |
| Momentum Resolution | $20\% \leq \delta p/p \leq 50\%$ |
| Interaction Lengths | 13-18 |

There are two methods of determining the hit position on a wire. Either the time difference for the pulse read from each end of the anode or the signals from cathode pads could be used. The cathode pad signals are amplified with a charge sensitive preamplifier, sent to a baseline subtractor that reads the signal before and after the event, and subsequently read out with 12-bit ADC circuits. The anode signals are discriminated from each end with time to voltage hybrid circuits.

There are several background sources which cause a muon chamber to misidentify an object, such as a cosmic ray, as a muon from a $p\overline{p}$ interaction. Punchthroughs are any track in the muon detector produced by a hadron incident on the calorimeter. Interacting hadrons may produce muons from secondary particles.

# CHAPTER 3
# TRIGGER AND DATA ACQUISITION

The purpose of the DØ triggering and data aquisition system is to select events of interest and save them for future analysis [46]. The data acquisition system is required to reduce the collision rate of 100 kHz to a rate of 2 Hz for writing to tape. Because of the large number of electronic channels, the data acquisition system also selectively reads only those channels thought to have important event information.

There are four levels of triggers:

- Level 0: This is a trigger implemented in hardware consisting of scintillation counter signals. The collision cross section is $\sim 47$ mb, with a collision rate of approximately 100 kHz.

- Level 1: Calorimeter and muon chamber information is used here with an input rate of $\sim 10$ kHz.

- Level 1.5: Used only by the muon triggers (in Run Ia).

- Level 2: This is a trigger implemented on a farm of $48 - 4000/60$ VAX computers for fast software analysis of each event and reduced the event rate from 100 Hz to about 2 Hz for writing to 8mm tapes.

The Level 0 and Level 1 triggers are implemented in hardware, with a decision time shorter than the time between bunch crossings to cause no data aquisition dead time. However, once the Level 1 decision is made to pass the event to Level 2 triggers, the time require by the electronics to readout the detector channels accounts for less than 10% dead time. The Level 2 trigger decisions are implemented with software

and required a significant processing time, depending on the specific routines or tools that are necessary to analyze an event and to decide if it should be accepted or rejected. Studies that model this system have shown that the dead time was well under 2% [47]. A schematic legend of the DØ data acquisition system is shown in Figure 3.1.

## 3.1 Level 0 Trigger

The purpose of the Level 0 (L0) trigger system is to identify beam crossings containing non-diffractive inelastic collisions and to measure the instantaneous luminosity [48]. The L0 signal is also used to determine the $z$-coordinate of the interaction point for triggering and to detect multiple interactions. The L0 trigger counters are two arrays of hodoscope scintillation counters (Bicron BC-408 PVT scintillator) mounted on the front surface of the endcap cryostats: long counters with a photomultiplier tube (Philips XP-2282 photomultiplier) readout on both ends ($\sim$ 80 ps time resolution) and short counters with a photomultiplier readout only on one end (120 ps time resolution). Combined, the L0 scintillators provide nearly complete coverage over $2.2 < |\eta| < 3.9$ and partially covers the pseudorapidity region $1.9 < |\eta| < 4.3$.

The short counters provide a fast determination of the vertex position ("fast z"), using the time difference of the analog sums between the north and south arrays. Approximately 400 nsec after the beam crossing, the "fast vertex" is passed to the calorimeter Level 1 triggers for vertex position correction to correct the $\theta$-coordinate of each calorimeter cell. The calorimeter Level 1 trigger towers allow for corrections to the vertex in 8 cm increments, although this was not done in collider Run Ia.

The "slow vertex" position is calculated by using the average time from each photomultiplier tube on the long counters. The difference in average time for hits in

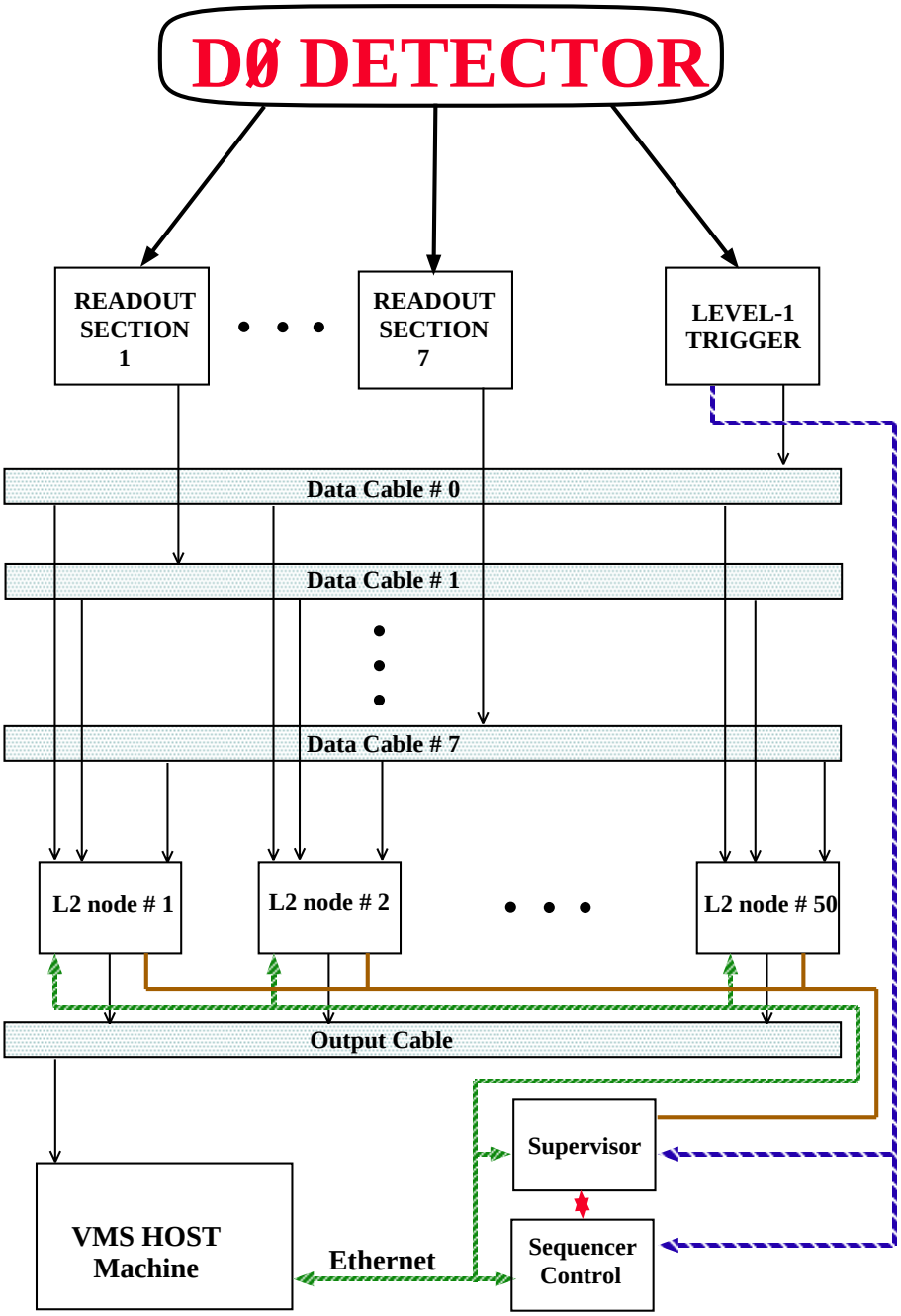


Figure 3.1: DØ Data Acquisition System

the north and south L0 arrays is available approximately 2 $\mu$sec following the beam crossing and is used by Level 2 triggers. If the spread in time between L0 arrays exceeds a programmable cut, then the interaction is flagged as a multiple interaction. If there is more than one interaction, then it is not possible for L0 to accurately determine the primary vertex position. Beam-halo, Main Ring backgrounds, and beam-gas collisions introduce errors in the L0 counting rate, although the vertex position is required to be to be within $|z| < 1$ meter of the center of the detector to reject interactions from beam-gas and beam-halo events.

## 3.2 Level 1 Trigger

The Level 1 (L1) triggers (32 specific L1 triggers) are used to reduce the rate from $\sim$ 10 kHz to under 100 Hz [49]. Projective towers pointing back to the center of the detector are subdivided in depth (see Figure 3.2) and used in triggering. Information from electromagnetic and hadronic trigger towers (segmented into divisions of $\eta$ and $\varphi$: $\Delta\eta = 0.2$ and $\Delta\varphi = 0.2$, see Section 2.3) is used in the L1 triggering up to $|\eta| \leq 4.0$. Each trigger tower sums the BLS circuits and is weighted by the $\sin\theta$ of the tower for the vertex postion as given by the Fast Vertex.

## 3.3 Level 2

Once an event passes a L1 trigger, the data are sent to one of 48 VAX station nodes connected to the detector electronics via eight 32-bit high speed data cables. Cables connected the VME crates in the moving counting house, grounded with the detector, through optical isolator circuits, to the fixed counting area where the Level 2 (L2) nodes are located.

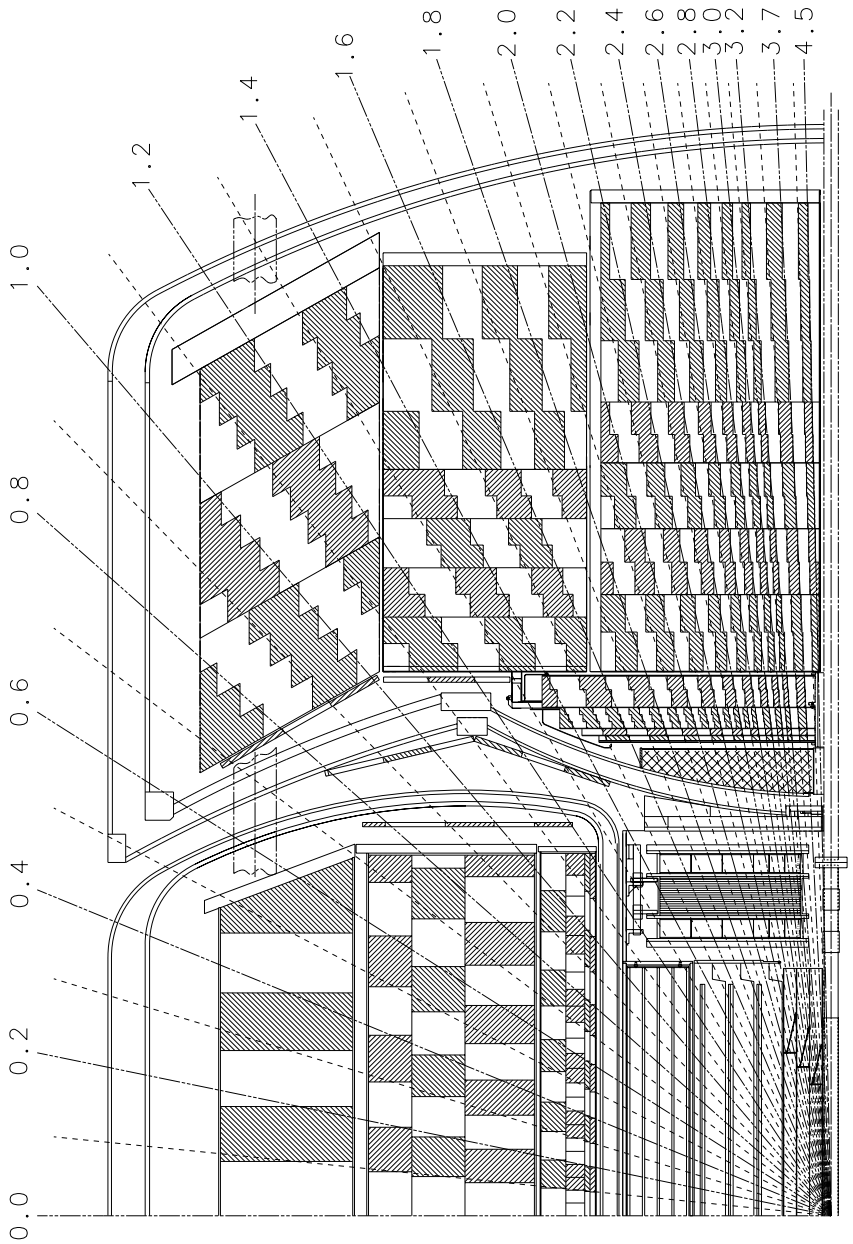


Figure 3.2: DØ Calorimeter cross sectional side view subdivided in pseudorapidity showing the segmentation in $\eta$ into "pseudoprojective towers" of size $\Delta\eta \times \Delta\varphi = 0.1 \times \frac{2\pi}{64}$. The labels of the straight lines that pass through the center of the detector denote $\eta = -\ln\tan\frac{\theta}{2}$.

Each L2 node is comprised of a VAX station 4000/60 processor and a VME Buffer Driver board for data transfer to the host computer. Software algorithms are used to determine if the event should be passed on to the host computer, a VAX 6620. Once sent to the host computer, the DATA LOGGER program writes the event to tape [50]. The L2 processing time is less than 200 msec per event. The L2 framework provides for 128 individual triggers, although fewer than 64 are used.

The available bandwidth for writing to the host computer is 1500 kbytes/sec and the typical event size is $\sim$ 500 kbytes. The actual rate of events out of L2 and written to 8 mm tapes is about 2 Hz. For collider Run Ia, about 13 million events were recorded on 3000 8 mm tapes for future retrieval and analysis.

### 3.4 Missing Transverse Energy ($\not\!\!E_T$) Trigger

The $\not\!\!E_T$ (defined in Section 1.5) for L1 was calculated by knowing the $x$ and $y$ components of the $E_T$ (with a threshold $>$ 500 MeV) for the electromagnetic and hadronic sections of the calorimeter. Various limitations of the $\not\!\!E_T$ trigger prevented the L1 calculation of $\not\!\!E_T$ from being very accurate. For example, the $E_T$ for each tower is not corrected by the vertex position, available from L0 called the fast vertex. Also, the energy deposits into the ICD and coarse hadronic layers are not included.

The L2 $\not\!\!E_T$ trigger uses raw calorimeter information. The $\not\!\!E_T$ L2 trigger filter tool used the CL2 fast calorimeter unpacking [51] and is calculated by

$$E_x = \sum E_T(\eta, \varphi, l) e_T^{\mathrm{corr}}(\eta, z) \cos\varphi$$

$$E_y = \sum E_T(\eta, \varphi, l) e_T^{\mathrm{corr}}(\eta, z) \sin\varphi$$

where $\eta$, $\varphi$, $l$ are the address of the cell, $E_T$ is the transverse energy for the cell with the nominal vertex position, and $e_T^{\mathrm{corr}}$ is the correction for the slow vertex to the

transverse energy from the nominal vertex position. Corrections for energy deposits in the ICD are included. Also, a routine to suppress anomalous energy deposits by finding isolated cells in energy was implemented [52]. The $\not{E}_T$ triggers were not active during the Main Ring cycle.

The triggers used in this analysis are the $\not{E}_T$ and Jet-Miss triggers, see Tables 3.1 and 3.2. The Fraction column shows the fraction (in percentage) of total data taken with that trigger configuration. Most of the data used Trigger Version 7.2. The symbols used in describing the trigger configurations are: MS($x$) means that at that trigger level, $\not{E}_T \geq x$ GeV; for L1, JT($n, x$) requires at least $n$ trigger towers with $E_T \geq x$ GeV; and for L2, L2J($n, x, r$) requires at least $n$ jets with $E_T \geq x$ GeV using a cone size of radius $r$. A $\not{E}_T$-significance parameter is used in the L2 trigger and was defined as

$$S_T = \frac{\not{E}_T}{(B + M \sum_i^{cells} E_{Ti})}$$

where $M = 0.029$, and $B = 0.9$ based on offline reconstructed $\not{E}_T$ and scalar $E_T$ [51]. The $\not{E}_T$-significance was required to be $S_T \geq 5$ for Trigger Version 6.0 and was not used for any other Trigger Versions.

## 3.5 Luminosity

For luminosity determination, the L0 system records the in-time hits for each Tevatron bunch, measuring the non-diffractive inelastic collision rate with 99% efficiency. Monte Carlo studies were used to determine the fraction of nondiffractive cross section seen by the L0 counters. The event rate out of L0 was typically 150 kHz. The L0 visible cross section used the non-diffractive cross section of (46.7$\pm$2.5) mb, as calculated by using a world average cross section and comparing unbiased DØ collider data to Monte Carlo event generators [53]. The total DØ integrated

luminosity for data written to tape was 13.5 $pb^{-1}$. In addition, approximately 1 $pb^{-1}$ of data was taken for calibration and special runs. Dead time due to the Main Ring was 9% and the overall data taking efficiency was 54%.

Table 3.1: $\not\!\!E_T$ Trigger History. The Fraction column is the fraction (in percentage) of total data taken with that trigger configuration.

| Version | L1 | L2 | Runs | Fraction (%) |
|---|---|---|---|---|
| 6.0 | MS(35)+JT(1,3) | MS(40) | 54965 - 55200 | 0.75 |
| 6.1 | MS(35)+JT(1,3) | MS(40) | 55217 - 55600 | 0.87 |
| 6.2 | MS(35)+JT(1,3) | MS(40) | 55601 - 56297 | 4.5 |
| 6.3 | MS(35)+JT(1,3) | MS(40) | 56298 - 57711 | 17 |
| 6.4 | MS(30)+JT(1,3) | MS(35) | 57712 - 58141 | 3.2 |
| 6.5 | MS(30) | MS(35) | 58142 - 59378 | 17 |
| 7.1 | MS(30)+JT(1,3) | MS(35) | 60100 - 62149 | 16 |
| 7.2 | MS(30)+JT(1,3) | MS(35) | 62150 - 64085 | 31 |
| 7.3 | MS(30)+JT(1,3) | MS(35) | 64086 - 65423 | 9.5 |

Table 3.2: Jet-Miss Trigger History.

| Version | L1 | L2 | Runs | Fraction (%) |
|---|---|---|---|---|
| 6.0 | MS(20)+JT(1,7) | L2J(1,20,0.3)+MS(20,5) | 54965 - 55200 | 0.75 |
| 6.1 | MS(20)+JT(1,7) | L2J(1,20,0.3)+MS(20,5) | 55217 - 55600 | 0.87 |
| 6.2 | MS(20)+JT(1,7) | L2J(1,20,0.3)+MS(25,0) | 55601 - 56297 | 4.5 |
| 6.3 | MS(20)+JT(1,7) | L2J(1,20,0.3)+MS(25,0) | 56298 - 57711 | 17 |
| 6.4 | MS(20)+JT(1,7) | L2J(1,20,0.5)+MS(25,0) | 57712 - 58141 | 3.2 |
| 6.5 | MS(20)+JT(1,7) | L2J(1,20,0.5)+MS(25,0) | 58142 - 59378 | 17 |
| 7.1 | MS(20)+JT(1,7) | L2J(3,20,0.5)+MS(25,0) | 60100 - 62149 | 16 |
| 7.2 | MS(20)+JT(3,5) | L2J(3,20,0.5)+MS(25,0) | 62150 - 64085 | 31 |
| 7.3 | MS(20)+JT(3,5) | L2J(3,20,0.5)+MS(25,0) | 64086 - 65423 | 9.5 |

# CHAPTER 4
# EVENT SELECTION

## 4.1 Data Collection

The data ($\sim$ 13 million events in total) were collected during Fermilab Collider Run Ia, including most runs from 54967 to 63827, 743 runs total, from October 1992 to April 1993. Once an event passed a specific filter, the raw data of that event ($\sim$ 0.5 megabyte) were stored on disk and spooled onto an 8 mm tape at a rate of approximately 2 events/sec.

The raw data were processed on a farm of 36 Silicon Graphics Crimson machines with 4D/35 processors provided by the Fermilab Central Computing Facility, using a program called DØRECO (which contained roughly 150,000 lines of code) that converted the digitized information from the detector electronics into physics variables (energy deposits, track directions, etc...). The reconstruction farm was capable of processing 90,000 events/day on the 36 33-MIP machines, and required approximately 30 cpu sec/event. Smaller format files containing the most interesting physics variables called Data Summary Tapes, or DSTs, were used to store data on disk, readily accessible with a size of approximately 0.5 megabytes/event. A larger, more complete file format called a Standard Tape stored data on 8 mm tapes at the Feynman Computing Center, with an event size of $\sim$ 1 megabyte.

Corrections to convert ADC counts into energy include pedestal subtraction, gain corrections for pulser variations, sampling fraction corrections, and corrections for variations in liquid argon gaps.

The measurement of $\not{E}_T$ can be spoiled by the inclusion of anomolous energy deposits from a source other than the interaction of interest. During data collection,

the pedestals measured by the CALIB program were used to suppress calorimeter channels that exhibited bad hardware behavior, usually fewer than 10 channels per run. Some noise had a lifetime shorter than the frequency at which the pedestals were taken. Those cells isolated in space were removed from the event before reconstruction of jets and $\not{E}_T$ calculations.

Cells containing an exceptional energy deposit with no other surrounding energy deposits that were found consistently throughout a series of runs, were removed from the reconstruction program so as to not affect the particle finding algorithms [54]. About half of the runs had no cells suppressed, and usually only one cell in any run required suppression. A separate routine in the reconstruction program (AIDA [52]) identified and eliminated high energy cells without neighboring hit cells on an event by event basis. These methods were found to be sufficient to eliminate the influence of noisy cells on the jet finding algorithm and $\not{E}_T$ calculation.

## 4.2 Jets

At very small distances, the QCD strong interaction between quarks and gluons are analogous to the electromagnetic force, while at larger distances the potential increases with distance confining the quarks inside a hadron. High energy collisions of hadrons will sometimes scatter the partons (quarks and gluons) with high transverse momentum, also called hard scattering. The strong color force of QCD will hadronize these partons into particles that cluster into groups along the initial parton direction; this is called a jet. Clusters of energy detected in the calorimeter are reconstructed to form the original parton jet. One such method is called the cone algorithm [55].

Partons have virtual gluons that surround them and for very energtic partons, a real gluon may be radiated. For example, a gluon emitted from an outgoing quark

is called gluon Bremmstrahlung or parton splitting. From quantum field theory, the probability that a parton may emit another parton is determined by a probability density function derived by solving the Altarelli–Parisi evolution equation [56].

### 4.2.1 DØ Cone Algorithm

The DØ jet definition is consistent with the Ellis, Kunszt, and Soper definition [57] and is as follows.

- Pre-clusters are formed by sorting calorimeter towers (in $\eta - \varphi$) in descending order of $E_T$.
- Only those towers with $E_T \geq 1$ GeV, called seed towers, are intially considered.
- Neighboring towers (within $\pm 0.3$ units of $\eta$ or $\varphi$) above a threshold of $E_T > 1$ GeV are joined to form a precluster.
- The $E_T$ weighted $\eta$, $\varphi$ of each precluster is calculated.
- Each precluster is used as the center of a cone. A cell is considered inside the cone if its distance $R$ from the center of the cone, $R = \sqrt{(\delta\eta)^2 + (\delta\varphi)^2}$ is smaller than a reference value $R_{\text{cone}}$. Standard values of $R_{\text{cone}}$ used in DØ are 0.3, 0.5, 0.7 and 1.0.
- All cells in a cone are added together to form a cluster.
- New $\eta$ and $\varphi$ are calulated using $E_T$ weighted $x$ and $y$ positions of the cluster.
- This procedure is repeated until the center of the cone is equal to the average $\eta$ and $\varphi$ of the cluster.
- If two clusters share more than 50% of their energy, they are merged into one cluster.

- Only clusters with $E_T > 8$ GeV are accepted as jets.

The measured jet $E_T$ occasionally does not equal the parton $E_T$: energy can be lost in uninstrumented parts of the detector such as cracks, energy from an underlying event can contribute energy inside the cone radius, or some jet energy may be outside the cone due to fragmentation effects. The jet energy resolution is determined from collider data to be $\sigma/E = 80\%/\sqrt{E}$.

## 4.3 Energy Corrections

The $\not\!\!E_T$ is determined by the measured energies in the detector. This physics analysis selected events based on the $E_T$ of the jets and the $\not\!\!E_T$. Thus, any systematic variation in the jet $E_T$ or the $\not\!\!E_T$ is important to this analysis.

The energy corrections applied to the DØ calorimeter can be summarized in two categories: calibration of the energy scale measured in the detector and corrections of jet energies due to the jet reconstruction algorithm. The jet energy is corrected in both data and Monte Carlo as accurately as possible in order to determine the final quark energy from the hard scattering process.

The DØ collider data jet energy was corrected by approximately 5% for out-of-cone particle showering, 6% for electromagnetic scale corrections, less than 10% for dijet $p_T$ balancing, and 5 to 20% for $\gamma/jet$ $p_t$ balancing [59]. The jet correction is dependent on both $\eta$ and jet energy.

At the time the preselection analysis cuts were applied to the data (see Section 4.5), uncorrected energies for the jet $E_T$ and the $\not\!\!E_T$ were used since the energy correction algorithms were not in place. The effects of the energy corrections on the $E_T$ of the leading jet (ordered by jet $E_T$) and $\not\!\!E_T$ after data streaming are shown in Figure 4.1.

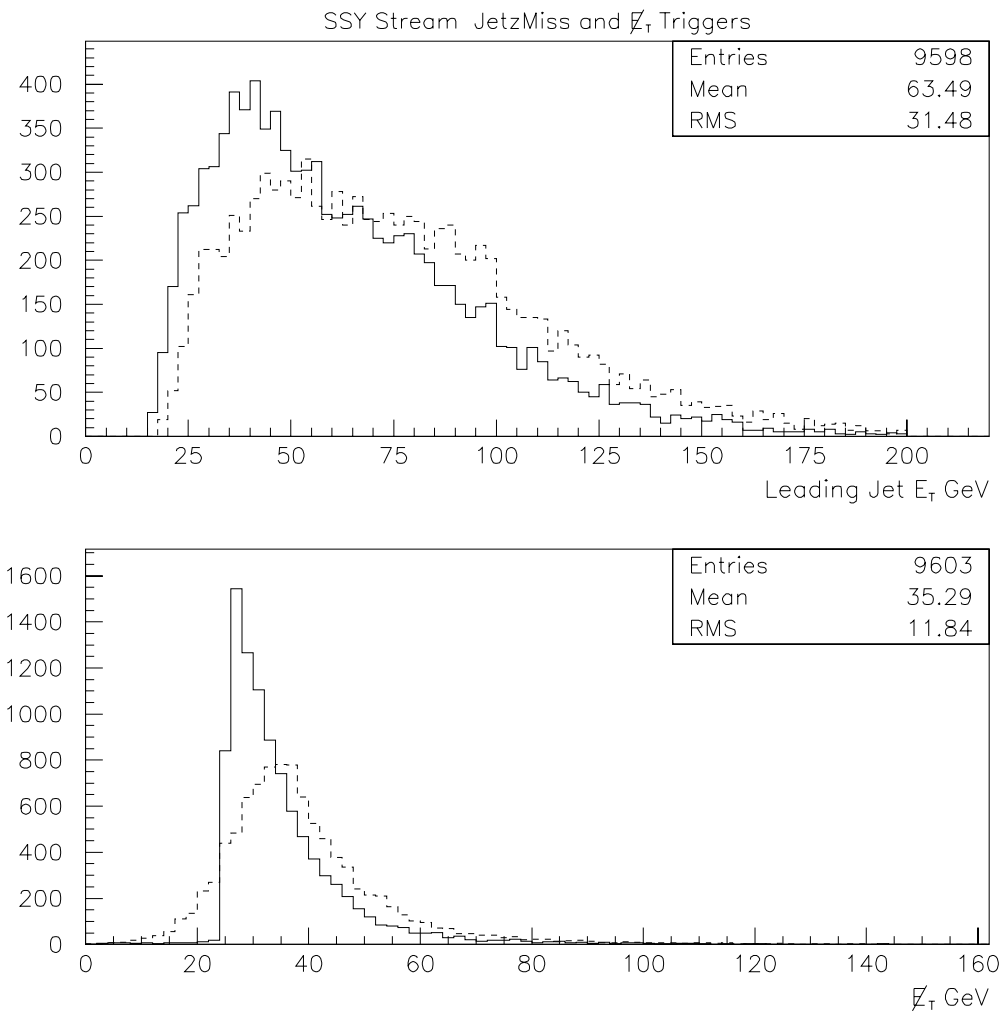


Figure 4.1: Comparison of $\not\!\!E_T$ and leading jet (highest jet $E_T$) $E_T$ before and after energy corrections after data streaming.

### 4.3.1 Electromagnetic Energy Scale

To calibrate the electromagnetic energy response in the calorimeter, the mass of the $Z$ boson was measured from its decay into electrons ($m_Z = 85$ GeV/c$^2$) and compared with the $Z$ boson mass previously well measured by other experiments ($m_Z = 91.17 \pm 0.02$ GeV/c$^2$ [60, 61]). A measurement of the $Z$ boson mass was determined by using data that required two electrons each with $E_T > 20$ GeV, some shower shape cuts, track cuts, and a fit to the dielectron transverse mass with a Breit-Wigner curve. The energy measured in the electromagnetic sections of the calorimeter was renormalized to the $Z$ boson mass.

Possible reasons for this discrepancy could be systematic shifts due to liquid argon impurity or temperature variations, test beam particle momentum (+0.5%), test beam clustering algorithms (+0.2%), zero supression (+0.5%), $\eta$-dependence, $\varphi$-cracks, sampling fractions, timing (pulsers, control signals), pulser stability and uniformity ($-0.7\%$), electronic gains ($1-2\%$), or software errors.

### 4.3.2 Hadronic Energy Scale

Since jets contain both hadronic and electromagnetic energy, a separate correction must be used to calibrate the hadronic energy scale. The missing projection fraction method was used to determine the jet energy correction [59] (first used by the CDF collaboration [62]). The technique assumes the $\not\!\!E_T$ is on average balanced (zero) for dijet and photon-jet events. The jet energy scale was determined from direct photon events with one jet by adjusting the $p_T$ balance. The jet energy correction was found to be between $5-20\%$ depending on the $E_T$ of the jet. A dijet event sample was used to determine an $\eta$-dependent correction of $0-10\%$. The overall uncertainty of the corrections was $6-12\%$.

The jet energy was calibrated with respect to the direct photon using the missing projection fraction (MPF). If $E_T^{\rm jet}$ is the uncorrected reconstructed jet $E_T$ and $E_T^{\rm corr}$

is the actual jet $E_T$, then the calorimeter response to the jet is

$$R_{\mathrm{MPF}} = \frac{E_T^{\mathrm{jet}}}{E_T^{\mathrm{corr}}}$$

$$\mathrm{MPF} = \frac{\not{E}_T \cdot \hat{n}_T^{\mathrm{jet}}}{E_T^{\mathrm{jet}}} = \frac{E_T^{\mathrm{corr}} - E_T^{\mathrm{jet}}}{E_T^{\mathrm{jet}}} = \frac{1}{R_{\mathrm{MPF}} - 1}$$

### 4.3.3 Out-of-Cone Showering

The jet fragmentation is the hadronization of partons into many low energy hadrons and is one of the least understood features of QCD. Out-of-cone showering is energy loss that results when a pion or electron, which is inside the applied cone, showers and deposits some amount of energy ouside the cone. For the DØ mixture Monte Carlo [63] (see Section 5.4.1), there were non-negligible out-of-cone losses in the forward region, although only a small effect ($< 1\%$ for $R_{\mathrm{cone}} = 0.3$) in the central region [58]. From the test beam particle library, about a $2 - 3\%$ out-of-cone loss was observed for cone sizes of $R_{\mathrm{cone}} = 0.5, 0.7$ and $3 - 5\%$ for $R_{\mathrm{cone}} = 0.3$. As observed from the mixture Monte Carlo, central jets ($|\eta| < 0.4$) with a cone size of $R_{\mathrm{cone}} = 0.5$ have a better energy response than with a cone of $R_{\mathrm{cone}} = 0.7$; the larger cone size admits more soft particles which are not part of the jet and tend to have a lower response. The percentage of energy measured inside the jet cone has been parametrized using the DØ mixture Monte Carlo. For a cone size of $R_{\mathrm{cone}} = 0.7$ and energy of 20 GeV, the percentage of jet energy retained inside the cone is 94.3%.

### 4.3.4 Zero-Suppression

In order to keep the event size small, allowing fast transfer of event data, "zero-suppression" was used in the read-out, i.e. only those data channels were read out that were significantly above the pedestal value. A gaussian width ($\sigma$) of the pedestal distribution was determined from data taken when the collider beam was off with a program called CALIB. To be read out, each channel was required to be more than twice its width ($2\sigma$) above the pedestal value.

Since the pedestal values for the DØ calorimeter cells had an asymmetric distribution, a simple suppression of channels based on a threshold of two sigma above the mean will produce a positive side tail. After zero suppression the total sum of energy is non-zero with positive offset. This effect contibuted to overmeasured jet energy.

During showering of a jet, many particles may be generated with small energies. Combined with the preamplifier response, the measured energy of the particles may fall below the zero-suppression limit. Then the spread of the jet energy over many cells will contribute for a net energy loss.

The net effect of zero-suppression is that the energy of high energy particles is underestimated while that of low energy particles is overestimated. The net energy loss due to zero suppression is determined by parameterizing the jet energy in the DØ calorimeter with collider data comparing suppressed and non-suppressed data. For a 20 GeV jet, the energy loss for a cone of $R = 0.7$ is $\sim 8\%$.

### 4.3.5 Underlying Event

The inclusion of energy in the jet which is due to particles from a beam jet must be subtracted from the jet energy to accurately determine the initial quark energy. The average underlying event energy has been determined by CDF by selecting dijet events and measuring the amount of energy seen at right angles from the jet axis. The mean value measured was 1.2 GeV/steradian and 1.85 GeV for a jet with a cone size of $R = 0.7$.

## 4.4 Missing Transverse Energy ($\not\!\!E_T$) Resolution

The $\not\!\!E_T$ (defined in Section 1.5) resolution was determined [64] by studying events from low $E_T$ jet triggers. The dominate process for the low $E_T$ jet triggers are QCD

dijet events that contain no true $\not\!\!E_T$. Events with similar transverse energies are grouped together and the $\not\!\!E_T$ is fitted to an "RMS Gaussian" distribution. The resolution was determined to be a function of scalar transverse energy

$$\sigma_T = a + bS_T + cS_T^2$$

for transverse energies of 70 GeV $\leq S_T \leq$ 330 GeV, where $a = 1.89 \pm 0.05$ GeV, $b = 6.7 \pm 0.7 \times 10^{-3}$, and $c = 9.9 \pm 2.1 \times 10^{-6}$ GeV$^{-1}$. The $\not\!\!E_T$ resolution was about $\pm 5$ GeV for scalar $E_T$ of 350 GeV.

## 4.5 Data Streaming

Data files were accessed via a CERN utility called FATMEN modified for use at DØ. A program called FATMEN coordinated a robotic library of 8 mm tapes with 16 tape drives and staging disks to provide data access over an FDDI network to the primary data analysis VAX cluster FNALDØ for physics analysis.

The Jet-Miss and $\not\!\!E_T$ triggers were used in this analysis because of the high acceptance for ISASUSY Monte Carlo events. The event criteria for these triggers are listed in Section 3.4. For the runs analyzed, the Level 2 $\not\!\!E_T$ trigger passed 143,177 events, and 227,752 events passed the Jet-Miss trigger.

Before final analysis, to avoid events with fake or mismeasured $\not\!\!E_T$, the relevant physics objects were required to be well measured in each event, including jets and $\not\!\!E_T$. The following data reduction was accomplished offline before final analysis. Events from the two online triggers were processed with reconstruction version 11.19 and filtered from the RGE stream with the following loose selections.

- Calorimeter $\not\!\!E_T > 25$ GeV.

The $\not{E}_T$ was determined by including the transverse energies measured in the calorimeter, excluding any muons that may be detected in the muon chambers. This cut reinforces the $\not{E}_T$ trigger requirement. At the time of filtering, the energy correction algorithms were not in place, thus uncorrected energies had to be used for filtering. The uncorrected energies were generally lower than corrected energies. Since muons only leave a minimum ionizing energy deposit in the calorimeter, any muon energy in the event will contribute to the missing energy of the event.

- $N_{\text{jets}} \geq 3$

  Jets were defined as energy clusters within a cone of size $R = 0.5$, within $|\eta| < 3.5$, and with uncorrected energy $E_T > 15$ GeV. Uncorrected jet energies tended to be less than corrected energies. The cone size of 0.5 was chosen to reduce noise and increase sensitivity for multijet events.

- All jets within $|\eta| < 3.5$ and $E_T > 25$ GeV must have $5\% < \text{EMF} < 90\%$, where the electromagnetic energy fraction (EMF) is the fraction of the total jet energy measured in the electromagnetic calorimeter.

  This cut served to remove events with electrons.

- $|\delta\varphi_{\text{jeti}}| > \pi/32$, where $\delta\varphi_{jeti} = \varphi_{\not{E}_T} - \varphi_{\text{jeti}}$

  By removing events where the $\not{E}_T$ in the event points directly toward a jet, events with severely mismeasured jets are rejected. Mismeasured jets would contribute to the $\not{E}_T$ signal. The $\pi/32$ fraction is the width of one cell.

- $\psi > 0.25$, where $\psi = [\varphi_{\text{jet1}}^2 + (\pi - \varphi_{\text{jet2}})^2]^{1/2}$

  This removes events where both the leading and next to leading jet were mismeasured. Jets are ordered in $E_T$ with highest being jet 1.

This left 24,843 events (from all triggers). The triggers used in this analysis are the Jet-Miss and $\not\!\!E_T$ triggers. They both require $\not\!\!E_T$ and energy deposited into the calorimeter. The trigger thresholds are shown in Tables 3.1 and 3.2. Only 9,163 events remained after requiring these triggers to be selected.

# CHAPTER 5
# DATA ANALYSIS

This analysis searched for events with high $\not\!\!E_T$, 4 or 5 jets and no electrons. Events allowed into the final data sample had jets with properties characteristic of being well measured to preserve the true $\not\!\!E_T$ signal. Likewise, the $\not\!\!E_T$ must have appeared to be from an object that escaped interaction with the calorimeter because of its weakly interacting character. From the squark-gluino data stream 9,163 events remained. Data runs with known electronics problems or data taking errors were removed from the analysis, leaving 8,666 events.

## 5.1 Multiple Interactions

The transverse energy for a cell is defined as $E_{Ti} = E_i \sin\theta_i$ where $E_i$ is the measured cell energy and $\theta_i$ is the angle between the colliding beam axis and the cell (see Section 1.5). The angle $\theta_i$ depends on the event vertex position. This dependence of the cell $E_{Ti}$ on the event vertex position adversely affects the $\not\!\!E_T$ calculation for those events that have their vertex position reconstructed incorrectly. If the event vertex is substantially mismeasured, the calculated $\not\!\!E_T$ will be mismeasured.

During the Fermilab Collider Run Ia, the average instantaneous luminosity ($8 \times 10^{30}$ sec$^{-1}$cm$^{-2}$) was sufficiently high to make the probability of a bunch crossing containing multiple soft inelastic interactions significant ($P(n_{\text{vertices}} > 1) \sim 40\%$). Although the probability that more than one hard interaction in a single bunch crossing occurs is small, the presence of even a second "soft" interaction (i.e. an interaction without high $p_T$ particles or jets) may make it impossible to determine

the correct interaction vertex. Since the calculation of $\not{E}_T$ requires knowledge of the vertex position, using the wrong vertex introduces an error in the determination of $\not{E}_T$.

The error made in the calculation of the $E_{Ti}$ (the cell $E_T$) by using the wrong vertex grows with the distance between the correct vertex and the vertex used in the $E_{Ti}$ determination. This is illustrated in Figure 5.1 which shows the effect of a mismeasured vertex on the $\not{E}_T$ resolution.

The central detector system software was optimized to determine the primary vertex position and not the number of vertices. The central detector system determines the primary event vertex (vertex position used for the $\not{E}_T$ calculation) by the number of tracks reconstructed to a vertex position and not necessarily the hard scattered interaction. The vertex resolution was determined to be $\pm 1$ cm (see Section 2.4.3), well within the necessary tolerance for the $\not{E}_T$ calculation.

To avoid events with multiple vertices, a cut on the Multiple Interaction Flag (MIF) [65] was used, which was determined using the Multiple Interaction Tool. Events were selected which are most likely to have one primary interaction using the MIF ($\leq 2$, see Figure 5.2 and Table 5.1), which combines information from the L0 trigger, central detectors, and the calorimeter. If the total energy measured in the calorimeter is greater 1800 GeV, then the MIF is set to 4. The weight $wgt1$ ($wgt2$) is the fraction of tracks used to form the primary (second) vertex. The efficiency for the MIF was determined by comparing the instantaneous luminosity of collider data collected using a minimum bias trigger (to avoid biasing the data sample with bunch crossings containing more than one interaction) with the fraction of those events identified by the MIF as having a single interaction. The MIF was found to identify single interaction events with an efficiency of $93.4 \pm 1.7\%$ with a misidentification rate of $10.0 \pm 1.6\%$ for multiple interaction events [66]. After multiple interaction events were removed, 3,347 events remained.

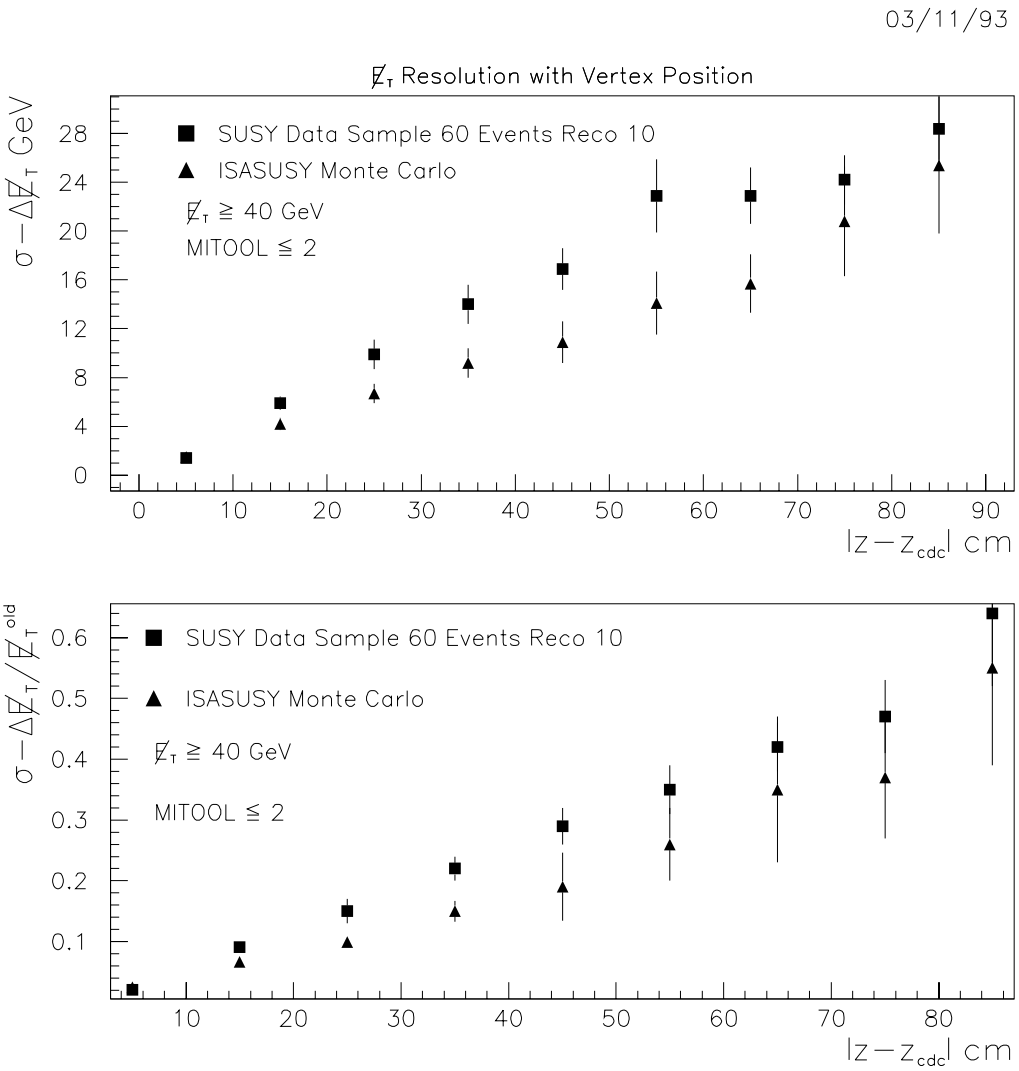


Figure 5.1: Effect of vertex mismeasurement on the $\not{E}_T$ for candidate events from collider data (60 events). Vertex position is determined primarily from the central drift chamber (CDC). The vertex position was varied from the measured CDC position $z_{\mathbf{cdc}}$ and the $\not{E}_T$ was recalculated. The top figure shows the average difference in $\not{E}_T$ before and after changing the vertex ($\sigma - \delta\not{E}_T$) versus the difference in the adjusted and CDC vertex position. The top figure show the average fractional difference in $\not{E}_T$ after changing the vertex ($\sigma - \delta\not{E}_T/\not{E}_T{}^{\mathrm{old}}$). For a large difference in the vertex where the $\not{E}_T$ is reconstructed ($\sim 20$ cm), the recalculated $\not{E}_T$ may vary as much as the uncertainty of the $\not{E}_T$ due to the calorimeter energy resolution.

Table 5.1: Results from the Multiple Interaction Flag (MIF). The flag is one or two for an event that probably has a single interaction. three or four for a multiple interaction, and zero if there is not enough information.

| Central Tracking | L0 | MIF | |
|---|---|---|---|
| 1 vertex | bad | 2 | |
| | 1 | 1 | |
| | 2 | 2 | |
| | 3 | 3 | |
| | 4 | 3 | |
| | 4 | 3 | vertex found from CDC |
| | 4 | 4 | vertex found from FDC |
| 2 vertices | bad | 3 | |
| | 1 | 2 | $\lvert z_{\mathrm{CDC}} - z_{\mathrm{L0}} \rvert < 8$ cm |
| | 1 | 3 | $\lvert z_{\mathrm{CDC}} - z_{\mathrm{L0}} \rvert \geq 8$ cm |
| | 2 | 2 | $\lvert z_{\mathrm{CDC}} - z_{\mathrm{L0}} \rvert < 8$ cm and $wgt1 \leq 0.7$ |
| | 2 | 4 | $\lvert z_{\mathrm{CDC}} - z_{\mathrm{L0}} \rvert \geq 8$ cm |
| | | | and $(wgt1 - wgt2)/wgt1 < 25$ |
| | 2 | 3 | otherwise |
| | 3 | 3 | |
| | 4 | 4 | |
| 3 vertices | bad | 4 | |
| | 1 | 2 | $\lvert z_{\mathrm{CDC}} - z_{\mathrm{L0}} \rvert < 8$ cm |
| | 1 | 3 | $\lvert z_{\mathrm{CDC}} - z_{\mathrm{L0}} \rvert \geq 8$ cm |
| | 2 | 2 | $\lvert z_{\mathrm{CDC}} - z_{\mathrm{L0}} \rvert < 8$ cm and $wgt1 \leq 0.7$ |
| | 2 | 3 | otherwise |
| | 3 | 4 | |
| | 4 | 4 | |

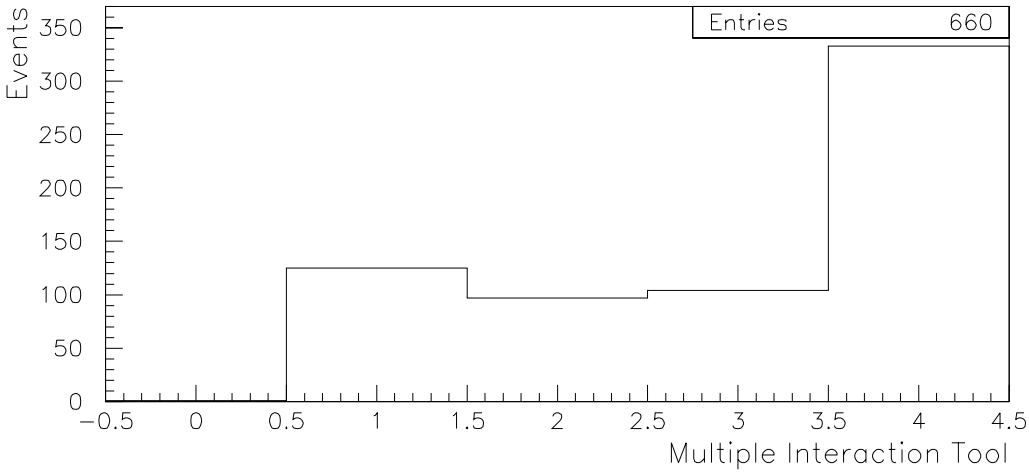


Figure 5.2: Multiple Interaction Flag distribution before the final $\not\!\!E_T$ cut. A value of one or two is considered to be a single interaction.

## 5.2 Jets

Jet energies must be well measured in each event to reduce the uncertainty in the $\not\!\!E_T$. A fake jet is any reconstructed jet object which was a result of something other than particles from a proton-antiproton collision. This may be the result of a noisy electronics channel, a change in pedestal values, hardware problems affecting a group of channels systematically, losses of Main Ring protons, cosmic ray bremsstrahlung, or beam-gas interactions.

The following jet cuts, Leading Cell Fraction, Electromagnetic Fraction, and Hadronic Fraction, are standard analysis criteria for DØ jet studies and were about 95% efficient [67], depending on jet $E_T$. Only those jets with corrected energy $E_T > 20$ GeV and $|\eta| < 3.5$ were considered.

### 5.2.1 Leading Cell Fraction

Cells isolated in energy, where there is a large energy difference between neighboring cells in a jet, may be due to a calorimeter discharge, electronic failure, or

other noise. The leading cell ratio ($\frac{E_2}{E_1}$, where $E_1$ is the leading cell in energy and $E_2$ is the next leading cell in energy) was designed to remove events containing a jet which has most of its energy concentrated in one cell. This ratio would be zero for a single cell and almost 1 for a jet whose energy is spread among many cells. A cut of $> 10\%$ was used and has been found to reject 90% of the noise jets due to calorimeter discharges [67]. Cells isolated in space, where there are no nearby cells with significant energy, are removed beforehand in the reconstruction program. This selection leaves 3,023 events.

### 5.2.2 Main Ring Interactions

The Main Ring runs through the DØ detector directly above the Tevatron ring and was used to accumulate anti-protons for collisions. Beam losses in the Main Ring, in particular during injection and transition, can lead to large energy deposits in the calorimeter cells nearest to the Main Ring, thus causing preamplifiers especially in the coarse hadronic section to saturate. The sampling of the BLS (baseline subtraction) circuits before the crossing sets the baseline incorrectly so that any events recorded during that crossing may have negative coarse hadronic energies. The central detectors were adequately shielded from Main Ring losses by the uranium surrounding them. The DØ calorimeter shows Main Ring events by the energy deposited into the coarse hadronic modules adjacent to the Main Ring resulting in the reconstruction of jets with a large hadronic fraction and large $\not\!\!E_T$ opposite the Main Ring.

At the trigger level, Main Ring events were avoided by requiring the trigger tool MICROBLANK to be set [68]. This vetoed Main Ring events within a window of $\pm 800$ nsec. Since the calorimeter electronic sampling was $\sim 2$ $\mu$sec, the MICROBLANK veto was not fully efficient for vetoing events with Main Ring energy deposited into the calorimeter. The typical deadtime due to the MICROBLANK veto was $\sim 9\%$. The MICROBLANK veto used accelerator timing signals only,

making no effort to minimize the deadtime (such as when Main Ring losses were negligible), although the veto efficiency was completely determined.

The coarse hadronic fraction ($E_{\rm CH}/E_{\rm total}$) of the jets was used to eliminate the remaining Main Ring events, since Main Ring losses were almost entirely contained in the coarse hadronic layers. If this fraction was $> 40\%$ for any jet, the event was removed. This left 2,845 events in the data sample.

### 5.2.3 Electromagnetic Fraction

Events with spurious calorimeter signals due to low rate calorimeter discharges, as well as events with electrons were removed by an electromagnetic fraction requirement for each jet. The electromagnetic fraction of a jet is the fraction of the total jet energy contained in the electromagnetic calorimeter ($E_{\rm EM}/E_{\rm total}$). Jets usually do not have a fraction close to zero or one. An EM fraction cut of $> 5\%$ rejects 95% of the noise jets [67] and a cut of $< 90\%$ rejects 95% of the Monte Carlo $W$ boson decay to electron events. After the electromagnetic fraction cut, 2,829 events remain.

### 5.2.4 ICD Faction

If particles produced in a $p\overline{p}$ collision enter the region between the central and end calorimeters, the energies of these particles may be deposited into the stainless steel wall of the cryostat and not be measured by the calorimeter or the ICD. Although the ICD will measure the energy of particles in this region, its energy resolution is less than that of the DØ calorimeter. This will adversely affect the $\not\!\!E_T$ resolution.

If a jet is directed into this region, it faces a greater chance of energy mismeasurement and will contribute to the $\not\!\!E_T$. To remove the influence of these events, a cut on the fraction of total energy deposited into the ICD region was used $E_{\rm ICD}/E_{\rm total} > 50\%$. For data taken with the Jet-Min trigger (no $\not\!\!E_T$ requirement), this cut was $\sim 99\%$ efficient.

This cut was not used in the final analysis, although it was necessary when the $\not{E}_T$ threshold was lower ($< 60$ GeV).

### 5.2.5 Number of Cells in the Jet

A jet that has been reconstructed containing only one cell may be the result of an eroneous energy measurement. The hot cell suppression programs (see Section 4.1) would most likely remove the influence of such events. For a low $\not{E}_T$ cut ($< 60$ GeV), an unusually large number of events containing a jet with only one cell with $E_T > 1$ GeV was observed

This cut was not used in the final analysis, but events were removed for $\not{E}_T < 60$ GeV containing a jet with only one cell with $E_T > 1$ GeV.

## 5.3 Signal Selection: Missing Transverse Energy ($\not{E}_T$) and Number of Jets

The $\not{E}_T$ signature is the most distinguishing feature of supersymmetric particles. Events with high $\not{E}_T$ are selected to remove the backgrounds and retain what could be candidate events. Thus it is important to ensure that the $\not{E}_T$ is really due to the transverse energy carried away by a weakly interacting particle and not an artifact of detector effects as, e.g., mismeasurement of jet energy due to cracks in the calorimeter or jet energy fluctuations.

Events were discarded in which the $\not{E}_T$ vector is parallel to the transverse momentum vector of a jet (see Section 4.5 ). All jets with $E_T > 20$ GeV and $|\eta| < 3.5$ were required to pass this cut. Also, only those events whose two leading jets (highest in $E_T$) satisfy

$$\psi > 0.5$$

were accepted (see Section 4.5). These cuts are shown in Figure 5.3, where the events within the arc in the upper left corner are removed.

Each event was required to contain at least four jets, each with $E_T > 20$ GeV (see Figure 5.4). This left 223 events.

Missing transverse energy is the single most powerful variable for distinction between signal and background. Each event must have high $\not\!\!E_T$, as is characteristic of the LSP signature.

Muons interact in the calorimeter by depositing only minimum ionizing energy. The $\not\!\!E_T$ used in this analysis did not include any $E_T$ from the muons, only the transverse energies measured in the calorimeter. No muons with $E_T > 5$ GeV (determined from the the muon chambers) were in the data sample after all analysis cuts were applied. Therefore, any muons that were not detected contribute to the $\not\!\!E_T$.

The $\not\!\!E_T$ and jet energies were corrected offline, after the initial streaming filter. Some events which did not pass the filter requirements may have uncorrected jet energies below the initial threshold and corrected energies above the final threshold. The latter cut must be high enough to avoid these events. A $\not\!\!E_T$ cut of 50 GeV was found to be sufficient. Figure 5.8 shows the collider data compared with the QCD, $W$ and $Z$ boson backgrounds for changes in the $\not\!\!E_T$ cut from 30 GeV to 100 GeV.

The $\not\!\!E_T$ cut was varied from 50 GeV to 100 GeV, see Figure 6.5. A minimum requirement of $\not\!\!E_T > 65$ GeV was found to support the best lower limit on the gluino mass for a squark mass of 500 GeV/c$^2$ (see Section 6.3). This left 5 events in the final data sample. All data cuts are listed in Table 5.2.

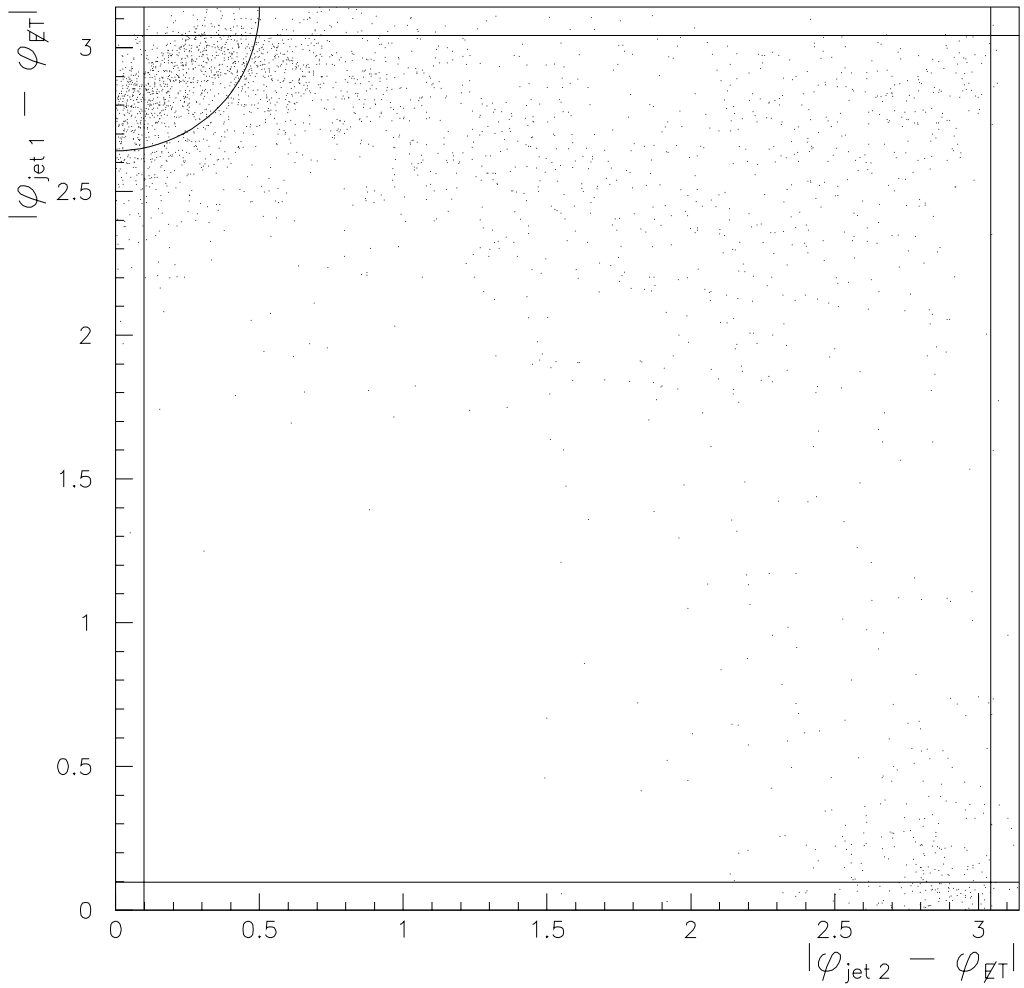


Figure 5.3: Collider data (8,666 events) that passed the $\not{E}_T$ triggers. The angle between the $\not{E}_T$ and jet$-i$ in the plane transverse to the beam is $\delta\varphi_{\text{jet}i}$. Shown is the $\delta\varphi_{\text{jet1}}$ of leading jet vs. $\delta\varphi_{\text{jet2}}$ of next-to-leading jet.

The lines shown parallel to the coordinate axes demonstrate the cut that removes events where the $\varphi_{\not{E}_T}$ is near the $\varphi_{\text{jet}}$ where the $\not{E}_T$ originated from events with mismeasured jet energies.

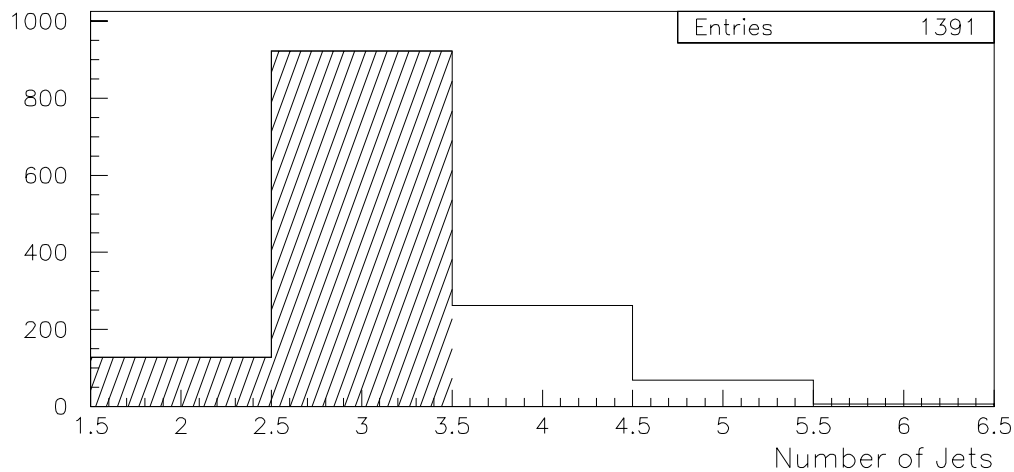


Figure 5.4: Jet multiplicity for collider data after all cuts (excluding the $\not\!\!E_T$ cut). The shaded region indicates the events that were removed.

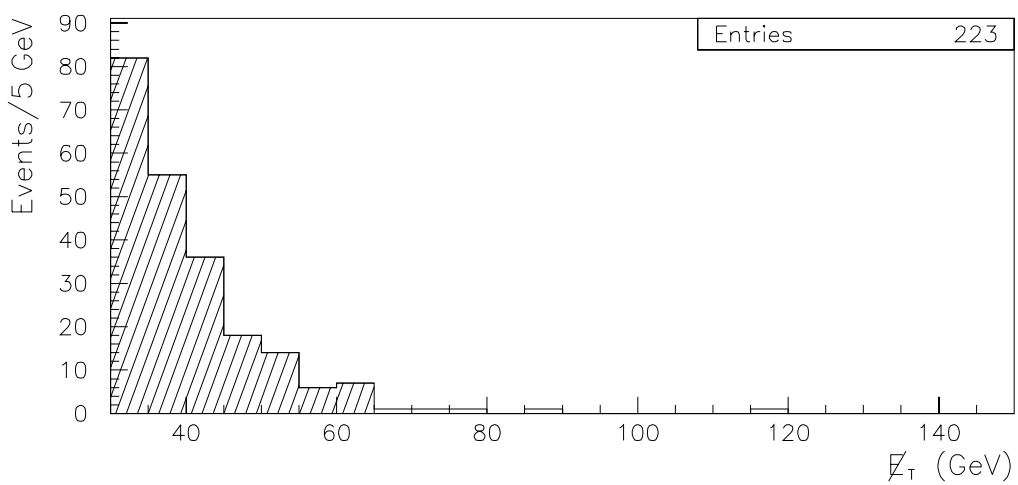


Figure 5.5: $\not\!\!E_T$ distribution from data after all analysis cuts, $\not\!\!E_T > 30$ GeV. The shaded region indicates the events that were removed.

Table 5.2: Offline analysis selection.

| Selection | Collider Data |
|---|---|
| New Phenomena Filtering (see Section 4.5) | 24,843 |
| Jet-Miss or $\not\!\!E_T$ Trigger (see Tables 3.2 and 3.1) | 9,163 |
| Remove unusable runs | 8,666 |
| Remove events with multiple interactions | 3,347 |
| All jets: $R = 0.5$, $\|\eta\| < 3.5$ and $E_T > 20$ | |
| Leading Cell Fraction $> 10\%$ | 3,023 |
| Coarse Hadronic Fraction $< 40\%$ | 2,845 |
| $5\% <$ Electromagnetic Fraction $< 90\%$ | 2,829 |
| $\frac{\pi}{32} < \|\varphi_i\| < \frac{31\pi}{32}$,where $\varphi_i = \varphi_{\not\!\!E_T} - \varphi_{\mathrm{jet-i}}$ | 1,942 |
| $\psi > 0.5$, where $\psi = [\varphi_1^2 + (\pi - \varphi_2)^2]^{1/2}$ | 1,392 |
| Number of Jets $\geq 4$ | 223 |
| $\not\!\!E_T > 65$ GeV | 5 |

## 5.4 Background Calculations

Physics backgrounds to a multijet and $\not\!\!E_T$ analysis include processes with neutrinos, muons and electrons such as $W$ and $Z$ boson decays. Detector backgrounds can be from QCD multijet events, where some events with hard scattered partons may have enough $\not\!\!E_T$ introduced by calorimeter energy mismeasurement to enter the final data sample. The backgrounds for the supersymmetry signal of 4 or 5 jets and high $\not\!\!E_T$ were $W$ and $Z$ boson decays into neutrinos and multijet QCD events where the jets were significantly mismeasured.

A muon leaves only a minimum ionizing particle trace in the calorimeter. Since the $\not{E}_T$ was determined from calorimeter cells, muons will contribute to the $\not{E}_T$ of the event and must be considered as a background.

The electromagnetic fraction cut was expected to eliminate most events with electrons, although not every electron will deposit its energy into the electromagnetic calorimeter. These events will be in the final data sample when the electron energy is directed into an uninstrumented section of the detector. Some highly energetic electrons may "punch through" to the hadronic sections of the calorimeter; or similarly, the hadronic section behind the electron may be noisy and contribute substantially to the hadronic energy fraction of the so–called jet. The cross section of backgrounds with electrons (high $E_T$) is small and combined with the probability of punchthrough renders this background negligible.

### 5.4.1 DØ Detector Simulation

The DØ collaboration uses a detector simulation program based on the GEANT [69, 70] package provided by CERN to simulate the detector's response to particles. Multiple coulomb scattering, full showering of electromagnetic and hadronic particles, and bremsstrahlung by electrons and muons were included. Tracking chamber volume materials were included fully down to the sense wires. The full support structure for the DØ calorimeters was included, although the uranium plate and liquid argon construction of the calorimeter were simulated by a mixture of effective atomic weight. Sampling fluctuations were included along with the difference in hadronic and electromagnetic response in shower developement as determined by testbeam results. Tracking was done for particles down to an energy of 200 MeV. The cell readout structure was included and a rough conversion to ADC counts was included to allow the user to add noise and simulations of the online trigger. Simulated Level 1 trigger and the actual Level 2 filter scripts and configuration files were available to simulate the online triggers on Monte Carlo data.

The long processing time required for a full simulation of the detector motivated the production of the shower library [71, 63]. A library of single particle showers generated by the full simulation of the calorimeter was produced. Accessing this library of information instead of individually showering each particle improves CPU speed per event by as much as a factor of 300.

Such a library cannot contain every possible shower; the available phase space must be quantized. Vertex, eta, phi position, and momentum were all separated into bins for each particle type. The shower library only stores calorimeter response and no central detector information, although the central detector material was included during generation. Building the calorimeter response in the shower library was accomplished by using the DØGEANT 3.14 calorimeter module mixture Monte Carlo with fully simulated electromagnetic showers and parametrized hadronic showers as input.

Monte Carlo events were generated using the shower library to simulate detector response and trigger simulations were also included. The same reconstruction algorithms were used on Monte Carlo as were used for collider data.

## 5.5 Vector Boson Backgrounds

Any event whose final decay products include an energetic neutrino may exhibit large missing transverse energy and is potentially a background to this search. Intermediate vector bosons are produced in the high energy collisions at Fermilab and can decay into leptons, jets, and neutrinos. These events are produced via the weak interaction and have a small cross section relative to the strong interaction from QCD.

To estimate the $W$ and $Z$ boson backgrounds, the VECBOS [72] Monte Carlo program was used to calculate the parton 4-vectors and cross sections. Another Monte Carlo program, ISAJET [29], fragmented the partons into jets producing input for the detector simulation. The samples generated with VECBOS included $W \rightarrow e\nu$ + 4-jets, $W \rightarrow \mu\nu$ + 4-jets, $W \rightarrow \tau\nu$ + 3-jets, $Z \rightarrow \mu\bar{\mu}$ + 3-jets, and $Z \rightarrow \nu\bar{\nu}$ + 3-jets.

Table 5.3 lists the background contributions after all cuts were applied. After event, detector and trigger simulation the total background from $W$ and $Z$ boson events was $5.2 \pm 2.2$ events. Figure 5.6 shows the $\not{E}_T$ distribution for the collider data compared with the $W$ and $Z$ boson Monte Carlo background.

## 5.6 QCD Background

Another significant Standard Model background because of its large cross section can be hard scattered partons that radiate gluons, resulting in a final event signature of multi-jets. An event may appear to have large $\not{E}_T$ if the jet energies were significantly mismeasured.

Table 5.3: List of $W$ and $Z$ boson backgrounds estimated after all analysis cuts with VECBOS Monte Carlo and DØGeant detector simulation.

| Background | $\sigma$ (pb) | BF (%) | $\epsilon$ (%) | $\epsilon \cdot \mathrm{BF} \cdot \sigma \cdot \mathcal{L}$ (events) |
|---|---|---|---|---|
| $W \to e\nu$ | $146 \pm 58$ | $10.5 \pm 0.9$ | $1.33 \pm 0.14^{+0.27}_{-0.37}$ | $1.5 \pm 0.7$ |
| $W \to \mu\nu$ | $146 \pm 58$ | $10.5 \pm 0.9$ | $1.48 \pm 0.12^{+0.38}_{-0.20}$ | $1.8 \pm 0.9$ |
| $W \to \tau\nu$ | $516 \pm 155$ | $6.8 \pm 1.0$ | $0.290 \pm 0.096^{+0.16}_{-0.00}$ | $0.9 \pm 0.5$ |
| $Z \to \nu\bar{\nu}$ | $148 \pm 44$ | $20.3 \pm 0.4$ | $0.43 \pm 0.14^{+0.047}_{-0.095}$ | $0.9 \pm 0.4$ |
| $Z \to \mu\bar{\mu}$ | $148 \pm 44$ | $3.34 \pm 0.04$ | $0.43 \pm 0.14^{+0.00}_{-0.095}$ | $0.14 \pm 0.07$ |
| Total Events | | | | $5.2 \pm 2.2$ |

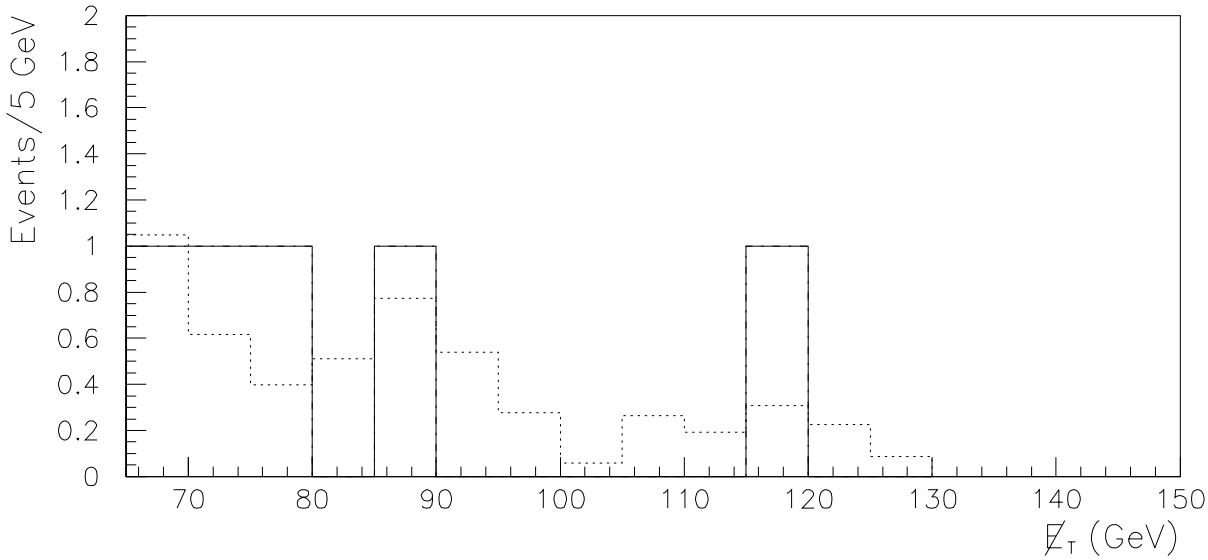


Figure 5.6: Comparison of $\not{E}_T$ distributions of collider data (solid line) with that expected from events with $W$ and $Z$ bosons (dotted line).

### 5.6.1 Estimate from Collider Data

This background was estimated using events from a trigger with no $\not\!\!E_T$ requirement. A jet trigger with a hardware requirement of one jet tower with $E_T > 3$ GeV and a software requirement of one jet with a cone size of $R = 0.7$ and $E_T > 20$ GeV was used. The small amount of data collected with this trigger leads to a large uncertainty in the final estimate.

The same analysis selection was applied to this data sample (no $\not\!\!E_T$ cut), with 63 events remaining, see Figure 5.7. To estimate the contribution of such events to the SUSY sample, an extrapolation in $\not\!\!E_T$ was necessary. To do this extrapolation, a parametrization of the $\not\!\!E_T$ distribution was determined from a fit to the data.

In the absence of any theoretical guideline for the function, various functions were tried. The best fit was found to be with a function of the form

$$N_{QCD} = e^{A+B\sqrt{\not\!\!E_T}}$$

shown in Figure 5.7. The total number of background events estimated from an extrapolation of data is $1.54 \pm 0.88$ (stat) events.

Figure 5.8 shows the $\not\!\!E_T$ distribution for the collider data and the Standard Model backgrounds. The combined vector boson backgrounds and QCD backgrounds appear to accurately account for the events with $\not\!\!E_T > 45$ GeV. Below 45 GeV, the QCD background calculation fails to reproduce the data because no trigger estimate has been used (the $\not\!\!E_T$ trigger threshold was set at 35 GeV for most of the data collection). Furthermore, the lack of statistics does not allow for proper evaluation of the functional fit to the QCD $\not\!\!E_T$ background.

### 5.6.2 Estimate from Monte Carlo with Jet $E_T$ Smearing

If the QCD background originates from mismeasured jets, then perhaps an estimate can be found by applying the DØ jet energy resolution to ISAJET Monte Carlo. ISAJET was used to generate 2-jet events in various $p_T$ ranges, where gluon

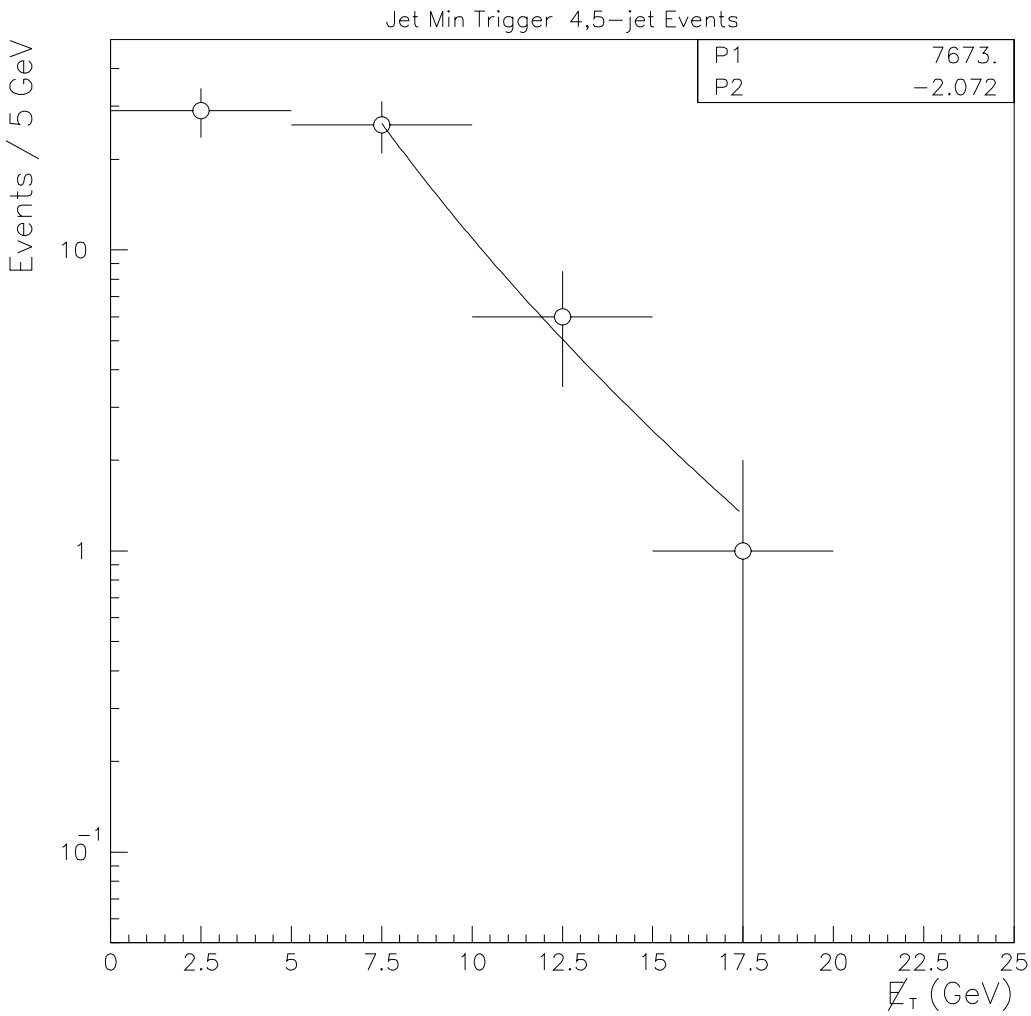


Figure 5.7: The $\not\!\!E_T$ distribution for events with at least one jet of $E_T > 20$ GeV. Also shown is a fit of this distribution to a function of the form $N_{QCD} = e^{P1+P2\sqrt{\not\!\!E_T}}$.

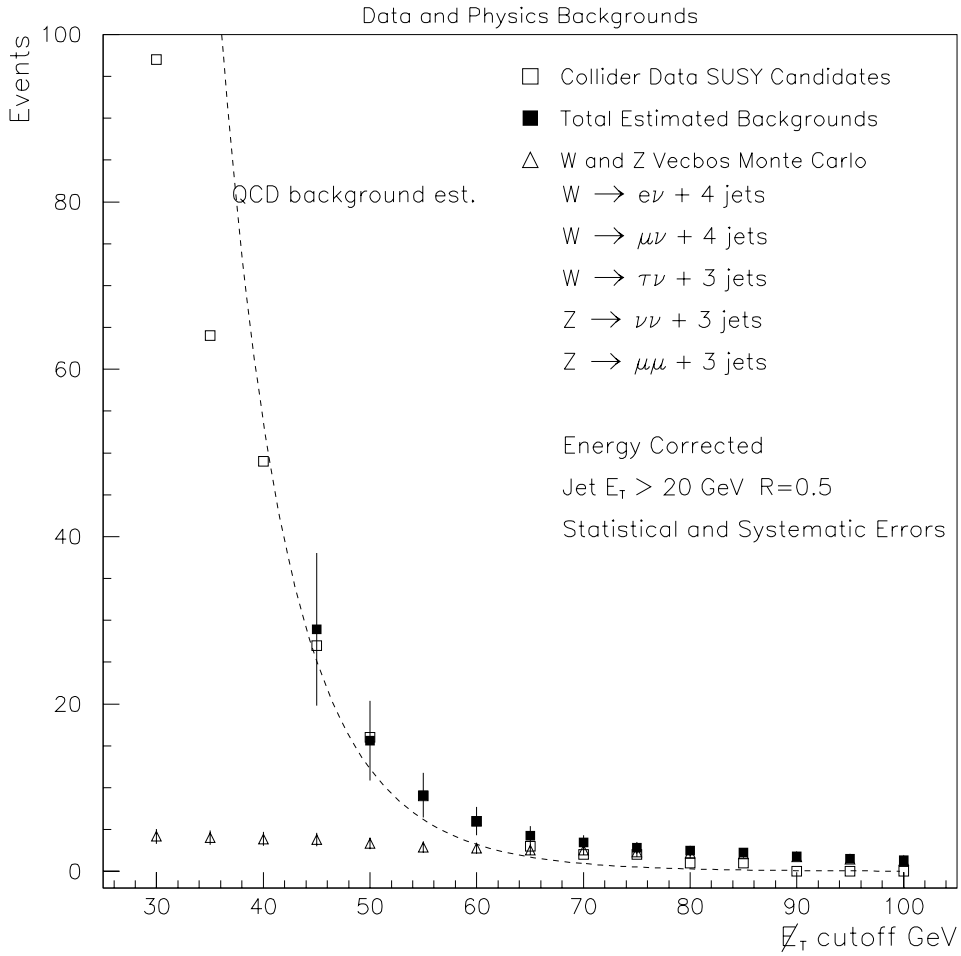


Figure 5.8: Number of events versus $\not{E}_T$ cut with additional cuts on the ICD fraction and number of cells in the jet for: collider data (SUSY selection, open squares), $W$ and $Z$ boson Monte Carlo events (open triangles), and the total background ($W/Z$ and QCD, filled squares).

Table 5.4: Parameters for the DØ jet energy resolution function. applied to ISAJET four-jet events.

| | Noise | Sample | Constant |
|---|---|---|---|
| $\|\eta\| < 0.8$ | 1.74 | 0.86 | 0.016 |
| $0.8 < \|\eta\| < 1.5$ | 7.81 | 0.346 | 0.117 |
| $1.5 < \|\eta\|$ | 1.97 | 1.10 | 0.034 |

fragmentation may create additional jets in the event. A large number of events were required from ISAJET so that a statistically significant number will pass the $\not\!\!E_T$ cut after energy smearing. Therefore, the DØ detector simulator, DØGEANT cannot be used due to its slow speed. Instead, each jet energy was smeared according to the parametrized DØ jet energy resolution function [73] determined from collider data. Events were selected with four or more jets (cone size of 0.5 and with $|\eta| < 3.5$), and the minimum jet energy before smearing was 15 GeV to allow for smearing upwards in energy. The jet energy resolution used was

$$\frac{\sigma}{E} = \frac{A_{\text{Noise}}}{E} \oplus \frac{B_{\text{sample}}}{\sqrt{E}} \oplus C$$

where the constants were separated into eta regions, see Table 5.4.

For each jet, the smeared jet energy contributes to the $\not\!\!E_T$.

$$\not\!\!E_x = -\sum_i^{\text{jets}} \cos\varphi_i \cdot \delta E_{Ti}$$

where $\varphi_i = \varphi$ of jet i; $\delta E_T = E_T^{\text{smeared}} - E_T^{\text{unsmeared}}$.

The angular cuts, $\delta\varphi$ and $\psi$, were applied, as well as the jet multiplicity cut $N_{\text{jets}} = 4, 5$. The final $\not\!\!E_T$ distribution, shown in Figure 5.9, was used to estimate the QCD background. The jet efficiency was estimated to be 92% per jet, and the trigger efficiency applied was 92%. The number of background events expected for this estimate was $49 \pm 8$ (stat) events.

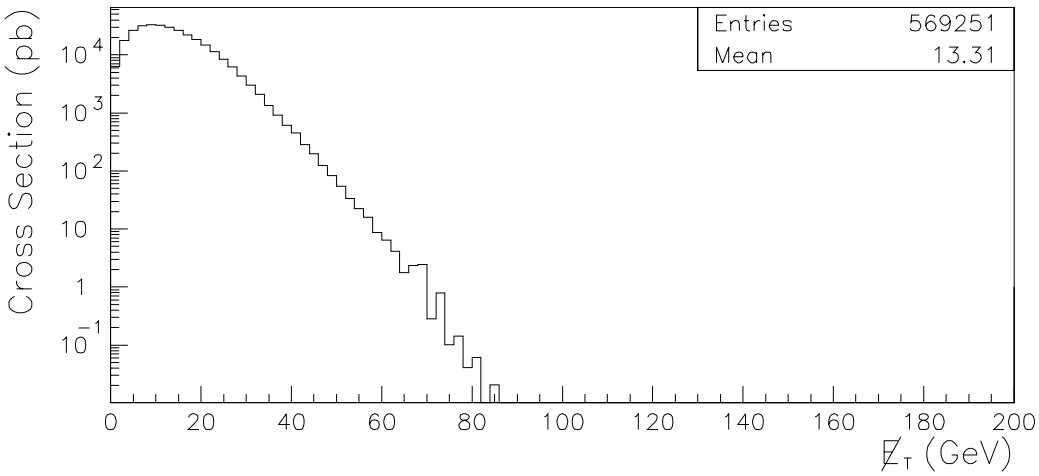


Figure 5.9: Distribution of $\not{E}_T$ for ISAJET four jet events, where the jets were smeared according to the DØ jet resolution.

Because of the large systematic uncertainty in the estimate of the QCD background, this contribution to the background was not included in the final background estimate used to establish the lower mass limit (see Chapter 6). Most high $\not{E}_T$ events from the QCD background result from a large fluctuation in the energy measurement of the primary jet, and smaller contributions from the less energetic jets mismeasured in nearly the same $\varphi$ direction. A large fluctuation in measured energy probes the tail of the jet energy resolution parametrization. This analysis is very sensitive to the parametrization of the tail of the jet energy resolution. Therefore, this is not a very good method for determining the QCD background contribution and it is not included in the final background estimate for determining the mass limit.

Table 5.5: Supersymmetry model parameters used for the ISAJET Monte Carlo in signal cross section caculations.

| Parameter | Value Used |
|---|---|
| $\tan\beta$ | 2 |
| $\mu$ | $-250$ GeV |
| $m_{\mathrm{top}}$ | 140 GeV/c$^2$ |
| $m_{\mathrm{H}^+}$ | 500 GeV/c$^2$ |

## 5.7 Squark-Gluino Efficiencies

The Monte Carlo program ISASUSY [74] was used to simulate the production of gluino-gluino, squark-squark, and squark-gluino events in proton-antiproton collisions at the Fermilab Tevatron. The shower library provided detector response and trigger simulations were included as well. The ISASUSY data points were chosen to match the experiment's sensitivity range and to be complementary to the LEP bounds for $\tan\beta$ and $\mu$ (see Section 1.3.3). The model parameters used in this analysis are listed in Table 5.5.

The same cuts as applied to the collider data were applied to the signal Monte Carlo sample. The summary of the generated signal Monte Carlo samples in Table 5.6 gives for every sample the gluino and squark mass, the total cross section and the signal detection efficiency.

There are two $m_{\tilde{g}}$ and $m_{\tilde{q}}$ combinations of particular interest. For squarks much heavier than gluinos, the supersymmetry signal comes mostly from the production of gluinos whose production cross section and decays do not vary significantly with higher squark masses. Then the mass limit on the gluino doesn't change for heavier squarks reaching an asymtopic value.

The other important combination occurs when the squark and gluino masses are equal. The signal cross section will be maximum at this point since the squark and gluinos can be equally produced. To interpolate the efficiencies for the mass limit, the efficiencies for these two cases were parametrized to linear functions of the mass in order to produce the DØ cross section limit and derive the mass limits. Figures 5.10 and 5.11 show the efficiencies and their respective parametrizations.

## 5.8 Systematic Uncertainties

An uncertainty that can influence all measurements of a particular quantity equally is called a systematic uncertainty. This section describes the systematic uncertainties affecting this analysis, see Table 5.7. The systematic uncertainties were included in the final limit calculation by combining them in quadrature with the statistical errors whose sources were binomial errors from the counting of events passing kinematic cuts. The uncertainties in the backgrounds and signal estimates were assumed to be random (normally distributed) and independent.

There is a systematic error due to the energy scale uncertainty. The jet energy scale uncertainty was about 10% as described by the jet energy correction working group [75]. For the Monte Carlo backgrounds, the jet $E_T$ threshold was varied by 10% and the resulting change in the number of background events was recorded as the systematic error. A shift in the energy scale for an event will also systematically change the missing transverse energy for that event. The missing transverse energy was varied as well to estimate this uncertainty, and this effect has also been included in the reported systematic uncertainty for the background efficiencies.

There was a systematic uncertainty in the VECBOS cross section of 10% per jet, and for the 4-jet sample the total systematic uncertainty was 20%. DØ finds

Table 5.6: Detection efficiencies from ISASUSY Monte Carlo are shown with statistical errors. The gluino and squark masses are in units of GeV/c$^2$.

| $m_{\tilde{g}}$ | $m_{\tilde{q}}$ | $\sigma$ (pb) | $\epsilon$ (%) | $m_{\tilde{g}}$ | $m_{\tilde{q}}$ | $\sigma$ (pb) | $\epsilon$ (%) |
|---|---|---|---|---|---|---|---|
| 100 | 150 | 537. | $1.24 \pm 0.38$ | 200 | 220 | 12.9 | $12.21 \pm 1.62$ |
| 200 | 150 | 60.7 | $6.86 \pm 0.85$ | 220 | 220 | 9.35 | $6.62 \pm 1.20$ |
| 300 | 150 | 35.3 | $4.95 \pm 0.73$ | 400 | 100 | 154. | $0.82 \pm 0.50$ |
| 150 | 100 | 511. | $2.57 \pm 0.53$ | 220 | 200 | 15.4 | $7.30 \pm 1.27$ |
| 150 | 200 | 52.8 | $6.11 \pm 0.81$ | 400 | 200 | 5.97 | $9.70 \pm 1.01$ |
| 150 | 300 | 27.5 | $5.59 \pm 0.77$ | 400 | 250 | 1.44 | $12.09 \pm 1.13$ |
| 150 | 400 | 26.0 | $3.42 \pm 0.61$ | 275 | 275 | 1.44 | $12.97 \pm 1.17$ |
| 100 | 100 | 1411. | $1.15 \pm 0.37$ | 225 | 300 | 2.18 | $15.11 \pm 1.27$ |
| 100 | 500 | 346. | $0.93 \pm 0.34$ | 200 | 400 | 3.49 | $11.05 \pm 1.08$ |
| 500 | 100 | 132. | $0.41 \pm 0.25$ | 175 | 175 | 47.3 | $5.70 \pm 0.78$ |
| 200 | 200 | 19.4 | $7.26 \pm 0.88$ | 125 | 250 | 92.4 | $3.13 \pm 0.58$ |
| 150 | 500 | 29.6 | $4.55 \pm 1.02$ | 125 | 300 | 83.1 | $2.16 \pm 0.49$ |
| 175 | 300 | 10.4 | $8.13 \pm 1.33$ | 125 | 400 | 90.2 | $2.17 \pm 0.49$ |
| 175 | 500 | 10.4 | $8.07 \pm 1.33$ | 250 | 125 | 94.6 | $3.09 \pm 0.58$ |
| 300 | 200 | 8.43 | $9.74 \pm 1.45$ | 300 | 125 | 75.2 | $1.92 \pm 0.47$ |
| 225 | 500 | 1.61 | $10.80 \pm 1.52$ | 350 | 100 | 169. | $1.34 \pm 0.40$ |
| 400 | 150 | 25.2 | $2.93 \pm 0.83$ | 375 | 100 | 162. | $1.55 \pm 0.42$ |
| 250 | 250 | 3.34 | $9.97 \pm 1.46$ | 350 | 125 | 63.8 | $2.78 \pm 0.55$ |

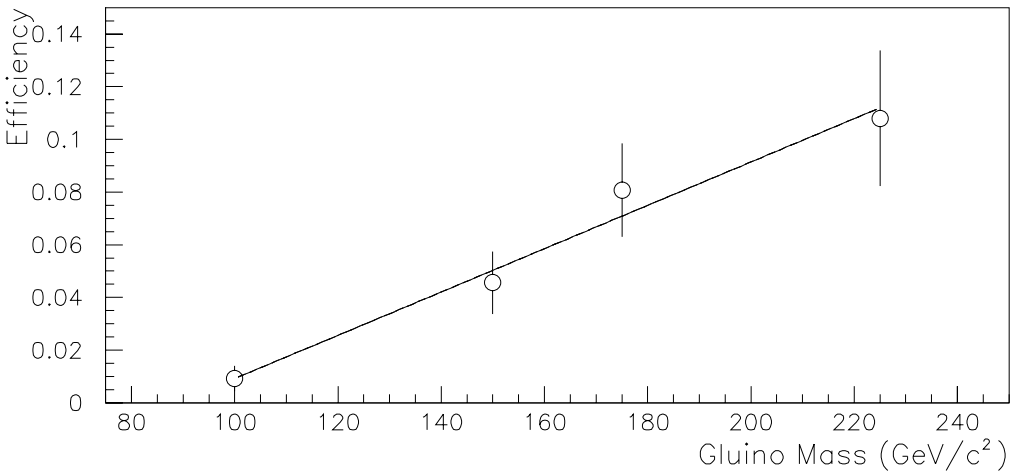


Figure 5.10: Plot of efficiency vs. gluino mass for a squark mass of 500 GeV/c$^2$, with a linear fit. The errors are combined statistical and systematic uncertainties.

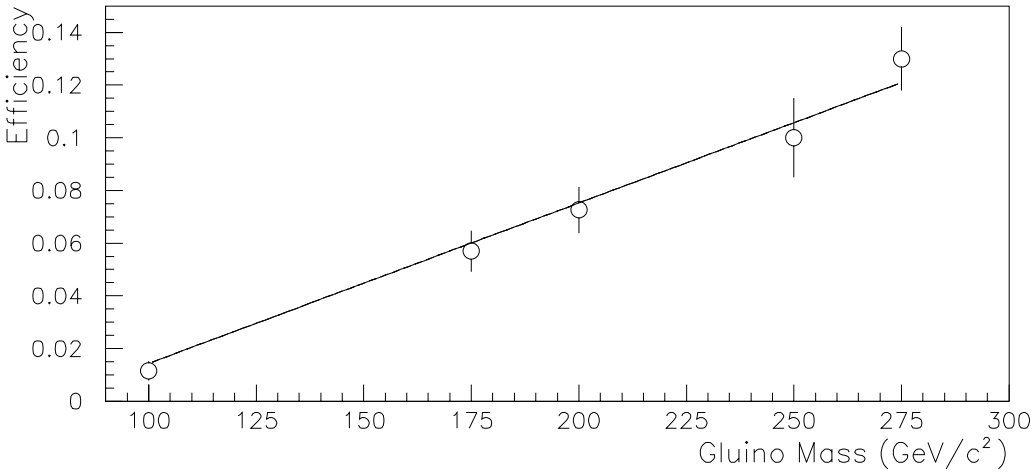


Figure 5.11: Plot of efficiency vs. Gluino mass for equal squark masses, with a linear fit. The errors are combined statistical and systematic uncertainties.

Table 5.7: Estimated systematic uncertainties included in the cross section limit.

| Description | Systematic Uncertainty |
|---|---|
| Luminosity | 5.4% |
| Single Interaction Cut | 4% |
| Jet Energy scale correction [59] | vary jet threshold $E_T$ by 10% |
| VECBOS uncertainty | 10%/jet |

agreement between the VECBOS and measured cross sections within 20% [76] for inclusive $W$ boson production cross section. There was also a systematic shift in the jet energy spectrum of the data compared with the parton-level VECBOS output [77]. VECBOS performs a leading order exact calculation and lacks some of the softening next-to-leading-order effects. This feature disappears when the parton jets are hadronized, allowing occasional creation of extra jets due to splitting, accomplished by the interface to ISAJET.

A systematic error in the luminosity was determined by comparing unbiased DØ data samples to Monte Carlo event generators with DØGeant detector simulations [53]. The overall L0 trigger efficiency was determined to have a systematic uncertainty of 5.4%. This error has been combined with other errors, statistical as well as systematic, for the background events as shown in Table 5.3.

# CHAPTER 6
# RESULTS

From the data collected, 5 candidate events remain with high $\not{E}_T$ and 4 jets. The background from $W$ and $Z$ boson production was estimated from Monte Carlo to be $5.2 \pm 2.2$ events, where the statistical and systematic errors have been combined in quadrature. The QCD background has been estimated from collider data to be $1.54 \pm 0.88$ (stat) events. Thus, the number of observed events with significant $\not{E}_T$ is compatible with that expected from the Standard Model, i.e. there is no evidence for events requiring "New Physics" for their explanation. This null result is used to establish a lower limit on the squark and gluino masses.

The QCD background is the least understood of all the backgrounds. Because of the extrapolation to such large values of $\not{E}_T$, and small statistics available, a small variation in the fitted function would result in a large change in the QCD background estimate. Therefore, the QCD background has not been included in the total background estimate for the calculation of the mass limits. This provides a more conservative limit, since by underestimating the background a larger signal cross section is necessary before any events can be observed.

## 6.1 Event Limit

The observed number of events was assumed to be the result of statistical fluctuations originating from a Poisson distribution, convoluted with a gaussian-distributed background whose mean is the expected number of background events and width is equal to the background uncertainty.

A Poisson distribution with mean $\mu$ (the predicted non-negative real number) and $n$ (the observed non-negative integer) is

$$f(n;\mu) = \frac{\mu^n e^{-(\mu)}}{n!},$$

where $f(n_o;\mu)$ is the probability to observe $n_o$ events when the mean is $\mu$. When $\mu$ is large ($\sim 8$), the distribution may be approximated with a Gaussian distribution of mean $\mu$ and variance $\sigma^2 = \mu$. The confidence level ($C$), means that for any random observation of $n$, $C$ percent of the time $n$ lies below the observed $n_o$. In the case of no background, and when $n_o$ events have been observed, we define an upper limit $N_{\text{limit}}(C)$ at confidence level $C$ to be the mean of that Poisson distribution for which the probability of observing more than the $n_o$ events is $= 1 - C$, i.e. $N_{\text{limit}}$ is the solution of the equation

$$\sum_{i=0}^{n_o} \frac{(N_{\text{limit}})^i}{i!} e^{-(N_{\text{limit}})} = 1 - C$$

To extract a limit for an experiment with background, both the signal and background are drawn from a Poisson distribution. The sum $n_o = n_s + n_b$ of two random variables $n_s$ and $n_b$ drawn from Poisson distributions with means $\mu_s$ and $\mu_b$, respectively, is also Poisson distributed, with mean $\mu_o = \mu_s + \mu_b$. When the background is estimated to be $= \mu_b$, with negligible uncertainty, the upper limit on the number of signal events, $N_{\text{limit}}$, can be found by solving the equation

$$C = 1 - \frac{\sum_{i=0}^{n_o} \frac{(N_{limit}+\mu_b)^i}{i!} e^{-(N_{limit}+\mu_b)}}{\sum_{i=0}^{n_o} \frac{\mu_b^i}{i!} e^{-\mu_b}}$$

However, in the presence of background with uncertainty, the Poisson-distributed signal is convoluted with a gaussian-distributed background whose mean is the expected number of background events and width is equal to the background uncertainty. The equation for the confidence level is then [78]

$$C = 1 - \frac{g(N_{limit})}{g(0)}$$

where

$$g(a) = \sum_{i=0}^{n_o} \int_{x<-a}^{\infty} \frac{(x + N_{limit})^i}{i!} e^{[\frac{-(x-\mu_b)^2}{2\sigma_b^2 - (x - N_{limit})}]} dx$$

For $n_o = 5$ events observed and a background estimate of $\mu_b = 5.2 \pm 2.2$ events, and choosing the confidence level to be $C = 95\%$, the above equation is solved to obtain $N_{limit} \geq 7.53$ signal events.

## 6.2 Mass Limit

To extract mass limits for the squark and gluino, the theoretical cross section for their production and their detection efficiency were parametrized as a function of squark and gluino masses. This parametrization is necessary to allow interpolation between the values of the squark and gluino masses for which cross sections and detection efficiencies were calculated. The squark-gluino production cross section from ISAJET (see Figure 1.3) was parametrized as an exponential function as shown in Figures 6.1 and 6.2. The signal efficiencies were determined for 36 points in the squark-gluino mass plane with ISASUSY Monte Carlo (see Table 5.6). The efficiencies were parametrized with a $\chi^2$ fit to a linear fuction for two cases: $m_{\tilde{q}}$= 500 GeV/c$^2$ and $m_{\tilde{q}}$=$m_{\tilde{g}}$.

The mass limit was derived from the comparison of the theoretical SUSY cross section $\sigma_{\rm th}(m_{\tilde{q}}, m_{\tilde{g}})$ with the experimentally determined 95% C.L. upper limit on the cross section,

$$\sigma_{\rm limit}(m_{\tilde{q}}, m_{\tilde{g}}) = \frac{N_{\rm limit}}{\mathcal{L} \cdot \epsilon(m_{\tilde{q}}, m_{\tilde{g}})}$$

where $N_{\rm limit} = 7.53$ events (the minimum number of signal events that may rule out a squark-gluino mass combination at a 95% confidence level), $\mathcal{L} = 7.45 \pm 0.41$ pb$^{-1}$ (the integrated luminosity) and $\epsilon(m_{\tilde{q}}, m_{\tilde{g}})$ is the detection efficiency for squarks and

gluinos of masses $m_{\tilde{q}}$ and $m_{\tilde{g}}$. If $\sigma_{\rm limit}(m_{\tilde{q}}, m_{\tilde{g}}) < \sigma_{\rm th}(m_{\tilde{q}}, m_{\tilde{g}})$, then the corresponding mass values $m_{\tilde{q}}$ and $m_{\tilde{g}}$ can be ruled out. If the experimental cross section limit is smaller than the supersymmetry cross section from Monte Carlo, then the squark and gluino masses can be ruled out. Figures 6.1 and 6.2 show the DØ cross section limit and the supersymmetry cross section. For heavy squarks (500 GeV/c$^2$) the gluino mass limit for 95% confidence level is

$$m_{\tilde{g}} > 163 \text{ GeV/c}^2.$$

For equal mass squarks and gluinos the limit is

$$m_{\tilde{q}} = m_{\tilde{g}} > 213 \text{ GeV/c}^2.$$

Since the efficiencies and cross sections vary between squark and gluino masses, it is appropriate to determine the limit in the squark-gluino mass plane. To determine the mass limit in the squark-gluino mass plane, the cross section limits were compared with the cross sections from ISAJET, Figure 1.3. The mass limit in the squark-gluino mass plane is shown in Figure 6.3, where the open circles are the Monte Carlo points that cannot be excluded, and the solid triangles are the Monte Carlo points that can be excluded. There are a few comments that should be made regarding this figure.

For $m_{\tilde{g}} \gg m_{\tilde{q}}$, the renormalization group evolution drives $m_{\tilde{q}}^2$ to negative values before the unification scale [79]. This is shown in Figure 6.3 as the contour at the bottom right corner. This constraint comes from the squark mass being related to the gluino mass in Supergravity theories [16], where the squark cannot be much lighter than the gluino before becoming the LSP. In the minimal supersymmetric model, the LSP cannot be charged or strongly interacting.

Right-handed squarks decay differently than left-handed squarks. The left-handed squarks have large SU(2) gauge couplings, which causes decays into charginos to dominate, whereas the right-handed squarks decay directly into the

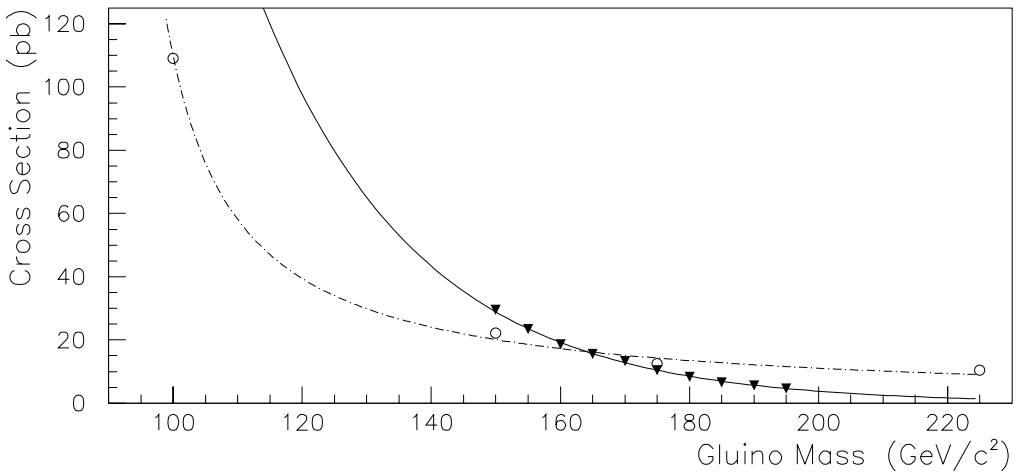


Figure 6.1: Squark-gluino production cross section (solid line) compared to the DØ lower limit contour (dotted line) with a 95% confidence level. The squark mass was fixed at 500 GeV/$c^2$. The intersection of the two curves indicates a mass limit of 163 GeV/$c^2$.

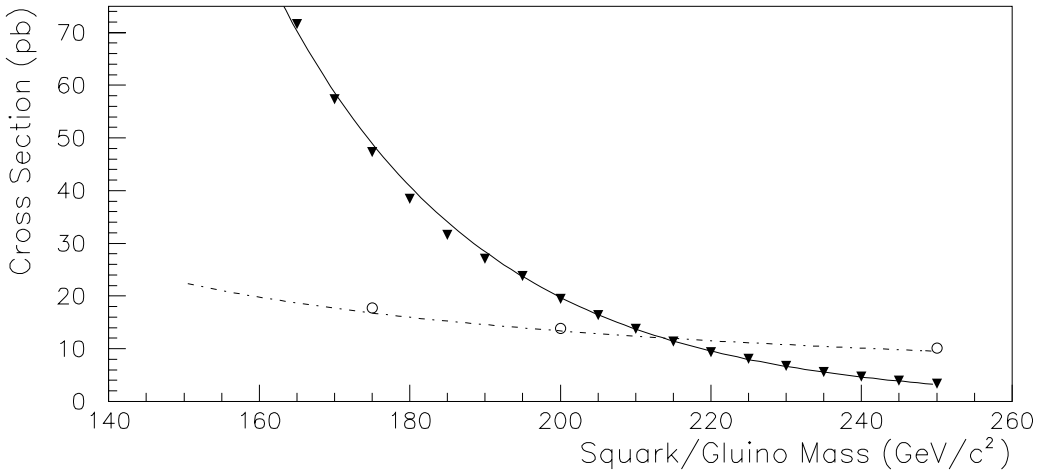


Figure 6.2: Squark-gluino production cross section (solid line) compared to the DØ lower limit contour (dot-dashed line) with a 95% confidence level. The squark and gluino masses were equal with a limit of 213 GeV/$c^2$.

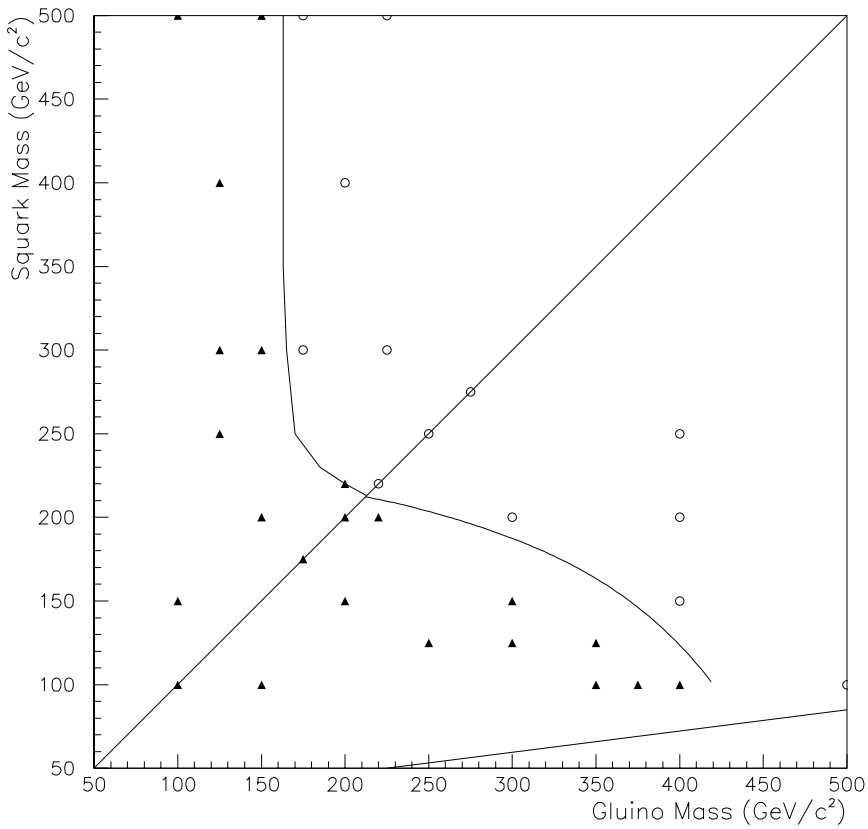


Figure 6.3: DØ lower limit for the squark-gluino mass plane at a 95% confidence level. For heavy squarks ($m_{\tilde{q}}$= 500 GeV/c$^2$) the gluino mass limit is $m_{\tilde{g}} > 163$ GeV/c$^2$, and for equal squark and gluino masses the limit is $m_{\tilde{q}} = m_{\tilde{g}} > 213$ GeV/c$^2$. The solid triangles are the signal Monte Carlo points that have been ruled out, and the open circles are Monte Carlo points that cannot be ruled out. Below the contour at the bottom right corner, no cross section was computed because the squark mass is not allowed to be much smaller than the gluino mass before it becomes the LSP [16].

LSP. Furthermore, the LSP mass is intricately tied to the gluino mass [16]. For heavy gluinos, the squark-gluino cross sections are dominated by squark production. For these reasons the lower limit for squarks with very heavy gluinos never reaches an asympotic value. However, for heavy squarks, where gluino production dominates, the LSP mass is not affected by changes in the squark mass, and the gluino mass limit quickly reaches an asymptotic value.

Finally, this analysis is very similar to the DØ hadronic supersymmetry search in the channel 3 or more jets and high $\not\!\!E_T$, accepted for publication in Physical Review Letters [80]. That analysis required more stringent cuts on the jet threshold ($E_T > 25$ GeV and $\not\!\!E_T > 75$ GeV); however, more observed data and backgrounds caused a slightly lower limit set on the squark and gluino masses. The excluded masses for that analysis were for heavy squarks $m_{\tilde{g}} >$ 144 GeV/c$^2$ and for equal masses $m_{\tilde{q}} = m_{\tilde{g}} >$ 212 GeV/c$^2$. Figure 1.2 shows events from higher gluino masses have higher jet multiplicities. Furthermore, requiring more jets in each event reduces the backgrounds.

A comparison with published squark and gluino mass limits is shown in Figure 6.4.

## 6.3 Effect of Varying the $\not\!\!E_T$ Cut on the Mass Limit

If the $\not\!\!E_T$ cut is low (e.g., 50 GeV), the number of background events will be high; therefore for a limit to be set the number of events from signal Monte Carlo must be large, resulting in a low mass limit. Similarly, for a high $\not\!\!E_T$ cut (e.g., 100 GeV), the number of background events is close to zero but the signal efficiency is very small, resulting in a low mass limit. The optimal $\not\!\!E_T$ cut which maximizes the lower mass limit lies somewhere between these extremes.

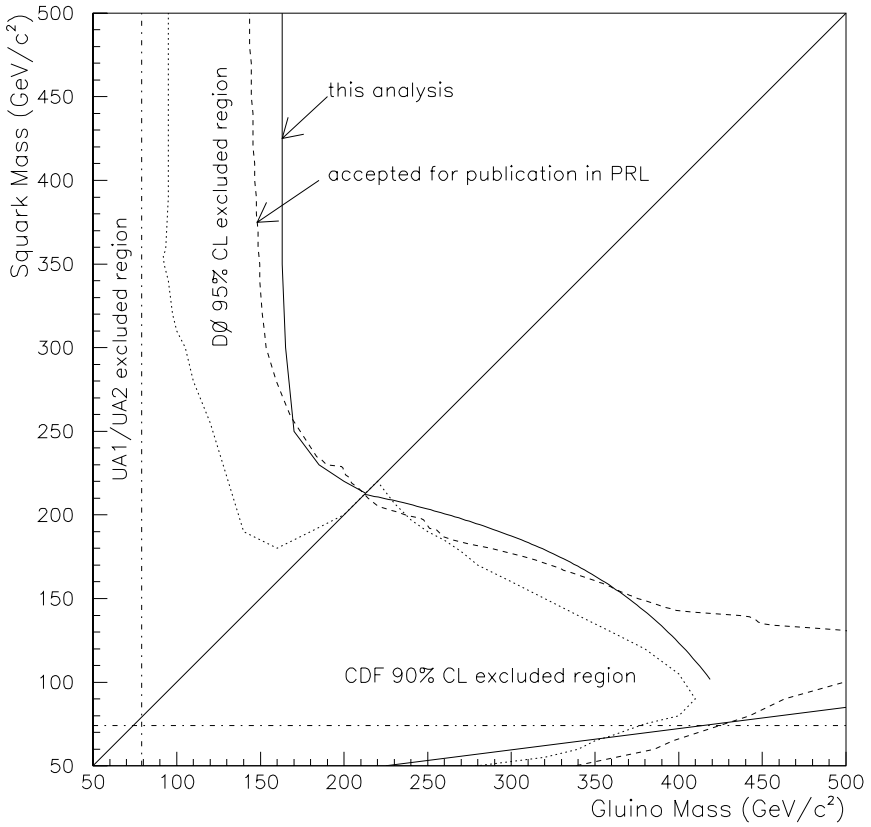


Figure 6.4: Squark-gluino mass limits from various experiments, including the DØ limit for this analysis at a 95% confidence level (solid curve). The dashed curve is the DØ mass limit for the analysis of $N_{\mathbf{jets}} \geq 3$ and $\not\!\!E_T > 75$ GeV, accepted for publication in Physical Review Letters [80].

The $\not\!\!E_T$ required by the data triggers was at most 35 GeV. A $\not\!\!E_T$ cut of 50 GeV was found to be high enough to avoid the steep rise in trigger efficiency due to the trigger threshold. To determine the best mass limit, the $\not\!\!E_T$ selection was varied between 50 and 100 GeV.

Figure 6.5 shows, as a function of the cut on the missing transverse energy, the number of signal events expected to survive that $\not\!\!E_T$ cut, for a fixed squark mass and various gluino masses. Also shown is the 95% experimental upper limit on the number of signal events versus the $\not\!\!E_T$ cut. The squark mass was held fixed at 500 GeV/c$^2$. Events entered into Figure 6.5 were subjected to two additional cuts: the ICD fraction (see Section 5.2.4) was required to be $< 50\%$ for all jets, to eliminate fake QCD events where a jet was mismeasured in the intercryostat region, and events with only one cell in a jet were removed (cells with $E > 1$ GeV energy, to eliminate the influence of noisy jets). By closely examining Figure 6.5, the best solution for maximizing the gluino mass limit was found to be for $\not\!\!E_T > 65$ GeV.

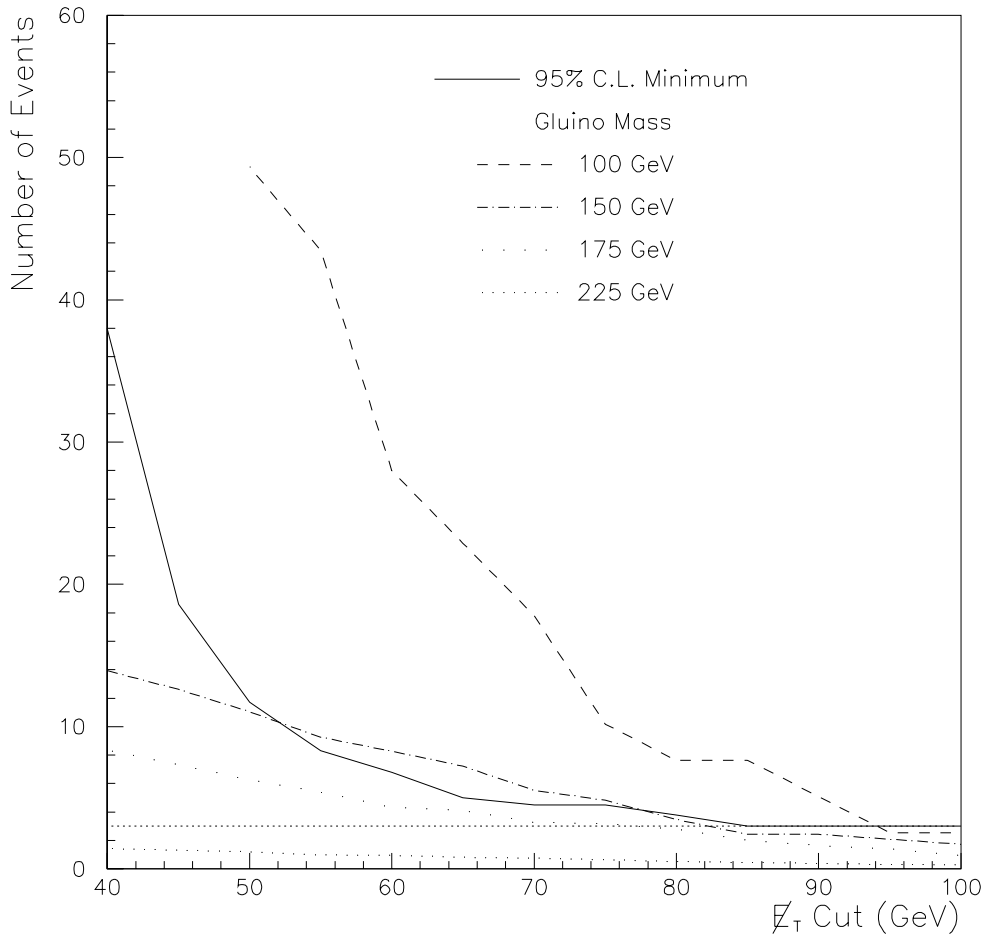


Figure 6.5: For a given $\not{E}_T$ cut, gluino masses for which there were more events from Monte Carlo than from the 95% confidence level can be ruled out. The squark mass was fixed at 500 GeV/c$^2$.

### 6.3.1 Effects of Varying Supersymmetry Model Parameters

The supersymmetry parameters $\mu$ and $\tan\beta$ have been held fixed, although the cross section and branching fractions are functions of these parameters. Variation of these parameters [81] does not vary the cross sections and branching fractions more than the theoretical uncertainty in the cross sections. The ISAJET Monte Carlo program allowed for varying choices of supersymmetry masses and mixings.

The $\tan\beta$ and $\mu$ parameters were varied for a fixed mass gluino (150 GeV/c$^2$) and squark (500 GeV/c$^2$). Figures 6.6 and 6.7 shows the variation.

The mass limits are insensitive to the changes in the charged Higgs mass if $m_{H+} \gg m_W$ [24], so therefore $m_{H+}$ was chosen to be 500 GeV/c$^2$. For small values of $\mu$, the gluino decay to a heavy neutralino dominates, causing a significant reduction in the $\not{E}_T$ signal. This is not a concern, since LEP measurements have already excluded the region for $\mu \simeq 0$ [21] as well as for positive $\mu$ values within the reach of the Fermilab Tevatron. The LSP gaugino content and mass varies little with variations in $\mu$, as long as $|\mu|$ is large compared to the $W$ boson mass.

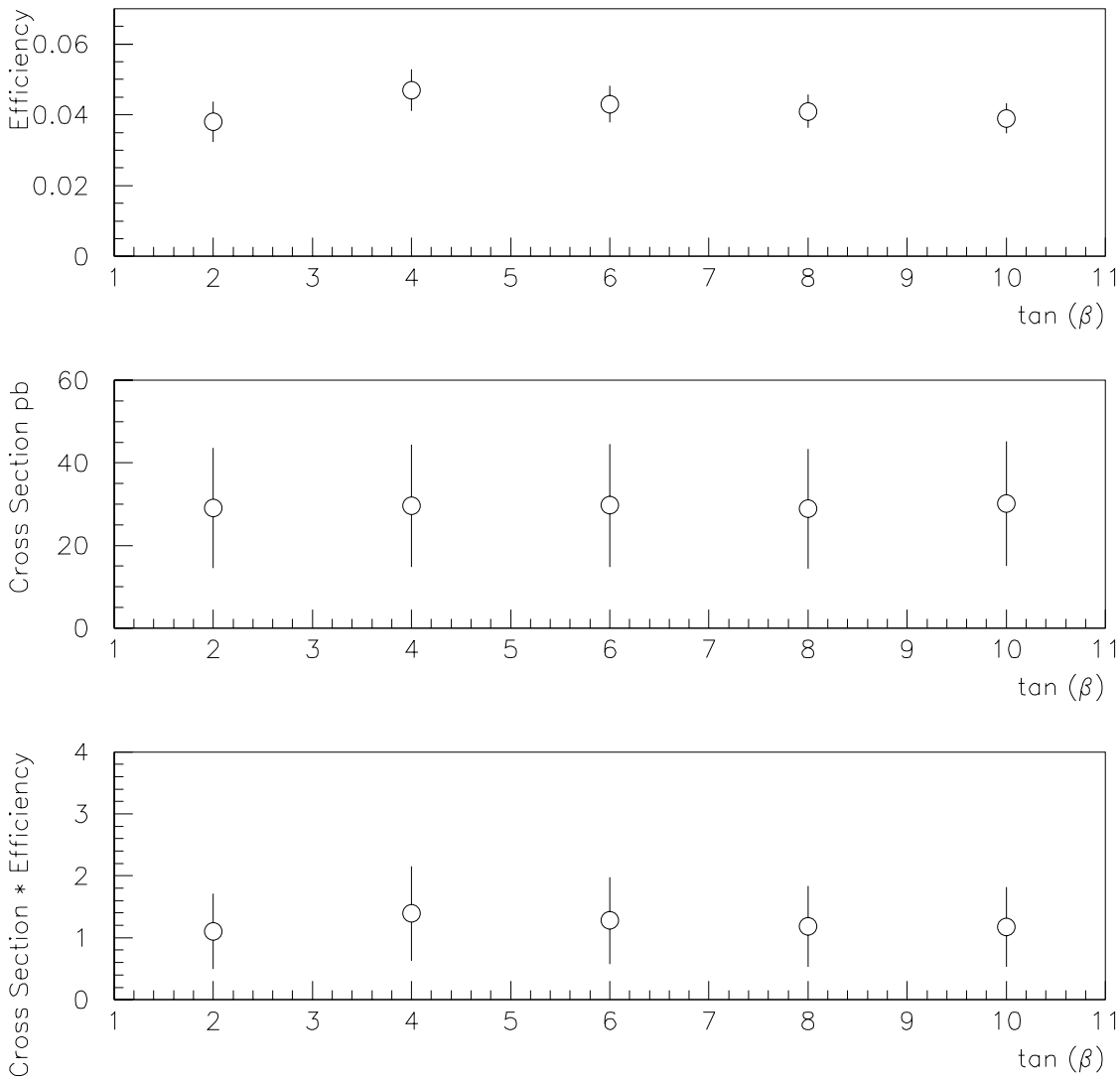


Figure 6.6: Effect of varying the $\tan\beta$ parameter on the cross section and efficiency for producing squarks and gluinos with $N_{\text{jets}} \geq 4$ and $\not{E}_T > 50$ GeV ($m_{\tilde{g}} = 150$ GeV/c$^2$, $m_{\tilde{q}} = 500$ GeV/c$^2$).

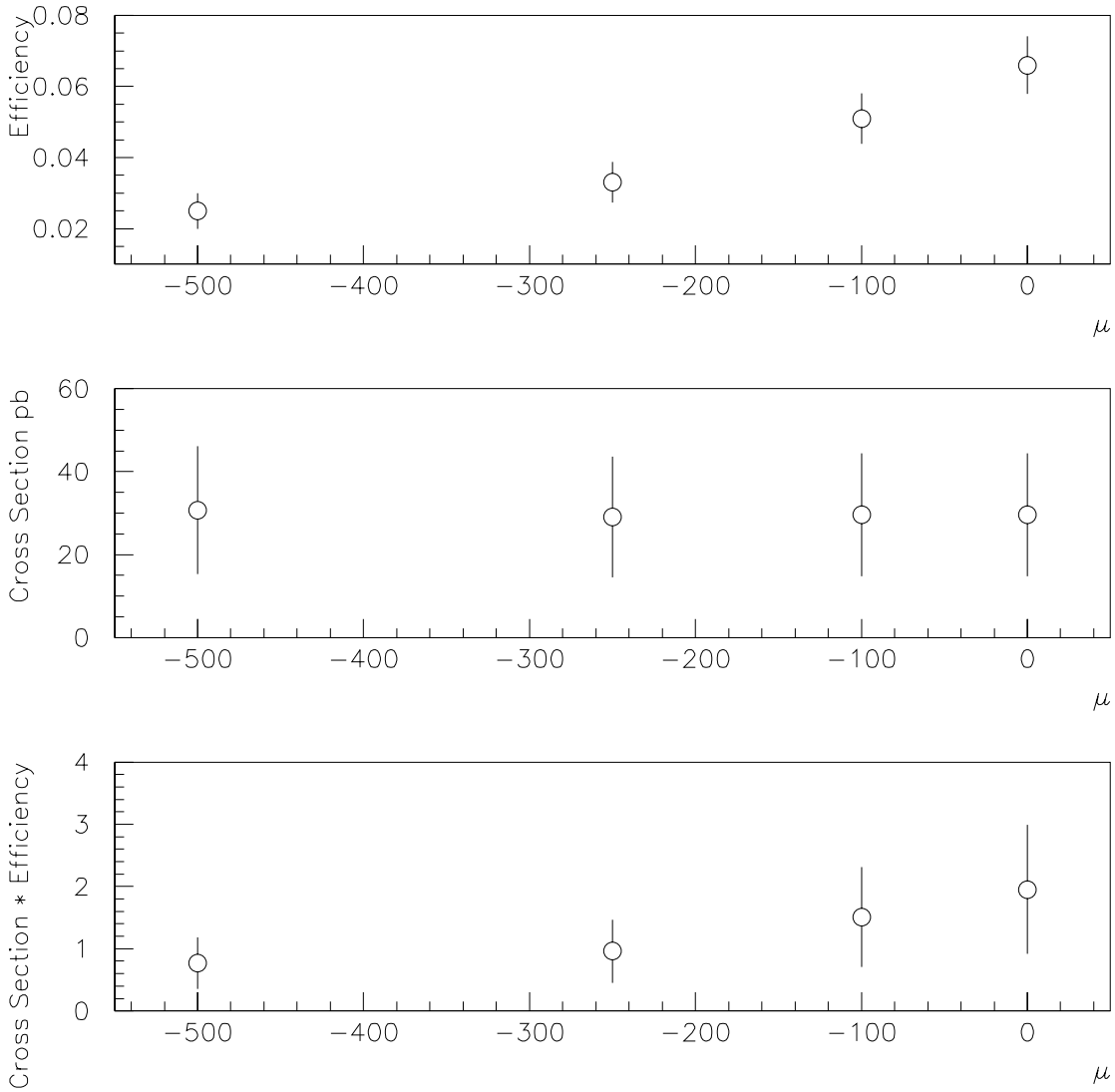


Figure 6.7: Effect of varying the $\mu$ parameter on the cross section and efficiency for squarks and gluinos with $N_{\rm jets} \geq 4$ and $\not{E}_T >$ 50 GeV ($m_{\tilde{g}}$= 150 GeV/c$^2$, $m_{\tilde{q}}$= 500 GeV/c$^2$).

## 6.4 Future Searches

Future searches at colliding beam facilities must handle large instantaneous luminosities giving rise to many interactions every beam crossing. In order to retain the full luminosity, and thus set higher limits, a new technique must be found. The $\not{E}_T$ resolution will be significantly degraded due to the uncertainty in the choice of a primary vertex. For Fermilab Collider Run 1b, the problem with multiple interactions must be handled so as to retain the full luminosity accepted by DØ. This will require a new method for handling the primary vertex for the $\not{E}_T$ calculation. One alternative is to use the jets in the event and their associated tracks to find the primary vertex position. A search with an event signature including leptons could also provide a method to locate the primary vertex and further reduce backgrounds.

Searches for supersymmetric particles at the LEP experiment ALEPH have provided a complementary search to the studies at Fermilab [16]. The LHC (Large Hadron Collider) is expected to begin collecting data at a high center of mass energy (14 TeV) early in the next century and will be able to discover supersymmetric particles or push the lower limits on their masses much higher than presently set [16].

An indirect but important test of extended theories is the measurement of the proton lifetime. The Standard Model does not require that the proton be stable and does not make any prediction regarding its lifetime. Grand Unified Theories, however, include quarks and leptons in a common representation creating a mechanism for protons to decay and their lifetime is estimated to be very large. Although no proton decays have been observed, a limit has been established on the proton lifetime by large-scale experiments such as IMB, Kamiokande and Frejus [82] of $> 9 \times 10^{32}$ years at a 90% confidence level. This limit is greater than any currently predicted lifetime. Future experimental limits on the proton lifetime will be important to studies of extended theories.

## BIBLIOGRAPHY


[1] B. Gruber and T. Otsuha, *Symmetries in Science VIII* (Plenum Press, 1993).

[2] J. Kepler, *Mysterium Cosmographicum* (1595).

[3] W. Pauli, Z. Physik **36**, 336 (1926).

[4] M. Gell-Mann, Phys. Rev. **125**, 1067 (1962); Y. Ne'eman, Nucl. Phys. **26**, 222 (1961).

[5] H. Fritzsch, M. Gell-Mann and H. Leutwyler, Phys. Lett. **B47**, 365 (1973); J. Friedman and H. Kendall, Ann. Rev. Nucl. Sci. **22**, 203 (1972).

[6] S. Glashow, Nucl. Phys. **22**, 1264 (1961).

[7] DØ Collaboration, S. Abachi *et al.*, Phys. Rev. Lett. **74**, 2632 (1995); CDF Collaboration, F. Abe *et al.*, Phys. Rev. Lett. **74**, 2626 (1995).

[8] Review of Particle Properties, Phys. Rev. **D45**, 11 (1992).

[9] G. Arnison *et al.*, Phys. Lett. **122B**, 103 (1982).

[10] P. Higgs, Phys. Rev. Lett. **13**, 508 (1964).

[11] S. Weinberg, Phys. Rev. **B14**, 387 (1976).

[12] H. Haber and G. Kane, Phys. Rep. **117**, 75 (1985); X. Tata, "Lectures presented at the Mt. Sorak Symposium on the Standard Model and Beyond," Mt. Sorak, Korea, Univ. of Hawaii preprint UH-511-713-90 (unpublished).

[13] J. Wess and B. Zumino, Nucl. Phys. **B70**, 39 (1974).

[14] H. Nilles, Phys. Rep. **C110**, 1 (1984); P. Nath, R. Arnowitt and A. Chamseddine, "Applied $N = 1$ Supergravity," ICTP Series in Theoretical Physics, Vol. I, World Scientific (1984).

[15] G. Ross, *Grand Unified Theories* (Benjamin Cummings Publishing Co., 1985).

[16] H. Baer *et al.*, "Low Energy Supersymmetry Phenomenology," FSU-HEP-950401 (1995) (unpublished).

[17] J. Wess and J. Bagger, *Supersymmetry and Supergravity* (Princeton University Press, Princeton, NJ, 1983).

[18] J. Ellis, J.S. Hagelin, D.V. Nanopoulos, K. Olive, and M. Srednicki, Nucl. Phys. **B238**, 453 (1984).

[19] B. Campbell, Phys. Rev. **D28**, 209 (1983); F. Gabbiani and A. Masiero, Nucl. Phys. **B322**, 235 (1989).

[20] R. Alitti *et al.*, Phys. Lett. **235B**, 363 (1990).

[21] T. Medcalf, "The Search for Supersymmetry with the Aleph Detector at LEP," **International Workshop on Supersymmetry and Unification of Fundamental Interactions**, P. Nath ed., World Scientific, Singapore (1993).

[22] H. Baer, "Preceedings of the 1990 Summer Study on HEP," Snowmass (1990).

[23] F. Abe *et al.*, Phys. Rev Lett. **69** (1992).

[24] H. Baer, X. Tata and J. Woodside, "Update of the Effect of Cascade Decays on the Tevatron Gluino and Squark Mass Bounds," FSU-HEP-910211, (1991) (unpublished).

[25] L. Roszkowski, Phys. Lett. **252B**, 471 (1991).

[26] H. Baer, J. Ellis, G. Gelmini, D. Nanopoulas and X. Tata, Phys. Lett. **161B**, 175 (1985); G. Gamberini, Z Phys. **C30**, 605 (1986).

[27] H. Baer, X. Tata, and J. Woodside, Phys. Rev. Lett. **63**, 352 (1989).

[28] H. Baer, X. Tata and J. Woodside, Phys. Rev. **D41**, 906 (1990).

[29] F. Paige and S. Protopopescu, BNL Report no. BNL38034, (1984) (unpublished).

[30] H. Baer *et al.*, Phys. Rev. **D51**, 2180 (1995).

[31] H. Baer *et al.*, Phys. Rev. **D50**, 4517 (1994).

[32] Personal communication with H. Baer.

[33] J. Botts *et al.*, Phys. Lett. **B304**, 159 (1993).

[34] W. Beenakker *et al.*, "Squark Production at the Tevatron," DESY 94-212 (1994) (unpublished).

[35] "Design Report, the DØ Experiment at the Fermilab $\overline{p}p$ Collider," DØNote 137 (1984) (unpublished).

[36] S. Abachi *et al.*, "The DØ Detector," Nucl. Instr. and Meth. **A338**, 185 (1994).

[37] M.D. Church and J.P. Marriner, "The Antiproton Sources: Design and Operation," Annu. Rev. Nucl. Part. Sci., **43**, 253 (1993).

[38] R. Wigmans, "Energy Loss of Particles in Dense Matter," Lecture Notes, ICFA School on Instrumentation in Elementary Particle Physics.

[39] S. Abachi *et al.*, Nucl. Instr. and Meth. **A324** 53 (1993).

[40] P. Franzini, Nucl. Instr. and Meth., **A289**, 438 (1990).

[41] K. De, "A Monte Carlo Study of Hadronic Energy Corrections in the ICD," DØNote 1017 (1990) (unpublished).

[42] A. Clark *et al.*, Nucl. Instr. and Meth. **A315**, 193 (1992).

[43] F. Feinstein, Ph.D. Thesis, (unpublished).

[44] A. Clark *et al.*, Nucl. Inst. and Meth. **A279**, 243 (1989).

[45] C. Brown *et al.*, Nucl. Instr. and Meth. **A279**, 331 (1989).

[46] D. Cutts *et al.*, "Proceedings of the Conference on Computing in High Energy Physics," CERN Preprint 92-01, pp. 262 (1992) (unpublished).

[47] R. Angstadt *et al.*, Proceedings of the IEEE Meeting, Santa Fe, NM (1991) (unpublished).

[48] R. Partridge, "Data Acquisition Triggers Level 0," DØNote 1218 (1991) (unpublished).

[49] M. Abolins *et al.*, Nucl. Instr. and Meth. **A289**, 543 (1990).

[50] Denisenko, "GLBMON-The Online Program for the Monitoring of Data Flow in DØ," DØNote 1684 (1993) (unpublished).

[51] A. Boehnlein, "Changes made to L2ETMISS and L2ETSUM during Run Ia," DØNote 1664 (1993) (unpublished).

[52] N. L. Grossman, "A Study of Hot Cells and Jets," DØNote 2525 (1995) (unpublished).

[53] J. Bantly *et al.*, "Improvement to the DØ Luminosity Monitor Constant," DØNote 2544 (1995) (unpublished).

[54] S. Fahey *et al.*, "Flagging Calorimeter Noisy Cells," DØNote 2379 (1994) (unpublished).

[55] J. Huth *et al.*, "Fixed-cone Clustering Algorithm," Proceedings of the Summer Study on High Energy Physics, Snowmass, Colorado (1990); F. Abe *et al.*, Phys. Rev. **D45**, 1448 (1992).

[56] F. Halzen and A. Martin, *Quarks and Leptons* (John Wiley and Sons, Inc., 1984).

[57] S. D. Ellis, Z. Kunszt and D. E. Soper, Phys. Rev. **D40**, 2188 (1989).

[58] R. Astur *et al.*, "Determining The Jet Energy Scale Using the Test Beam," DØNote 1683 (1993) (unpublished).

[59] A. Milder and R. Astur, "Jet Energy Calibration Using the Missing $E_T$ Projection Fraction," DØNote 1657 (1993).

[60] ALEPH Collab., D. Decamp, *et al.*, Phys. Lett. **B235**, 399 (1990).

[61] Particle Data Group, Phys. Rev. **D45**, 11 (1992).

[62] F. Abe *et al.*, Fermilab-Pub-92/182-E, submitted to Phys. Rev. Lett.

[63] W. Dharmaratna, R. Raja and C. Stewart, "The DØ Shower Library Version 2.0," DØNote 1730 (1993) (unpublished).

[64] M. Paterno, "A Study of the DØ Calorimeter $\not\!\!E_T$ Resolution Using Low $E_T$ Triggers," DØNote 1782 (1993) (unpublished); M. Paterno, "A Monte Carlo Study of the DØ Calorimeter $\not\!\!E_T$ Resolution," DØNote 1374 (1992) (unpublished).

[65] J. Bantly and Q. Li-Demarteau, "Multiple Interaction Tool," DØNote 1691 (1993) (unpublished).

[66] M. Paterno, DØNote 2187 (1994) (unpublished), and private communication from M. Paterno.

[67] R. Astur, "A Study of Standard Jet Cuts and their Efficiencies Using DØ Collider Data," DØNote 1763 (1993) (unpublished); R. Astur, "A Study of Fake Jets in the DØ Detector," DØNote 1662 (1993) (unpublished).

[68] J. Butler, "Main Ring Dead Time," DØNote 1682 (1993) (unpublished).

[69] Brun and F.Carminati, "GEANT Detector Description and Simulation Tool," CERN Program Library Long Writeup W5013 (1993) (unpublished).

[70] F. Carminati *et al.*, "GEANT User's Guide," CERN Program Library (1991) (unpublished).

[71] J. Womersley, R. Raja and A. Jonchheere, "Shower Libraries for DØ GEANT Monte Carlo," DØNote 650 (1983) (unpublished).

[72] W. Giele, Ph.D. Thesis, (unpublished).

[73] A. Milder, Ph.D. Thesis, DØNote 1874 (1994) (unpublished).

[74] H. Baer *et al.*, "Simulating supersymmetry with ISAJET 7.0 / ISASUSY 1.0," Argonne Accel. Phys. 703 (1993).

[75] R. Astur, " Energy Scale Corrections," DØNote 2089 (1994) (unpublished).

[76] S. Abachi *et al.*, "Top Quark Search with the D0 1992-93 Data Sample," (1995) submitted for publication.

[77] E. Varnes, "Comparison of Jet Kinematics in VECBOS and $W \rightarrow e\nu$ Data," DØNote 2425 (1995) (unpublished).

[78] G. Zech, Nucl. Inst. and Meth. **A277**, 608 (1989).

[79] U. Ellwanger, Phys. Lett. **141B**, 435 (1984).

[80] S. Abachi *et al.*, "Search for squarks and gluinos in $p\overline{p}$ collisions at $\sqrt{s} = 1.8$ TeV," FERMILAB-PUB-95-057-E (1995); accepted for publication in Phys. Rev. Lett.

[81] H. Baer, X. Tata and J. Woodside, Phys Rev. **D44**, 207 (1991).

[82] C. Arpesella *et al.*, Phys. Lett. **B269**, 227 (1991).

## BIOGRAPHICAL SKETCH

Mark Andrew Goforth.....Born in Winston-Salem, N.C. June 30, 1966

### Education

1980-1984 Ben C. Rain High School, Mobile, Alabama

1984-1988 University of South Alabama, Mobile, Alabama

Bachelor of Science

Major: Physics

1988-1995 Florida State University, Tallahassee, Florida

Doctor of Philosophy

Physics

### Publications

S. Abachi *et al.*, "BEAM TESTS OF THE D0 URANIUM LIQUID ARGON END CALORIMETERS," Nucl. Instr. and Meth. **A324**, 53 (1993).

H. Aihara *et al.*, "DESIGN, CONSTRUCTION, AND PERFORMANCE OF THE ELECTROMAGNETIC MODULE OF THE D0 END CALORIMETER," Nucl. Instr. Meth. **A325**, 393 (1993).

S. Abachi *et al.*, "THE D0 DETECTOR," Nucl. Instr. and Meth. **A338**, 185 (1994).

S. Abachi *et al.*, "FIRST GENERATION LEPTOQUARK SEARCH IN $p\overline{p}$ COLLISIONS AT $\sqrt{s} = 1.8$ TEV," Phys. Rev. Lett. **72**, 965 (1994).

S. Abachi *et al.*, "SEARCH FOR THE top QUARK IN $p\overline{p}$ COLLISIONS AT $\sqrt{s} = 1.8$ TEV," Phys. Rev. Lett. **72**, 2138 (1994).

S. Abachi *et al.*, "RAPIDITY GAPS BETWEEN JETS IN $p\overline{p}$ COLLISIONS AT $\sqrt{s} = 1.8$ TEV," Phys. Rev. Lett. **72** 2332 (1994).

S. Abachi *et al.*, "INCLUSIVE MU AND B QUARK PRODUCTION CROSS-SECTIONS IN $p\overline{p}$ COLLISIONS AT $\sqrt{s} = 1.8$ TEV," Phys. Rev. Lett. **74**, 3548 (1995).

S. Abachi *et al.*, "SEARCH FOR HIGH MASS TOP QUARK PRODUCTION IN $p\overline{p}$ COLLISIONS AT $\sqrt{s} = 1.8$ TEV," Phys. Rev. Lett. **74**, 2422 (1995).

S. Abachi *et al.*, "DISCOVERY OF THE TOP QUARK," Phys. Rev. Lett. **74**, 2632 (1995).